2015-12-22

Simultaneous Dynamic Optical Refraction and Biometry of the Human Accommodative Response

Victor M. Hernandez
University of Miami, vmhernandez112@gmail.com

UNIVERSITY OF MIAMI

SIMULTANEOUS DYNAMIC OPTICAL REFRACTION AND BIOMETRY OF THE HUMAN ACCOMMODATIVE RESPONSE

By

Victor M. Hernandez

A DISSERTATION

Submitted to the Faculty
of the University of Miami
in partial fulfillment of the requirements for
the degree of Doctor of Philosophy

Coral Gables, Florida

December 2015

UNIVERSITY OF MIAMI

A dissertation submitted in partial fulfillment of
the requirements for the degree of
Doctor of Philosophy

SIMULTANEOUS DYNAMIC OPTICAL REFRACTION AND BIOMETRY OF THE HUMAN ACCOMMODATIVE RESPONSE

Victor M. Hernandez

Approved:

Fabrice Manns, Ph.D.
Professor of Biomedical Engineering and Ophthalmology

Noel Ziebarth, Ph.D.
Assistant Professor of Biomedical Engineering

Jean-Marie Parel, Ph.D.
Henri and Flore Lesieur Chair in Ophthalmology, Research Associate Professor of Ophthalmology and Biomedical Engineering

Jorge Bohorquez, Ph.D.
Associate Professor of Professional Practice of Biomedical Engineering

Sonia H. Yoo, M.D.
Professor of Ophthalmology and Biomedical Engineering

Arthur Ho, B.Optom. (Hon.) M.Optom., Ph.D., FAAO
Chief Technologist
Brien Holden Vision Institute
Professorial Visiting Fellow
School of Optometry and Vision Science, University of New South Wales, Sydney, Australia

Dean of the Graduate School

HERNANDEZ, VICTOR M. (Ph.D., Biomedical Engineering)
(December 2015)

Simultaneous Dynamic Optical Refraction and Biometry of the Human Accommodative Response.

Abstract of a dissertation at the University of Miami.

Dissertation supervised by Professor Fabrice Manns.
No. of pages in text. (134)

The ability of the crystalline lens to change shape and bring near objects into focus is known as accommodation. Over time, the deformability of the lens decreases, deteriorating near visual function. This condition is known as presbyopia. There are many ways in which presbyopia correction is addressed, but currently there does not exist a method capable of restoring a dynamic visual range. In order to better understand the accommodative process and evaluate future corrective approaches, we require a system capable of dynamically acquiring refraction and biometric information. The goal of this work was to design, develop, and test a system that is capable of measuring dynamically the optical and physical changes that occur in the eye during stimulated accommodation. The system consists of: a high dynamic range Shack-Hartmann based autorefractor, an extended-depth spectral domain optical coherence tomography (SD-OCT) system for anterior segment imaging, a 1300 nm SD-OCT system for trans-scleral ciliary body imaging, and a dual channel modified Badal optometer for the stimulation of accommodation. This involved the development of optomechanical systems, software design for system integration, and the design of experiments to test system modules. A method to calculate lens power from OCT biometry, corneal topography, and refraction was devised to correlate change in lens

thickness to lens power during accommodation. The results acquired during human subjects testing demonstrate proof of concept.

This dissertation is dedicated to my wife, Pamela Hernandez.

ACKNOWLEDGEMENTS

I would like to begin by thanking my mentors, Fabrice Manns, Ph.D. and Jean-Marie Parel, Ph.D., for their patience, dedication, and guidance throughout my doctoral studies and for providing me the opportunity to work and learn alongside them at the Ophthalmic Biophysics Center.

I would like to thank my committee members; Jorge Bohorquez, Ph.D., Arthur Ho, Ph.D., Sonia Yoo, M.D., and Noel Ziebarth, Ph.D., for their support throughout this project.

I am also grateful to everyone at the Ophthalmic Biophysics Center and Bascom Palmer Eye Insitute who played a role in this and my many other projects: Mariela Aguilar, M.S., Karam Alawa, B.S., Alejandro Arboleda, M.S., Esdras Arrieta, M.D., Andres Bernal, M.S., David Borja, Ph.D., Florence Cabot, M.D., Carolina de Freitas, M.S., Stephanie Delgado, M.S., Heather Ann Durkee, M.S., Alex Gonzalez, B.A., Eleut Hernandez, Shawn Kelly, M.S., William Lee, Keke Liu, Bianca Maceo, B.S., Derek Nankivil, M.S., Izuru Nose, B.S.E.E., Cor Rowaan, B.S.E.M., Marco Ruggeri, Ph.D., Nelson Salas, Ph.D., Juan Silgado, Mukesh Taneja, M.D., Stephen Uhlhorn, Ph.D., and Raksha Urs, Ph.D.

I would like to thank my parents, Manuel Hernandez and Joceline Hernandez, and my sister Sasha Hernandez, for their unwavering support and encouragement throughout my academic career. I am also eternally grateful for my wife, Pamela Hernandez, for her patience and dedication throughout my doctoral studies.

This work was supported by: NIH grants R01EY021834 and R01EY014225, NIH center grant P30 EY14801, Florida Lions Eye Bank, Vision CRC, Sydney, Australia,

Research to Prevent Blindness, the Henry and Flore Lesieur Foundation, and Drs. Karl R. Olsen and Martha E. Hildebrandt.

TABLE OF CONTENTS

LIST OF FIGURES

LIST OF TABLES

PUBLICATION NOTE

The following are peer-reviewed articles, and conference proceedings that resulted from this dissertation.

Peer-Reviewed Journal Publications:

Hernandez V, Cabot F, Ruggeri M, de Freitas C, Ho A, Yoo S, Parel JM, Manns F. Calculation of crystalline lens power using a modification of the Bennett method. *Biomedical Optics Express* 6(11):4501-4515; 2015.

Ruggeri M, de Freitas C, Williams S, **Hernandez VM**, Cabot F, Yesilirmak N, Alawa K, Chang Y-C, Yoo S, Gregori G, Manns F, Parel JM. Quantification of the ciliary muscle and crystalline lens interaction during accommodation with synchronous OCT imaging. To be submitted to Biomedical Optics Express. December 2015.

Conference Proceedings:

Ruggeri M, **Hernandez V**, de Freitas C, Manns F, Parel J-M. Biometry of the ciliary muscle during dynamic accommodation assessed with OCT. In Ophthalmic Technologies XXIV, Proceedings SPIE Vol. 8930:89300W; 2014. (Winner of the best conference paper out of 57 submissions, Pascal Rol Award)

Conference Abstracts:

Hernandez V, Ruggeri M, Manns F, Parel JM. Measurement of accommodation with high dynamic range using a Shack-Hartmann wavefront sensor and dual-channel accommodation stimulus. Poster Presentation, Association for Research in Vision and Ophthalmology (ARVO) Annual Meeting, Denver, CO, May 7, 2015, Poster 6010-B0159.

Cabot F, Ruggeri M, Manns F, de Freitas C, **Hernandez V**, Yoo SH, Parel JM. Real-time imaging of accommodation with transscleral and anterior segment Optical Coherence Tomography. ASCRS conference; San Diego, CA; Paper #12791; April 21, 2015. Winner of the best poster award.

Hernandez VM, Ruggeri M, Cabot FA, Ho A, Manns F, Parel JM. Dynamic refraction and biometry of the anterior segment during accommodation. Abstract and Poster Presentation #9307-58; Ophthalmic Technologies XXV, Photonics West BIOS Conference; San Francisco, CA; February 7-8, 2015.

Ruggeri M, **Hernandez VM**, Williams SW, De Freitas C, Cabot FA, Manns F, Parel JM. Dynamic biometric response of the accommodative plant measured with OCT. Abstract and Poster Presentation #9307-57; Ophthalmic Technologies XXV, Photonics West BIOS Conference; San Francisco, CA; February 7-8, 2015.

Cabot F, **Hernandez V**, Manns F, Yoo SH, Ho A, Parel J-M. Evaluation of a real-time Hartman-Shack based autorefractor. ARVO Abstract and Poster Presentation #2717; Orlando, FL; May 6, 2014.

Arrieta EA, Aguilar MC, Arboleda A, Taneja M, Vaddavalli P, Moilanen J, Manns F, **Hernandez V**, Watling J, Parel J-M. Use of minicapsulorrhexis in the Phaco Ersatz technique for cataract surgery in a rabbit model. ARVO Abstract and Poster Presentation #2804; Orlando, FL; May 6, 2014.

Mohamed A, Durkee HA, Augusteyn RC, Urs R, **Hernandez V**, Bernal A, Manns F, Ho A, Parel J-M, Sangwan V. Digital mini-shadowphotogrammetric system for morphometric analysis of ex-vivo crystalline lenses: Pilot study on human lenses. ARVO Abstract and Poster Presentation #747; Orlando, FL; May 4, 2014.

Hernandez V, Delgado S, Borja D, Ho A, Manns F, Parel J-M. Real-time Hartmann-Shack autorefractor: Slit-lamp mounted prototype. Abstract and Oral Presentation #8567-29; Ophthalmic Technologies XXIII, Photonics West BIOS Conference; San Francisco, CA; February 2-3, 2013.

Chapter 1: Aims of the Study

Accommodation is the ability of the eye to change focus. During accommodation, the crystalline lens changes shape, effectively changing the optical power of the lens to bring near objects into focus. Presbyopia is the age-related loss of near visual function due to the gradual degradation of the ability of the crystalline lens to change shape. It is a condition that affects everyone, beginning between the ages of 40-45. This gradual loss of near visual ability can make routine near tasks more difficult to perform.

There are a number of correction or treatment options for presbyopia ranging from simple spectacle prescription to surgical techniques, such as accommodative intraocular lenses. There are also many new treatments for presbyopia in development, a need established by the continual growth of the presbyopic population. Some of these techniques are based on unproven theories of accommodation. Others may not be operating as intended, but their efficacy is difficult to characterize since these correction methods are typically evaluated subjectively. Even in approaches meant to restore accommodation, these subjective assessments often overestimate the amount of near visual ability restored in the patient. In order to assess the effectiveness of potential treatments designed to restore accommodation, an objective method of measuring accommodative response before and after treatment must be developed.

The goal of this project is to develop and evaluate a system that simultaneously measures the objective optical and mechanical accommodative response of the eye. The objective is to produce a device that can be used to qualitatively and quantitatively understand the changes that occur during accommodation and their age-dependence. This technology will allow for objective assessment of potential new surgical presbyopia treatments and verification of post-surgical results.

The specific aims of the study are:

Aim 1: Develop a high dynamic range real-time autorefractor and accommodation stimulus.

A Shack-Hartmann (S-H) aberrometer-based autorefractor will be developed for the purpose of the project in combination with an accommodation stimulus. The autorefractor requires a dynamic range of -20 D to +10 D in refraction measurement. The accommodation stimulus must provide a stimulus range with a maximum vergence change of -20 D. This would allow for a maximum stimulus of -10 D in a subject with a refractive error at the corneal plane of -10 D. The functionality of the system will be validated on three subjects.

Aim 2: Develop a method to calculate lens power from ocular biometry.

An optical model will be developed that will allow the measurement of lens power from whole eye OCT biometry, corneal topography, and refraction using a modified version of the Bennett method. The method will allow for the measurement of lens power and its change with accommodation. The method will be validated in 16 eyes.

Aim 3: Integration of the autorefractor with an accommodation biometry system for dynamic imaging of the anterior segment and ciliary muscle.

The integrated system will combine a modified existing extended-depth anterior segment SD-OCT system and a commercial SD-OCT system for the measurement of the ciliary muscle and the autorefractor described in Aim 1. Software and hardware will be developed to interface all four modules of the system (anterior segment SD-OCT, trans-scleral SD-OCT, S-H autorefractor, and accommodation stimulus) for acquisition of accommodation data and time delivery of the accommodation stimulus. The device will be used to quantify the relation between the change in lens thickness and lens power in three human subjects of different ages as proof of principle. The subjects will be imaged with

the integrated system during accommodation induced with a step stimulus ranging from 0 D to 6 D in 2 D steps. The images will be segmented and processed with a distortion algorithm developed separately to provide the shape of the cornea and lens during accommodation for each accommodative step. For each dataset, thickness-power responses will be calculated and a linear or non-linear regression will be performed to determine the relation.

Chapter 2: Background and Significance

This chapter briefly describes the mechanism of accommodation and its deterioration over time, leading to presbyopia. Methods to address this near visual loss with age, with their pros and pitfalls, are reviewed. This chapter also describes means to measure the shape, dimensions, and optical power of the eye during accommodation. These biometric systems can be used to inform decisions in the design and evaluation of correction techniques.

2.1 Accommodation and Presbyopia

Accommodation is the ability of the eye to focus on objects at different distances by changing the shape of the crystalline lens. Most of the evidence available today supports the Helmholtz theory of accommodation (Augusteyn, 2010; Burd et al, 1999; Doane & Jackson, 2007; Dubbelman et al, 2003; Queiros et al, 2012). Briefly, when viewing a distant object, the ciliary muscle of the eye is relaxed. This places the zonular fibers attached to the crystalline lens under tension, pulling the lens into a flattened shape. When the eye focuses on a near object, the ciliary muscle contracts. The contraction relaxes the tension on the zonular fibers. As a result the lens thickens, and the curvature increases which effectively increases the optical power of the lens and of the eye (Figure 2.1). With age, we progressively lose the ability to accommodate, leading to a loss of near visual function; a condition known as presbyopia. The origins of presbyopia are still not well understood, but the most prevalent theory is that presbyopia is due to a stiffening of the lens with age, making it more difficult to deform in response to an accommodation stimulus (Helmholtz, 1855; Glasser & Campbell, 1998; Kasthurirangan et al, 2003; Koretz et al, 1994; Koretz et al, 2001; Koretz et al, 2004).

Presbyopia affects everyone above the age of 45-50. It can be easily treated by simple optical corrections, such as reading glasses, but reading glasses do not restore the normal dynamic visual accommodative function. Of an estimated 1.04 billion people worldwide with presbyopia, more than half have no correction or inadequate correction (Holden et al, 2008). As the world population ages and is becoming more active in later stages of life, there is a demand for procedures that restore a normal dynamic accommodative response (Manns et al, 2004). As with LASIK for myopia, a subject may elect to undergo a surgical procedure to eliminate the need for glasses not only for cosmetic or psychological considerations, but also for increased comfort, quality of life, and productivity in occupations that require near work (Lazon de la Jara et al, 2011; Pascolini & Mariotti, 2012).

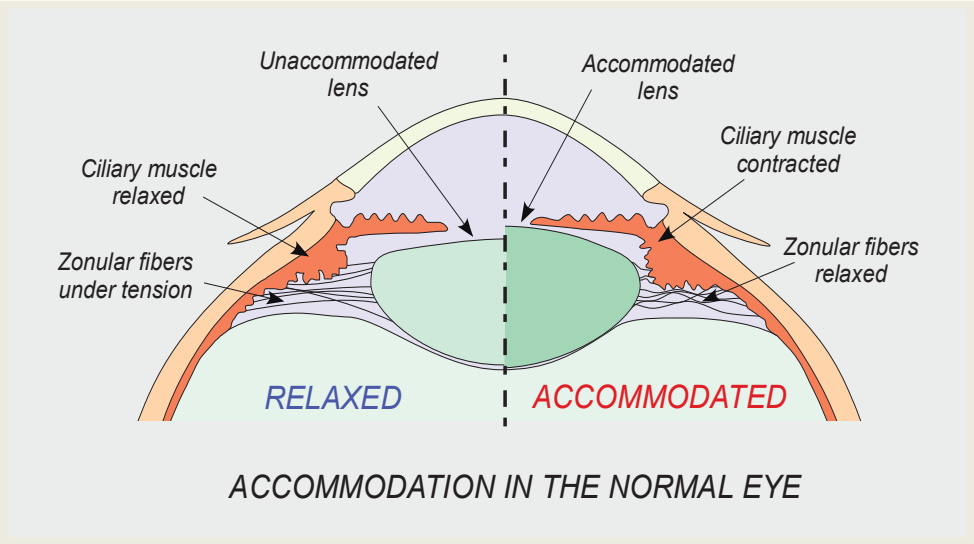

Figure 2.1: Sagittal cross-section of the eye demonstrating the differences in the ciliary muscle, the zonular fibers, and crystalline lens when relaxed and accommodated (Manns et al, 2004).

2.2 Surgical Presbyopia Correction Techniques

2.2.1 Restoration of Near Vision

There exist many surgical techniques for the restoration of near vision, which approach correction via modification of various ocular structures, and use various optical principles of operation. Multifocal intraocular lenses (IOL) create foci at different axial positions, providing a best focus for near, intermediate, and distance vision. This is done using diffractive or refractive optics. Diffractive IOLs use a rotationally symmetric surface echelette pattern that is calculated to produce a diffraction pattern resulting in multiple distinct focal planes, typically one for far, intermediate, and near vision. Refractive IOLs have multiple concentric zones with varying curvature designed to produce different powers, effectively creating different foci. The major difference between these multifocal types is the effective aperture of each focal plane. Since the refractive IOL requires different curvatures for far, near, and intermediate vision, each focal plane uses a different zone of the aperture, whereas the diffractive IOL uses the entire aperture for each focal plane.

Studies evaluating the post-surgical outcomes of multifocal IOL implantation show excellent performance in uncorrected and corrected near visual acuity (Alfonso et al, 2007; Brito et al, 2015; Mastropasqua et al, 2015). Alfonso et al evaluated 6-month postoperative visual acuity and patient satisfaction results in 1,320 eyes and show a best binocular uncorrected distance visual acuity of 20/40 or better in 95% of eyes, and a best binocular uncorrected near visual acuity of 20/40 or better in 100% of eyes. Intermediate visual acuity varied depending on the distance tested and was not as good as the aforementioned results.

Overall, patients are satisfied with their vision, although discomfort from glare and halo effects were reported.

One of the issues with multifocal IOLs is the potential for decreased contrast sensitivity (Vilupuru et al, 2015). Contrast performance has been found to significantly decrease in distance vision (Montes-Mico & Alio, 2003) and is poorer with diffractive IOLs versus refractive IOLs (Pieh et al, 1998). Multifocal IOLs also exhibit an increased sensitivity to a decrease in performance due to tilt or decentration. Small amounts of translation, decentration on the order of 0.4 mm and tilt within 4 degrees, can drastically reduce visual quality (Soda & Yaguchi, 2012; Montes-Mico et al, 2012).

Corneal procedures that have been used for the restoration of near vision include laser assisted in situ keratomileusis (LASIK), photorefractive keratectomy (PRK), conductive keratoplasty (CK) and corneal inlays. The application of LASIK and PRK for treating presbyopia relies on monovision, multifocal, or transitional corneal ablation patterns procedures. These techniques alter the corneal curvature in different regions, effectively changing the corneal refraction to compensate for the near visual losses while still providing distance vision. Monovision is the correction of one eye for near vision and one for distance vision (Farid & Steinert, 2009). Monovision procedures have a patient satisfaction rate between 72% and 96% (Torricelli et al, 2012). Complications include decreased stereoacuity, loss of contrast sensitivity, and a difficulty acclimating to the focal differences in each eye.

CK is a collagen shrinking procedure using radiofrequency energy to correct hyperopia that has also been used for presbyopia correction in older patients. Application of the radiofrequency energy to the cornea in a ring pattern at multiple locations steepens

the shape of the cornea, effectively increasing its dioptric power (Du et al, 2007). A study has shown six months after the procedure, 85% of patients had an uncorrected visual acuity of 20/25 for distance and a near uncorrected visual acuity of 20/35. A major setback of this procedure is the gradual regression of its corrective effects. A study conducted by Esquenazi et al (2006) on patients monitored after conductive keratoplasty surgery show a regression rate of 26%, 36%, and 39% after 4, 6, and 8 weeks respectively.

Corneal inlay (AcuFocus; AcuFocus Inc, Irvine, CA) is a procedure in which a thin anterior flap is made in the cornea, and an aperture is inserted between the flap and corneal surface. The aperture increases the depth of field of the eye and therefore improves near visual performance (Figure 2.2). Studies have shown high success rates with functional near and distance vision (Seyeddain et al, 2013). A considerable limitation in this technique is the loss of contrast sensitivity (Torricelli et al, 2012). In a study done by Tomita et al. (2012), patients with corneal inlays also complained of having mild difficulty with night vision activities, such as driving.

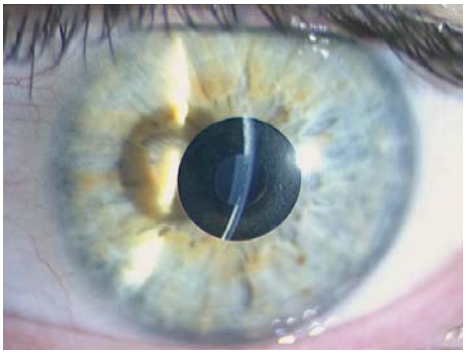

Figure 2.2: Slit lamp image of the human eye with corneal inlay (Seyeddain et al, 2013).

Another depth of field near vision restoration approach is the use of miotic eye drops, which cause constriction in the pupil. In a study by Abdelkader (2015) involving 48 emmetropic and presbyopic subjects, miotic eye drops were applied to the non-dominant

eye of 24 of the subjects, with the remainder receiving a placebo. The results show an improvement in near visual acuity in all subjects that received the drops. The downside of this approach is the need to reapply the drops after a few hours, which may deter patients from pursuing this treatment.

2.2.2 Restoration of Accommodation

Looking at the aforementioned methods for tackling presbyopia correction, it is clear that a definitive solution does not exist. All of these techniques address the symptoms of presbyopia, but do not attempt to restore normal accommodative function to the eye.

Accommodative IOLs are a relatively new approach to providing patients dynamic vision, and form the largest group of currently available accommodation restoration solutions involving the crystalline lens. Accommodative IOLs are designed to exhibit a shift in position or conformation with the contraction of the ciliary muscle during accommodation. These lenses currently have one of three designs; single optic, dual optic, or deformable (Figure 2.3).

Single and dual optic accommodative IOLs rely on translation of the optical element(s) to produce a change in focus of the eye. The single optic design has been shown to provide good quality distance vision, but poor improvement in near vision (Cleary et al, 2010; Alio et al, 2012; Zamora-Alejo et al, 2013). The response of the IOL to the accommodative stimulus and the shift of the lens is minimal at best, and at times unapparent (Waring IV & Berry, 2013; Marcos et al, 2014). The dual-optic IOL is meant to increase the potential accommodative range over that of the single optic by using two optical elements and increasing the optical power of the moving lens (McLead et al, 2003; Ho et al, 2006). The amplitude of accommodation is proportional to the power of the lens and

the amount of its translation. Therefore, a greater power lens would mean a greater eye power change per unit of movement. This higher power anterior operative lens is compensated for by a static minus posterior lens. Studies show a best uncorrected near visual acuity of 20/40 or better in all patients after 6 months (Ossma et al, 2007; Bohorquez & Alarcon, 2010; Marques & Castanheira-Dinis, 2014).

Deformable accommodative IOLs are meant to exact a lens curvature change in response to ciliary muscle contraction (Ben-nun & Alio, 2005). In one particular design, a fixed aperture against which a flexible gel-filled bag sits conforms as a contraction in the ciliary muscle pushes this malleable bag against the fixed aperture, changing the curvature of the bag. This type of IOL is still in the early development stages with very little research on its performance. One study by Alio et al (2009) shows that the deformable IOL does improve near visual ability in 10 eyes evaluated 6 months postoperatively.

Another accommodation restoration approach looks to modify the natural crystalline lens rather than replace it. Femtosecond lentotomy uses femtosecond pulsed laser ablation applied radially and at different depths within the lens to disrupt the lens tissue in an attempt to increase malleability (Myers & Krueger, 1998; Krueger et al, 2005). Animal trials of the technique demonstrate feasibility without inducing cataract formation (Lubatschowski et al, 2010). However, the procedure is still in its early developmental stages and its clinical efficacy remains to be demonstrated. A study by Reggiani Mello and Krueger (2011) reported on a human subjects trial performed on 14 subjects in the Philippines. Results show a variable improvement in objective and subjective accommodation dependent on the laser pulsing and energy pattern applied.

Figure 2.3: (Left) A single-optic IOL and a demonstration of its principle of operation (www.marineyes.com). (Middle) A dual-optic accommodating IOL, with both optics joined via the IOL's haptics (Bohorquez & Alarcon, 2010). (Right) A deformable IOL with components labeled. Note how the optic sits on the capsular bag (Alio et al, 2009).

The lens is also just one part of the entire accommodative plant. The ciliary muscle, and the zonular fibers that interface it to the lens, are also being addressed to affect restoration of accommodation. Anterior ciliary sclerotomy is a procedure in which incisions are made in the sclera located over the ciliary muscle in order to expand the space between the lens and ciliary body. This treatment has been shown to provide a very limited temporary increase in accommodative power, and the incisions made gradually heal, meaning the procedure is eventually reversed, rendering this procedure obsolete (Glasser, 2008). Scleral expansion implants function under the same principle, in which this expansion creates taut zonular fibers to flatten the lens. Scleral expansion has been shown to provide very small increases in near vision (Qazi et al, 2002), however the procedure is very controversial because it relies on a flawed theory of accommodation and presbyopia (Mathews, 1999; Ostrin et al, 2003).

Phaco-Ersatz (Parel et al, 1986) is a collaborative research initiative intended to restore dynamic vision in presbyopes. The surgical procedure was originally proposed by Dr. Jean-Marie Parel in the late 1970s. Since then, the project has become an international endeavor, involving the Brien Holden Vision Institute in Sydney Australia, the LV Prasad Eye Institute in Hyderabad India, and the Ophthalmic Biophysics Center (OBC) of the

Bascom Palmer Eye Institute. Phaco-Ersatz is a modified cataract surgical procedure. A small opening (capsulorhexis) is made in the anterior capsule of the crystalline lens. The inner contents of the lens are removed, leaving an empty capsular bag. The capsule is then refilled with a polymer exhibiting mechanical properties that allow the lens to expand and contract when the eye is presented an accommodation stimulus (Figure 2.4). There have been some in vitro and in vivo primate studies that demonstrate the basic principle (Haefliger et al, 1987; Haefliger & Parel, 1994; Hao et al, 2012). Koopmans et al (2003) took 9 natural and 10 refilled isolated human lenses and evaluated their ability to change power using a custom lens stretcher and power measurement system. The results showed that the refilled lenses were all capable of changing power similar to a young lens. The in vivo experiments performed on 9 rhesus monkeys demonstrated a restoration of the accommodative amplitude of up to 6.3 D, although the amplitude decreased over time, and in three cases was reduced to 0 D (Koopmans, 2006). The lens refilling procedure is still under development.

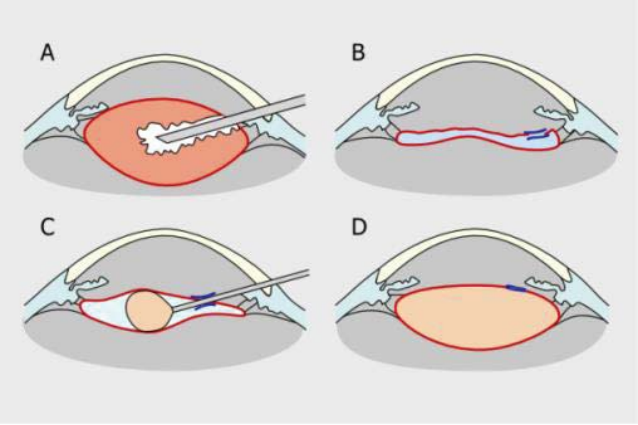

Figure 2.4: Phaco-Ersatz procedural steps. A: A hole is made in the lens capsule and the lens' inner contents are removed. B: Empty bag after removal of contents. C: A polymer is injected into the capsule through the same hole (capsulorhexis). D: Refilled crystalline lens (adapted from Parel et al, 1986).

In summary, there are a number of approaches for the restoration of accommodation, but a limitation to their development is the lack of a means by which to objectively assess their efficacy. Most of the assessment is done subjectively and does not truly measure the accommodative function. This lack of an objective standard is what has allowed controversial procedures such as scleral expansion to persist. The validity of other techniques that rely on unproven concepts for the restoration of accommodation, such as femtosecond lentotomy, remains unchecked. The reliance on subjective assessments makes it difficult to evaluate any of these procedures once they reach the clinic, bearing a direct impact on patient outcomes. In order to assess the efficacy of this and future accommodation restoration techniques, there exists a need for a system that can objectively provide validation and verification of these solutions.

2.3 Assessment of Accommodative Response

One of the obstacles in the development and assessment of presbyopia correction techniques designed to restore accommodation is the lack of a method by which to objectively assess the accommodative response, including the refractive changes during accommodation and the changes in shape or position of the natural, modified and/or artificial lens with the presentation of a near visual stimulus.

Currently, the accommodative response is most frequently assessed subjectively by using a method known as the push-up technique, where the subject is asked to read text that is brought closer to the eye (Anderson et al, 2010). The push-up technique does not truly measure the accommodative ability of the eye; it measures near visual focus. There is always some residual ability for a subject to see at different distances (depth of field),

even in the absence of an accommodative change in the lens (Kasthurirangan et al, 2003). This technique provides no information on the change of lens power with accommodation.

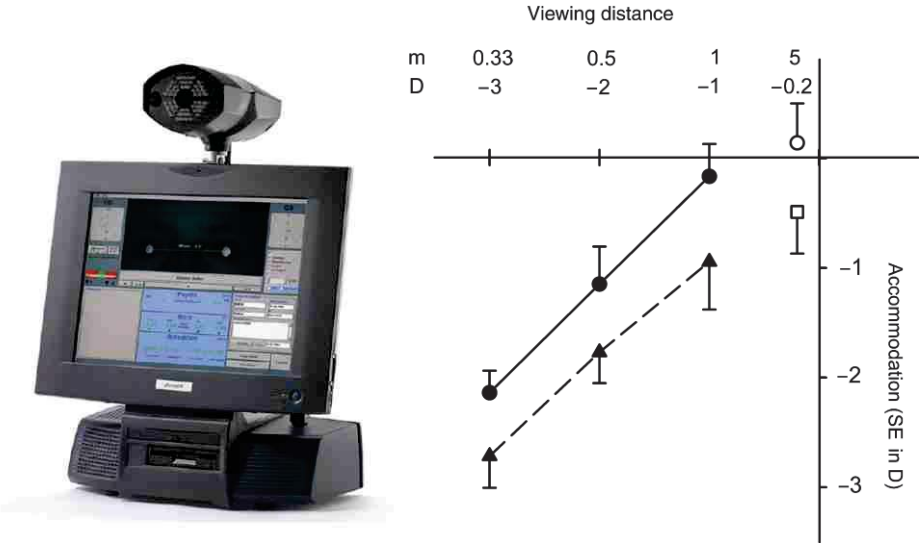

Figure 2.5: (Left) The PowerRef II photorefractor (www.plusoptix.com). (Right) Results of an experiment performed to evaluate accommodative response measured with the PowerRef II and the Canon R1 autorefractor. The photorefractor tends to underestimate accommodative response (Jainta et al, 2004).

Objective methods for determining the accommodative response of the eye emerged with the advent of commercial systems that can measure dynamic refraction. Eccentric photorefraction uses infrared point sources to illuminate the eye and records the intensity distribution in the pupil plane using a camera. There is a gradient of intensity in the pupil that is directly related to the amount of defocus. The Power Ref II (Plusoptix, Nuremberg, Germany) (Figure 2.5) is an autorefractor based on this technique that can accurately measure mild to moderate ametropia (Hunt et al, 2003). This modality is capable of measuring refraction in real time, but has a long working distance, typically one meter, making controlled delivery of a distant, intermediate, and near target during measurement difficult (Wesemann et al, 1991).

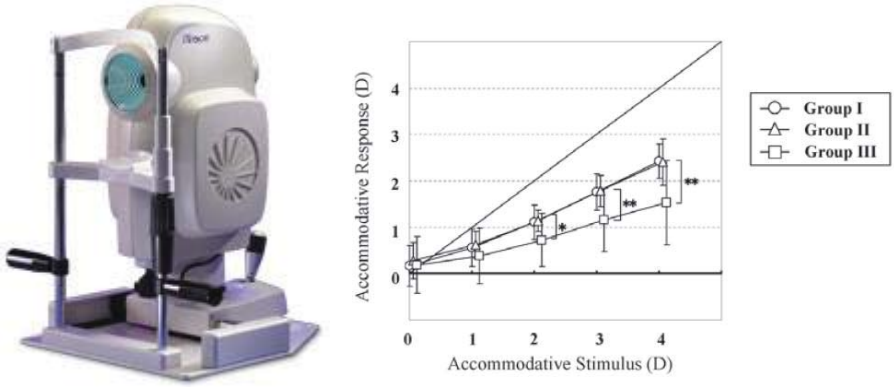

Figure 2.6: (Left) the iTrace open-field laser ray-tracing aberrometer (www.traceytechnologies.com). (Right) Results showing the accommodative response measured using the iTrace with up to 4 D stimulation utilizing a push up method. Measurements were taken in three groups: I, 20-29; II, 30-39; III, 40-49. The accommodative response lags greatest in Group III (Iida et al, 2008).

The iTrace (Tracey Technologies, Houston, TX) is an open-field laser ray-tracing (LRT) aberrometer (Figure 2.6) that can quantify objective accommodation. The LRT measures the position of a series of scanned single source spots back-projected from the retina. The source position is swept over a predefined pupil and the slopes of the rays returning from the eye are measured and processed to produce an aberration map. Refraction is calculated from the aberration coefficients. This system has been used to assess changes in ocular aberrations and refraction with accommodation (Li et al, 2011; Gabriel et al, 2015). In a study by Gabriel et al (2015), measurements of refractive changes in 50 eyes were evaluated at 5 different refractive states. They found increased uncertainty in the measurement with increased accommodative demand. Also, the LRT obtains a static measurement of the eye's refractive state. It does not measure the dynamic optical behavior of the eye during stimulated accommodation.

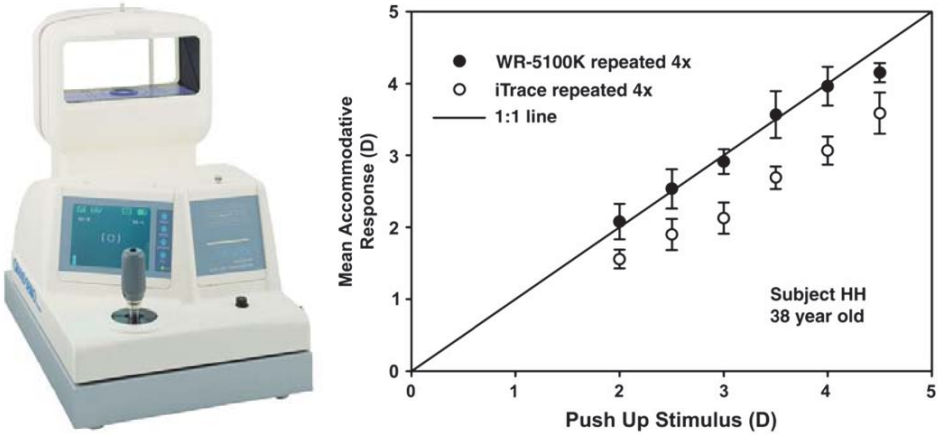

Figure 2.7: (Left) the Grand Seiko WR-5100K as viewed from the position of the observer (image obtained from aitindustries.com). (Right) Results showing the accommodative response of a 38 year old subject as measured with the Grand Seiko and the iTrace. The iTrace underestimated the accommodative response when compared to the Grand Seiko values (Win-Hall & Glasser, 2005).

Open-field autorefractors, which measure changes in the conformation of an infrared ring or parallel bars imaged onto the retina, have been used in the study of accommodation (Win-Hall et al, 2007; Wolffsohn et al, 2004). Open-field autorefractors, such as the Grand Seiko WR-5100K (Grand Seiko Co., Hiroshima, Japan) or Shin Nippon SRW-5000 (Rexxam Co., Osaka, Japan) allow for binocular stimulation through their measurement beam splitter (Figure 2.7). Typically, the subject is presented with a series of letters mounted to a slide rule which is positioned at different distances to induce a certain amount of accommodative change. Evaluation of such devices in the dynamic study of accommodation have provided repeatable results with strong correlation to static measurements obtained with the same device and inter-instrumentation comparisons (Wolffsohn et al, 2006; Win-Hall et al, 2008; Win-Hall et al, 2010). As with LRT, the limitation comes from the accommodation stimulus. The layout of an open-field autorefractor limits the maximum potential stimulus applicable to the uncorrected eye and is not readily adaptable for integration with an OCT system for ocular biometry.

Shack-Hartmann wavefront aberrometry has been shown to provide repeatable, real-time refraction measurement (Cheng et al, 2003). A Hartmann-Shack wavefront sensor contains a lenslet array positioned a focal length away from an image sensor. With an undistorted planar wavefront, the lenslet array images the wavefront as evenly spaced spots onto the sensor. A distorted wavefront is imaged as off-centered spots, and analysis of this gradient shift in spot position provides low and high order aberration information. The principles of Shack-Hartmann wavefront aberrometry and its application to the study of accommodation will be described in more detail in the following chapter.

2.4 Anterior Segment Biometry

There are currently a number of modalities that can image the lens and anterior segment of the eye, such as the Scheimpflug camera, ultrasound biomicroscopy, and optical coherence tomography.

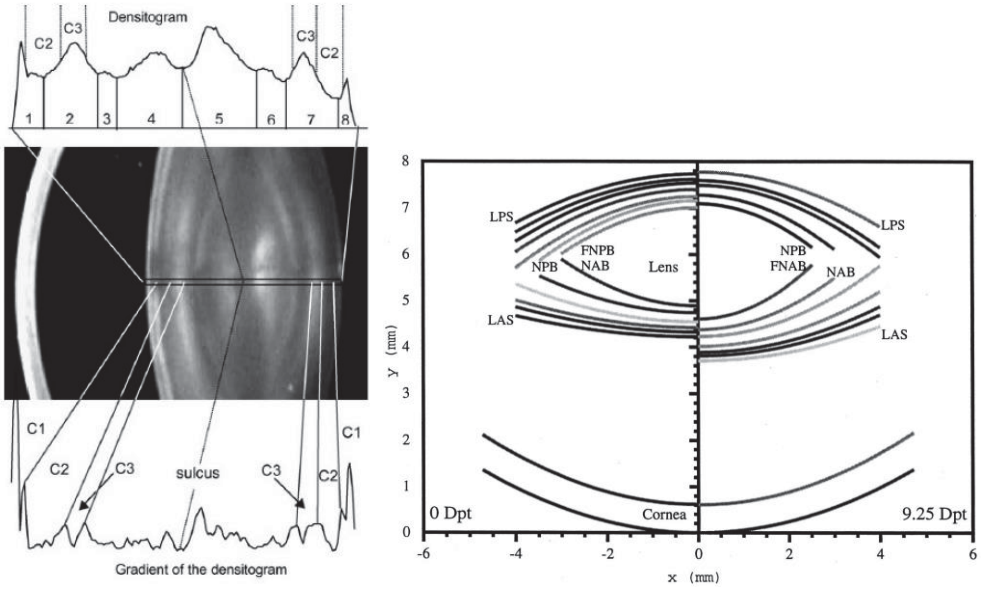

Figure 2.8: (Left) Scheimpflug image of the anterior segment of the eye. The densitogram shows separation of the layers of the crystalline lens (Dubbelman et al, 2001). (Right) A sagittal map of the layers of the crystalline lens made from data obtained with a Scheimpflug imaging system. The image shows a 20 year old subject in an unaccommodated (left) and accommodated (right) state (Koretz et al, 2002).

Scheimpflug imaging, which uses slit-beam illumination detected by a tilted camera to acquire cross-sectional images of the anterior segment, was one of the first modalities used to quantify the changes inside the eye during accommodation and with the aging eye (Brown et al, 1973; Dubbelman et al, 2001; Koretz et al, 2002) (Figure 2.5). Dubbelman et al (2003) have described the different layers of the crystalline lens, known as zones of discontinuity, and have measured how each zone changes with accommodation using a Nidek Eas-1000 Scheimpflug camera (Nidek Co., Japan). Koretz et al applied Scheimpflug imaging to the measurement of the change in radii of curvature of each layer of the crystalline lens and cornea during accommodation. Scheimpflug imaging, although it is a high resolution modality, is difficult to align, limiting its practicality for real time imaging of the dynamic eye (Koretz et al, 2004).

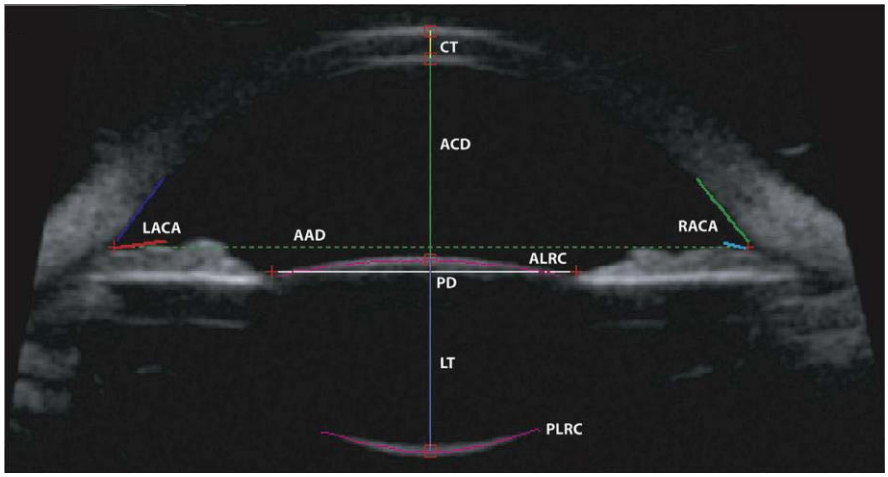

Figure 2.9: Tomographic image of the anterior segment acquired with ultrasound biometry with measured biometric parameters labeled. AAD: angle-to-angle distance; ACD: anterior chamber depth; ALRC: anterior lens radius of curvature; CT: corneal thickness; LACA: left anterior chamber angle; LT: lens thickness; PD: pupil diameter; PLRC: posterior lens radius of curvature; RACA: right anterior chamber angle (Ramasubramanian & Glasser, 2015).

Ultrasound biomicroscopy (UBM) is a contact, tomographic imaging modality capable of acquiring images of the anterior segment (Figure 2.9). Ramasubramanian and

Glasser (2015) have measured the accommodative optical response and UBM biometry and correlated the data to obtain relationships between the response and the change in the ocular dimensions. Their results show correlation to those obtained with other biometric methods, such as optical coherence tomography and magnetic resonance imaging. Note that all measurements of accommodative response were done in a static state, so dynamic accommodation was not measured. Another limitation of this modality is that refraction and biometric information are not acquired simultaneously per simulated accommodative state, since the contralateral eye is stimulated. This may over- or underestimate the accommodative response attributed to the biometric changes in the anterior segment obtained from UBM.

Optical coherence tomography (OCT) is a well establish imaging modality in ophthalmology that has been shown to be capable of imaging anterior segment of the eye in real-time (Radhakrishnan et al, 2001). Both time-domain and spectral-domain OCT systems can be used for imaging the eye, but only spectral-domain has sufficient speed to acquire images with sufficient depth in a reasonable time. However, there exists an intrinsic trade-off for spectral-domain OCT imaging involving image resolution, detection sensitivity, and imaging depth. Obtaining a full picture of the anterior chamber during accommodation was a challenge resolved by new spectral-domain OCT imaging technology and methods that extend the imaging depth. Richdale et al (2008) measured the change in crystalline lens thickness with accommodation using a commercial OCT system (Visante OCT), and the results show values comparable to those obtained with Scheimpflug, and ultrasound imaging. However, the commercial system provides a limited depth, with no full anterior segment imaging capability. New line-scan cameras with

increased number of pixels recently allowed extension of the imaging range (Grulkowski et al, 2009). Ruggeri et al (2012), at the Ophthalmic Biophysics Center, demonstrated whole anterior segment imaging in real time during accommodation via the implementation of an optical switching technique which further extended the imaging range. This approach will be explained in detail in a Chapter 5. Shao et al (2013) have demonstrated real-time whole anterior segment imaging, with ciliary muscle imaging, during accommodation using a similar approach.

2.5 Project Significance

As described above, there are techniques to measure refraction during accommodation. Techniques for performing anterior segment biometry also exist, with OCT being the most convenient method. Yet, there is currently no system that combines all of the above. The goal of the project is to develop a method to simultaneously measure the objective dynamic optical and mechanical accommodative response in vivo. The designed system integrates an extended-depth anterior segment SD-OCT system, a trans-scleral SD-OCT system, a Shack-Hartmann-based autorefractor, an accommodation target, and image processing to quantify changes in lens shape, ciliary body shape, and optics during accommodation.

The project is primarily technology-driven. It will improve technical capability, scientific knowledge and, in the long term, clinical practice by:

- **Increasing our understanding of accommodation and presbyopia:** The system will allow studies of the optical and mechanical accommodative response of the lens and its changes with age that will help better understand the age-related changes leading to presbyopia. In particular, the system will

produce the first measurements of the dynamic changes in lens power and curvature during accommodation and allow studies of lens dynamics and its correlation with presbyopia.

- **Objectively assess techniques for presbyopia correction:** Translation of this device to a clinical research setting will provide developers and clinicians the capability to better assess the efficacy of surgical presbyopia correction techniques, while providing a tool capable of objectively evaluating presbyopia and accommodation.

Chapter 3: Development of a High Dynamic Range Autorefractor and Accommodation Stimulus (Aim 1)

3.1 Purpose

The purpose of Aim 1 is to design, build, and test a system that combines a Shack-Hartmann based autorefractor with a dual-channel modified Badal optometer. The autorefractor and accommodation stimulus will allow for real-time measurement of the refractive change during accommodation. This chapter provides a brief description of the principles of wavefront aberrometry, how it is used to obtain ocular refraction information, the stimulation of accommodation, and their application to the system design. The development of an autorefractor capable of measuring dynamic refraction in real-time is necessary to quantify the optical changes of the eye during stimulated accommodation. The integration of an accommodation stimulus with a large potential stimulus vergence and controlled stimulus conditions will allow for the objective measurement of the full accommodative amplitude in an uncorrected state.

3.2 Design Specifications

There are two main components to this portion of the system; the autorefractor and accommodation stimulus. The autorefractor will measure the changes in refraction in real-time and the accommodation stimulus will present a target to the subject in a step-wise fashion to allow for the measurement of the transient accommodative response.

3.2.1 Shack-Hartmann Based Autorefractor

The autorefractor module of the system needed to meet the following design criteria (Figure 3.1):

- Utilize a Shack-Hartmann wavefront aberrometer capable of a spherical refraction measurement range from -20 D to +10 D.

- Linear measurement response, meaning uniform sensitivity across the measurement range.
- Continuous acquisition of measurement, at a minimum rate of 15 Hz.
- A relay system placing the pupil plane of the eye conjugate on the lenslet array of the wavefront sensor.
- A minimum working distance of 100 mm.
- A probe beam wavelength below 800 nm or above 880 nm.
- An alignment camera used to center the measurement system to pupil position.
- Software platform capable of displaying the refractive state change graphically in real time and record the relevant parameters for most processing.
- Changes in refraction need to be filtered in such a way that erroneous data is eliminated while maintaining the integrity of the true vergence response.

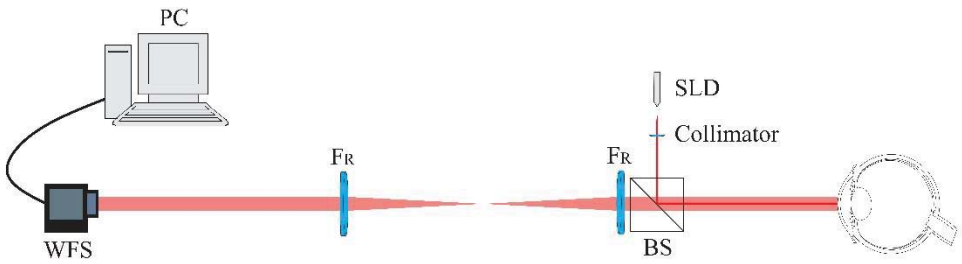

Figure 3.1: Representative sketch of the autorefractor module. WFS: Shack-Hartmann wavefront sensor. FR: Relay lens. BS: Beamsplitter. SLD: Super-luminescent diode.

3.2.2 Accommodation Stimulus

The accommodation stimulus module of the system needed to meet the following design criteria (Figure 3.2):

- A stimulus range with a maximum vergence change of -20 D. This will allow for a maximum stimulus of -10 D in a subject with refractive error at the corneal plane of -10 D.
- A stimulus that will allow for adjustment of the presented visual target. This will allow for future testing of spatial frequency changes and its effect on accommodation.
- A working distance matching that of the autorefractor module.
- A mechanical design providing lateral mechanical symmetry.
- Two channel system to allow for the presentation of a step-stimulus.
- Stimulus must be presented without correction for defocus.

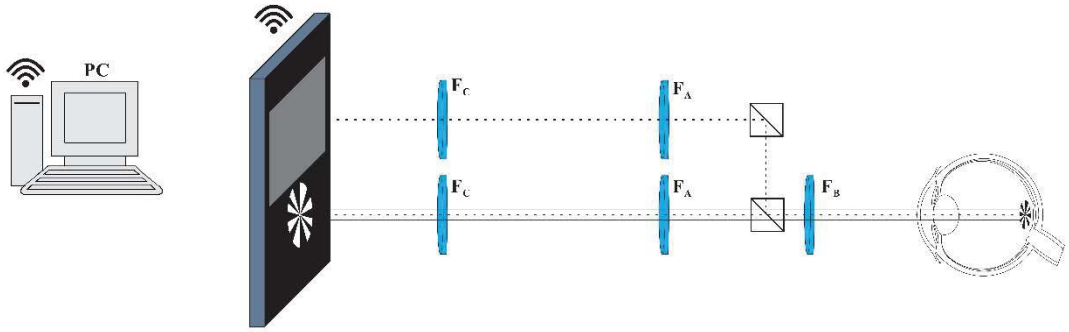

Figure 3.2: Representative sketch of the accommodation stimulus module. The target is presented using a split-screen display communicating wirelessly with a PC. F_A: Auxiliary translating lens. F_B: Badal lens. F_C: Collimating lens.

3.3 Wavefront-Based Refraction

3.3.1 Wavefront Aberrometry

A wavefront of light can be pictured as a 2-dimensional topographical map propagating along the axial z-direction. A planar wavefront, when viewed in profile, appears as a straight line, and a distorted wavefront appears curvilinear. In Figure 3.3, we see an example of this concept; the green beam corresponds to a planar wavefront incident

on the eye, and the red beam is the beam returning from the eye after reflection at the retina. The red beam is affected by the aberrations of the eye, which produce distortions in the wavefront. As with a conventional topographical map, one can represent the wavefront aberration as a two dimensional color map which represents the phase or optical path variation of the wavefront of the returning beam across the pupil of the eye.

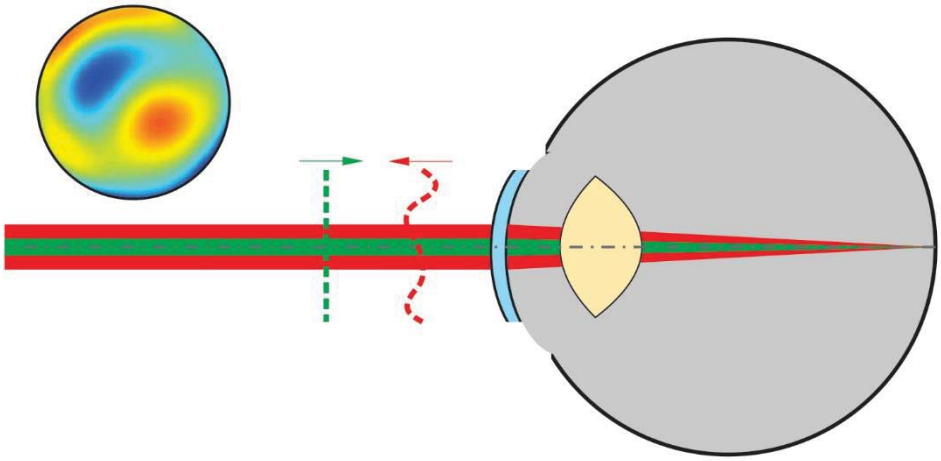

Figure 3.3: A planar wavefront (green) propagating along the axial z direction is incident on an aberrated eye. The retinal reflection (red) returns a distorted wavefront as the optical elements of the eye create optical path differences across the pupil. (Top Left) A radial aberration map of the reflected wavefront showing the variation of the optical path difference of the aberrated wavefront across the pupil.

The most common way of modeling the wavefront leaving the eye is by using Zernike polynomials. Zernike polynomials (Z) are an orthonormal polynomial set. Utilizing the Zernike polynomials, the wavefront W of the eye can be described mathematically as the sum of the scaled Zernike basis functions:

$$W(\rho,\theta) = \sum_{i=0}^{\infty} a_i Z_i(\rho,\theta) \qquad [3.1]$$

Where ρ and θ are the polar coordinate in the pupil plane, a_i is the i^{th} Zernike coefficient, and Z_i is the i^{th} Zernike polynomial. Each Zernike coefficient corresponds to a certain type of aberration. Table 3.1 summarizes the Zernike polynomials and their names

up to the fourth order, which are used in calculations of ocular aberrations throughout this dissertation. Each of the polynomials represents a type of aberration, and this aberration's influence on the wavefront map are depicted in Figure 3.4.

The Zernike coefficients of order two, which correspond to defocus and astigmatism, can be used to calculate values of ocular refraction, including sphere, cylinder, and axis. For a pupil of radius R, the refraction values (Sphere, Cylinder, and Axis) are given by (Dai, 2008):

$$S = -\frac{4\sqrt{3}a_2^0}{R^2} + \frac{2\sqrt{6}\sqrt{(a_2^{-2})^2+(a_2^2)^2}}{R^2} \quad [3.2]$$

$$C = -\frac{4\sqrt{6}\sqrt{(a_2^{-2})^2+(a_2^2)^2}}{R^2} \quad [3.3]$$

$$A = \frac{1}{2}\tan^{-1}\left(\frac{a_2^{-2}}{a_2^2}\right) + \frac{\pi}{2} \quad [3.4]$$

Where a_2^0, a_2^{-2}, and a_2^2 are the Zernike coefficients for defocus, y-astigmatism, and x-astigmatism respectively. From these values we can also derive the expression of spherical equivalent refraction in terms of the Zernike coefficients. Since the spherical equivalent is equal to Sphere plus one half the Cylinder, we get:

$$SEQ = S + \frac{C}{2} = -\frac{4\sqrt{3}a_2^0}{R^2} \quad [3.5]$$

This expression demonstrates that the spherical equivalent refraction is dependent only on the defocus Zernike coefficient.

Table 3.1: Zernike polynomials up to the fourth order.

i	*n*	*m*	Zernike Polynomials	Name
0	0	0	1	pistom
1	1	-1	$2\rho \sin\theta$	y-tilt
2	1	1	$2\rho \cos\theta$	x-tilt
3	2	-2	$\sqrt{6}\rho^2 \sin 2\theta$	y-astigmatism
4	2	0	$\sqrt{3}(2\rho^2\text{-}1)$	defocus
5	2	2	$\sqrt{6}\rho^2 \cos 2\theta$	x-astigmatism
6	3	-3	$\sqrt{8}\rho^3 \sin 3\theta$	y-trefoil
7	3	-1	$\sqrt{8}(3\rho^3 - 2\rho) \sin\theta$	y-coma
8	3	1	$\sqrt{8}(3\rho^3 - 2\rho) \cos\theta$	x-coma
9	3	3	$\sqrt{8}\rho^3 \cos 3\theta$	x-trefoil
10	4	-4	$\sqrt{10}\rho^4 \sin 4\theta$	y-quadrafoil
11	4	-2	$\sqrt{10}(4\rho^4 - 3\rho^2) \sin 2\theta$	y-secondary astigmatism
12	4	0	$\sqrt{5}(6\rho^4 - 6\rho^2 + 1)$	spherical aberration
13	4	2	$\sqrt{10}(4\rho^4 - 3\rho^2) \cos 2\theta$	x-secondary astigmatism
14	4	4	$\sqrt{10}\rho^4 \cos 4\theta$	x-quadrafoil

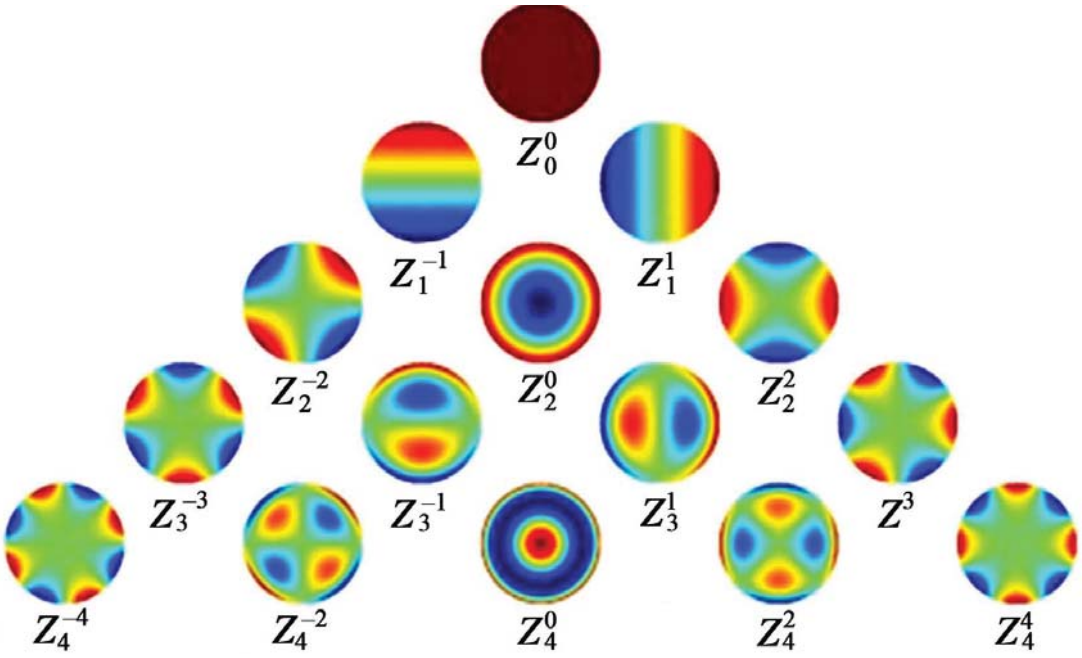

Figure 3.4: Pictorial description of the Zernike polynomials up to the fourth order. Polynomials are defined in Table 3.1. (Adapted from Spors et al, 2012).

3.3.2 Shack-Hartmann Wavefront Sensing

The most common approach to measure the wavefront aberrations of the eye is by means of Shack-Hartmann wavefront aberrometry. Shack-Hartmann wavefront aberrometer is particularly well-suited for the purpose of dynamic aberrometry or refraction because it can measure aberrations in real-time with high sensitivity. The Shack-Hartmann wavefront aberrometer is capable of measuring the wavefront of the entire pupil at once within a very short amount of time, making it an excellent choice for the study of dynamic accommodative response.

The Shack-Hartmann wavefront sensor samples the ocular wavefront via a lenslet array that is located in a plane conjugate to the pupil of the eye. The lenslet array focuses the wavefront onto an electronic imaging sensor. If a planar wavefront parallel to the plane of the array is incident onto the lenslet array, each lenslet of the array will produce a spot image focused on the imaging sensor at the focal point of the lenslet. When compounded, the lenslet array produces a regularly spaced spot field image on the sensor. If an aberrated wavefront is incident onto the lenslet array, each individual lenslet will produce a spot image that will no longer lie at the focal point of the lenslet, but will be offset in the x and y directions (Figure 3.5). The offset is determined by the local slope of the wavefront at the position of the lenslet and the focal length of the lenslet. The local slope of the wavefront can therefore be calculated from the measured spot image offset. At each lenslet, the relationship between the local wavefront slope and the Zernike coefficients can be expressed as:

$$\frac{\partial W}{\partial x} = \sum_{i=1}^{J} a_i \frac{\partial Z}{\partial x} \qquad [3.6]$$

$$\frac{\partial W}{\partial y} = \sum_{i=1}^{J} a_i \frac{\partial Z}{\partial y} \qquad [3.7]$$

From the local slope at each lenslet, the entire wavefront across the pupil can be determined using one of a number of reconstruction techniques (i.e. zonal or modal reconstruction [Panagopoulou & Neal, 2005]).

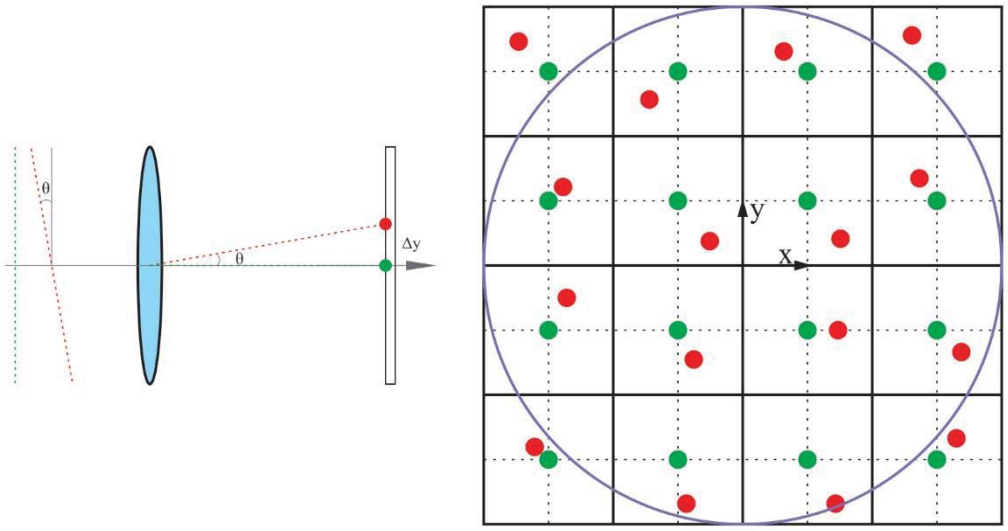

Figure 3.5: (Left) A lenslet sampling a portion of a planar (green) and aberrated (red) wavefront with displacement shown in the y-direction. The angle θ is equal to the wavefront slope measured from the normal to the axis and the two-dimensional ray axis between the nominal and shifted spot position. (Right) The nominal (green) and aberrated (red) spot positions of a 4 x 4 lenslet array within their intended sub pixel arrays. The purple pupil represents the measurement area.

Liang et al (1994) were the first group to publish aberrometric information of the human eye using a Shack-Hartman wavefront sensor. They used a relay system to place the pupil conjugate onto a 7x7 sampled lenslet array of the wavefront sensor with a magnification of 1.85x (Figure 3.6). They obtained repeatable aberrometric measurements that were in close agreement to data obtained subjectively (within 0.5 D in the sphere measurement), and demonstrated the feasibility of using a double-pass system for ocular aberration measurement.

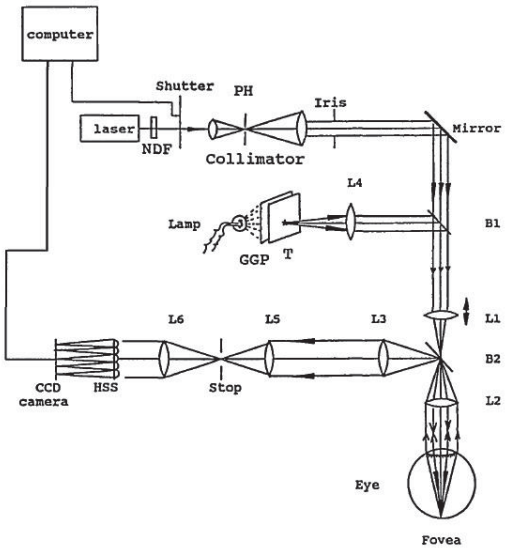

Figure 3.6: Schematic drawing of the system used by Liang et al (1994). NDF: Neutral density filter, PH: Pinhole, GGP: Ground-glass plate, T: Target, L1-L6: Lenses, B1-B2: Beamsplitters, HSS: Hartmann-Shack wavefront sensor.

Shack-Hartmann-based autorefractors have since been used clinically to study refractive surgical outcomes and accommodation (Cheng et al, 2003; Mirshahi et al, 2003; Shneor et al, 2011; Lopez-Miguel et al, 2012).

In ocular Shack-Hartmann aberrometers, the pupil plane is imaged onto the lenslet array using a 4f relay system, or telescope, consisting of two lenses separated by a distance equal to the sum of their focal lengths. This relay system is favored because it provides a compact means by which to place the pupil plane conjugate to the lenslet array of the wavefront sensor and gives a linear measurement response.

3.4 Design Layout and Justification of Shack-Hartmann Autorefractor

3.4.1 General Description

The Shack-Hartmann based autorefractor is comprised of the following components:

- Light source
- Relay optics

- Shack-Hartmann wavefront sensor
- Alignment camera

All components are joined using an optical cage mount system. The light source serves as the probe beam for the measurement of refraction. The autorefractor utilizes a 4f relay system to place the pupil conjugate on the lenslet array of the wavefront sensor. An alignment camera is coupled to the measurement channel of the autorefractor to allow for centration of the pupil to the measurement apparatus.

3.4.2 Light Source

When choosing the light source, there are three major properties that are considered; central wavelength, bandwidth, and maximum output power.

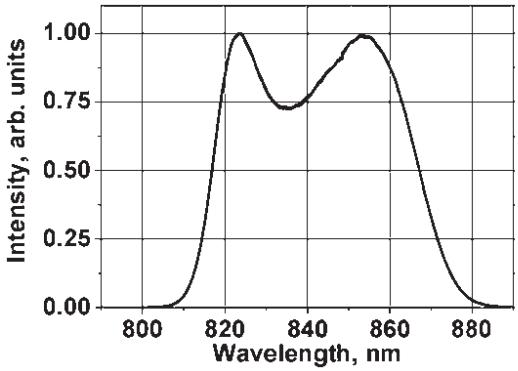

Figure 3.7: Spectral output of the OCT light source. The central wavelength of the autorefractor's light source must fall outside of this band so as not to interfere with the biometric module.

The central wavelength of the light source needs to be below 800 nm or above 880 nm. This is necessary to ensure that the probe beam does not interfere with the OCT system by operating within its wavelength band (Figure 3.7). A light source with a peak wavelength above 870 nm has the benefit of not being visible to the subject and becoming a distraction to target fixation. But the longer wavelength would require a custom-ordered dichroic mirror that would reflect the near-infrared emission of the OCT system and

transmit the visible emission of the accommodation target and the longer near-infrared emission of the wavefront sensor source. On the other hand, a wavelength below 800 nm could potentially be a distraction to the subject when viewing the accommodation target, but it would not require a custom-order dichroic mirror. Due to the high cost of a custom dichroic (approximately $10,000), a light source with a wavelength below 800 nm was selected.

The bandwidth of the light source needs to be narrow (10-20 nm) because the central wavelength selected operates near the cutoff wavelength of the OCT delivery dichroic mirror. A wide bandwidth would see a larger amount of its delivered energy to the eye lost to reflection at the dichroic mirror.

The maximum output power of the light source needs to be large enough to compensate for losses as the beam travels through the optical elements of the system to the eye, and back from the eye to the wavefront sensor. The power will need to be adjusted to ensure safe levels of light delivered to the eye while maximizing the power delivered to the wavefront sensor.

A 750 nm central wavelength super-luminescent diode with a bandwidth of 10 nm and a maximum output power of 2.5 mW was chosen (IPSDS0701C, InPhenix, Livermore, CA). Figure 3.8 shows the spectral output of the selected source.

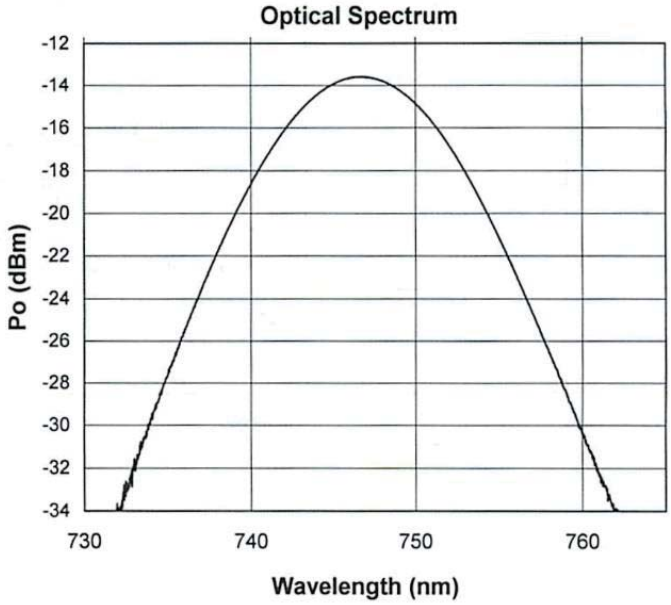

Figure 3.8: Spectral output of the selected SLD probe beam light source. Data is provided by InPhenix.

3.4.2.1 Collimator

The SLD is coupled to a FiberPort collimator (PAF-X-2-B, Thorlabs, Newark, NJ) with an effective focal length of 2.0 mm via a 1 m single-mode patch cable (HI780, Corning, Corning, NY) with mode field diameter of 4.6±0.5 μm and a specified output beam diameter of 0.42 mm. A collimator producing a small output beam diameter was selected to provide a large depth of focus. A large depth of focused is desired to make the measurement less sensitive to changes in axial position of the eye or device during adjustments or measurements and to reduce the effects of axial eye length variations on the retinal spot size. The depth of focus can be estimated by calculating the Rayleigh range of the beam. The Rayleigh range, R, of the beam is the distance away from the beam waist at which the cross sectional area of the beam is doubled. This value is defined by the following expression (Damask, 2004):

$$R = 2\left(\frac{\pi\left(\frac{d}{2}\right)^2}{\lambda}\right) \qquad [3.8]$$

Where d is the beam diameter and λ is the wavelength of the source. When d=0.5 mm, the Rayleigh range for the probe beam is 369.5 mm. Ideally, the position of the eye should be located at the beam waist. Since the collimator is mounted in a fixed position within the system, it is important to evaluate where the beam waist will lie relative to the collimator housing once it is placed in the system. According to the FiberPort specifications provided by Thorlabs, the maximum waist distance is:

$$z = f + \frac{2f^2\lambda}{\pi MFD^2} \quad [3.9]$$

Where MFD is the mode field diameter of the patch cable and f is the focal length of the collimator. For this system, the maximum waist distance is 92.3 mm. This shows that, including the relay optics of the autorefractor module, the subject's eye will fall within the Rayleigh range of the probe beam.

3.4.3 Wavefront Sensor Selection

A commercial off the shelf solution for the wavefront sensor (WFS150-5C, Thorlabs, Newark, NJ) provided the best trade-off between cost and performance (Figure 3.9). This wavefront sensor was selected since it had previously been characterized in the laboratory for another wavefront-based autorefractor design project and had been shown to provide a high dynamic range. The specifications of the device are summarized in Table 3.2. The WFS150-SC utilizes a chrome sub aperture mask to improve spot contrast by limiting the stray light incident on the sensor.

Figure 3.9: Thorlabs Shack-Hartmann wavefront sensor (www.thorlabs.com).

Table 3.2: WFS150-5C Shack-Hartmann wavefront sensor specifications.

Camera Specifications	
Maximum Camera Resolution	1280 x 1024 pixels
Pixel Size	4.65 µm x 4.65 µm
Maximum Aperture	5.95 mm x 4.76 mm
Maximum Frame Rate	15 Hz
Lenslet Array Specifications	
Wavelength Range	300-1100 nm
Effective Focal Length	3.7 mm
Maximum Active Lenslets	39 x 31
Lenslet Pitch	150 µm
Lenslet Size (Ø)	146 mm

3.4.4 Lens Selection

For the autorefractor module, the lenses used to place the pupil conjugate onto the lenslet array needed to meet certain criteria. The linear response provided by using a 4f relay system is desired. The lenses selected also needed to maintain the system compact while still providing a long enough working distance for the integration of other components. Typical wavefront sensor-based autorefractors have a working distance between 60-70 mm. Since the minimum working distance in our application is 100 mm, two 100 mm focal length lenses were selected to be the relay lenses for the wavefront sensor. This selection gives a total measurement system length, from the pupil plane of the

eye to the lenslet array of the wavefront sensor, of 400 mm. The use of two lenses with matched focal lengths provides a 1:1 magnification ratio. A lower magnification ratio would help decrease the size of the system, but it would also decrease the dynamic range by a factor equal to the square of the magnification factor.

3.4.5 Pupil Alignment Camera

The pupil alignment camera selected needed to provide sensitivity in the near infrared, since the probe beam of the wavefront sensor also serves as illumination for the alignment camera. A high-resolution 1/3" monochromatic CCD camera (CMLN-13S2M-CS, Point Grey, Richmond, Canada) was coupled to the measurement channel of the system. A single 25 mm diameter, 30 mm focal length achromatic lens was used to image the pupil onto the image sensor of the camera. The focal length of the lens was selected to produce a magnification of 0.3x, when combined with the 100 mm lens of the wavefront sensor relay system. Since the sensor size is 3.6 mm, the maximum object size that can be imaged by this system is 12 mm, corresponding approximately to the corneal diameter. These parameters will allow for imaging of the entire pupil with tolerance for alignment.

3.4.6 Beamsplitters and Implementation

The beamsplitters used to couple the subcomponents of the autorefractor and accommodation stimulus channels need to efficiently deliver the target stimulus and probe beam to the eye and maximize input to the wavefront sensor from the retinal reflection. The initial autorefractor design utilized cube beamsplitters with 50:50 Reflection: Transmission ratios. This created issues with power losses and reflections. Having the light source coupled to the measurement channel also created heavy reflections from the

beamsplitter surfaces on the alignment camera, making it difficult to visualize the pupil, even when anti-reflection coated beam-splitters were used. For the measurement channel, pellicle beamsplitters are used to eliminate the effect of component internal reflections. The Reflection: Transmission ratios were also optimized to minimize losses in the retinal reflection incident on the wavefront sensor and alignment camera (Figure 3.10).

The power reaching the wavefront sensor was estimated by placing a power sensor and connected to a power meter (918SL and 1930C, Newport, Irvine, CA) at the position of the wavefront sensor. A model eye using a plano-convex lens to simulate the optics of the eye and a diffuse reflector to simulate the retina was placed at the position where the subject's eye would be located during a real measurement. The power reaching the wavefront sensor was approximately 2.6 μW. This value is further attenuated when the dichroic mirror used for the anterior segment biometry mirror is placed in the path. With the dichroic in place, the power incident on the eye is 46 μW and the power reaching the wavefront sensor is 112 nW.

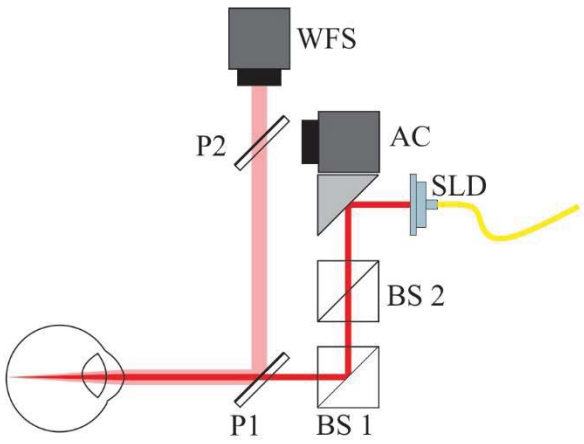

Figure 3.10: Schematic of the optical setup used to relay the probe beam of the wavefront sensor to the eye and the measurement of the return reflection. WFS: Wavefront sensor. AC: Alignment camera. SLD: Superluminescent diode source. P1: 45:55 R:T Pellicle beamsplitter. P2: 8:92 R:T Pellicle beamsplitter. BS 1 and BS 2: 70:30 R:T Cube beamsplitter.

3.4.7 Accommodation Stimulus: Modified Badal Optometer

3.4.7.1 Purpose

The purpose of the accommodation stimulus is to elicit an ocular response from the subject in order to measure the changes in optical refraction and biometry of the eye during accommodation.

The accommodation stimulus module is modeled after the modified Badal optometer as first described by Atchison (Atchison et al, 1995) and implemented by Ruggeri et al (2012) in an OCT-based accommodation biometry system (Figure 3.11). The original design had two major constraints that did not meet the design specifications. First, its maximum potential stimulus was -9.5 D, which falls below the -20 D maximum desired. Also, the physical layout is laterally asymmetric with respect to the subject's sagittal plane, which prevents ciliary muscle imaging on both eyes. The system does not provide space for placement of the trans-scleral OCT probe when the right eye of the subject is imaged.

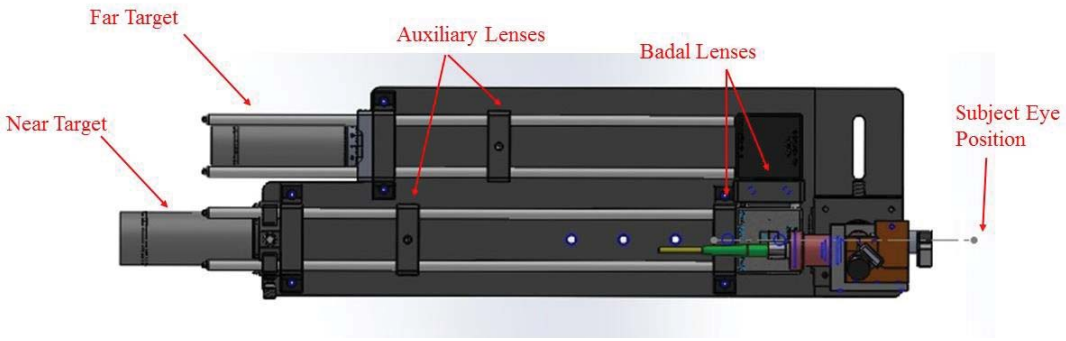

Figure 3.11: A top-view of the original modified Badal optometer accommodation stimulus implemented in the first generation accommodation biometry system. Notice that in this conformation, the system is laterally asymmetrical. (Adopted from a CAD model by Marco Ruggeri, PhD).

3.4.7.2 Lens Selection

The choice of lenses for the modified Badal optometer was defined by Atchison's optical model, where a distant target located at a fixed position away from the Badal lens

is imaged by the Badal/auxiliary lens system (Figure 3.12). The advantage of utilizing a modified Badal optometer as an accommodation stimulus is that this design provides a fixed target position and magnification across the entire vergence range and the addition of an auxiliary lens extends the potential stimulus range. This increased potential stimulus is required to meet the design specifications. A maximum vergence can be achieved when d, the distance between the Badal and auxiliary lens, is equal to zero. The equations below are used to determine the lenses selected for the Badal optometer. Here, Q is the vergence power of the system, M is the magnification of the lens system, F is the power of the Badal lens, and F_a is the power of the auxiliary lens. The equations were entered into MATLAB and the values for the focal lengths of the Badal and auxiliary lens were varied to determine the optimal combination of focal lengths that provides a minimum working distance of 100 mm and the desired vergence range.

$$Q = -F - \frac{F^2(1-dF_a)}{F_a} \quad [3.10]$$

$$Q_{max} = -F - \left(\frac{F^2}{F_a}\right) \quad [3.11]$$

$$M = -\frac{F}{F_a} \quad [3.12]$$

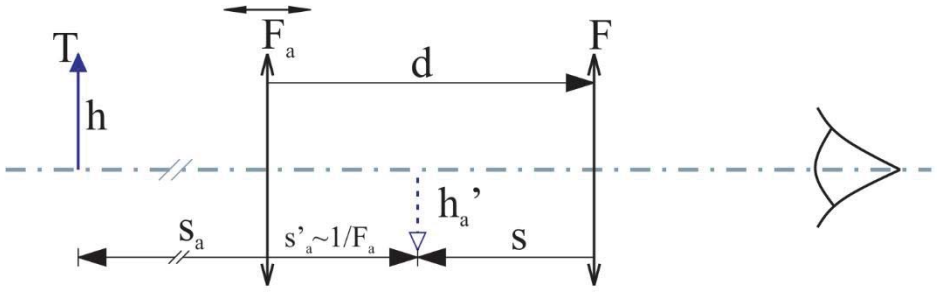

Figure 3.12: Badal optometer with an auxiliary lens imaging a distant target. This makes the auxiliary lens image distance approximately equal to its focal length.

The calculations show that a Badal lens with a 100 mm focal length combined with an auxiliary lens with a 200 mm focal length satisfy the design criteria. Figure 3.13 shows that for every one centimeter of auxiliary lens translation, there is 1 diopter of vergence change. To allow for the desired amount of correction (-10 D to +10 D) and stimulation (up to -10 D), the vergence range should be between -20 D to +10 D. As shown in the graph below, the selected lenses provide a theoretical negative vergence of up to -30 D over the entire desired position range with an angular magnification of -2. The target consists of a display described in Section 3.4.7.3. A 100 mm focal length lens is placed in front of the stimulus to create an infinite conjugate delivered to the Badal system. The combination of the Badal system with the target collimating lens provides a total accommodation stimulus system magnification of -5.

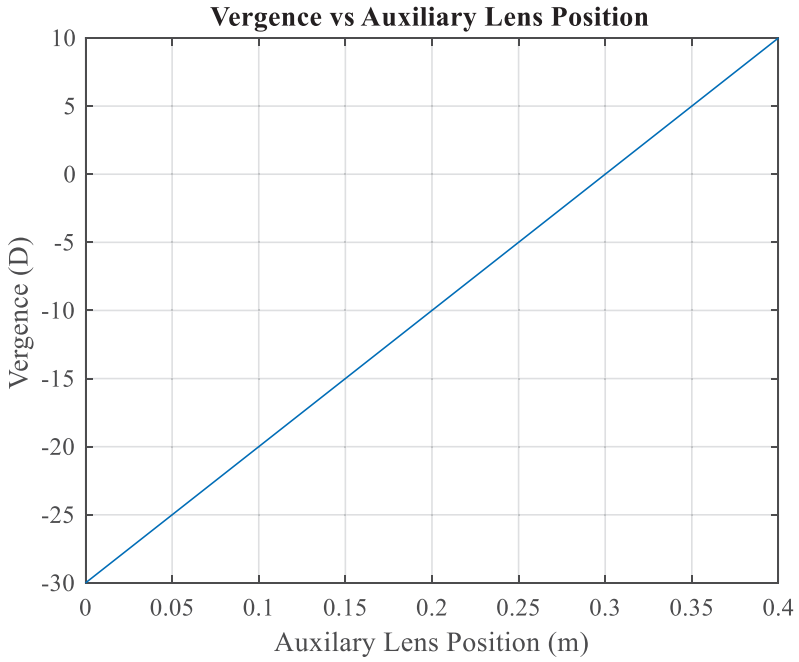

Figure 3.13: Vergence vs. auxiliary lens position.

3.4.7.3 Accommodation Stimulus Design

The design of the accommodation stimulus has progressed through two major revisions. The final design provides an adequate spatial resolution and is compact enough

to be mounted onto the translatable table in combination with the refraction and biometric modules. The first module used a microcontroller (UNO Rev. 2, Arduino, Ivrea, Italy) with two 1.8" Thin-Film-Transistor (TFT) Liquid Crystal Displays (LCD) (ST7735R, Sitronix, Taiwan). Each screen was programmed to exist in two output states: the desired target stimulus and a blank (black) screen. A click switch was wired to the microcontroller to allow the user to toggle between the two output states. The user input needed to be timed to match the timer in the software for triggering the near stimulus signal. This presented with the potential for larger amounts of inter-and intra-operator error. In addition, the resolution and brightness of the display were found to be insufficient.

In order to improve the output resolution through the optics of the Badal optometer and improve ease of integration with the autorefractor's software, the above LCD system was replaced with a cellular phone (Xperia Z1s, Sony, Tokyo, Japan). The resolution of the phone improves output image resolution almost fourfold (223 μm vs 57 μm). The phone communicates with the computer via an ad-hoc desktop mirroring software platform that takes into account the positioning and magnification of the stimulus presented from the PC. The stimulus is integrated into the software platform, meaning that once the program is run, there is no need for user input regarding measurement acquisition, eliminating the output variability.

The psycho-physiological response to a visual stimulus is governed by the target. Many aspects of the target and its presentation, such as spatial frequency, target luminance, and the field of presentation, all play a role in accommodative response. The spatial frequency of the stimulus can selectively increase or decrease the accommodative response elicited from the subject (Matthews & Kruger, 1993; Okada et al, 2005; Strang et al, 2011).

Studies evaluating the impact of spatial frequency on accommodative response show that the greatest amount of accommodation is elicited with a target exhibiting between 3 and 5 cycles per degree (cpd). A cpd above or below these values does not increase the response.

The target's luminance affects the response to the stimulus. As with spatial frequency, there is a range in which the measured response is greatest. Marcos et al demonstrated that the maximum measured accommodation was found with a target luminance of 16 cd/m^2 when the brightness was varied between 0.8 and 50 cd/m^2. Field of presentation, meaning a light target on a dark background or visa versa, also controls the results of accommodation measurements. In the same study by Marcos et al (2012), the presented target was placed on either a light or dark field and accommodation was measured in 7 subjects. The results showed a better response to the dark target presented on a white field (Figure 3.14).

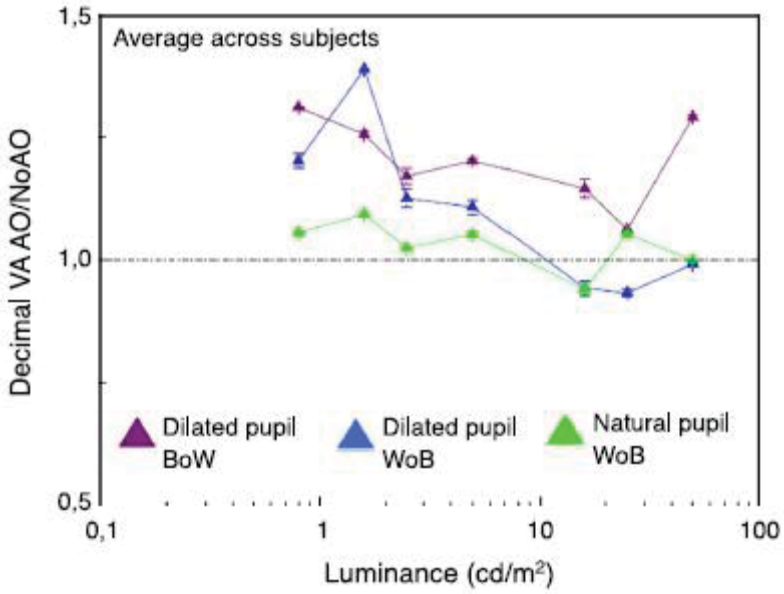

Figure 3.14: Visual acuity vs. luminance for white on black and black on white target presentation (Marcos et al, 2012).

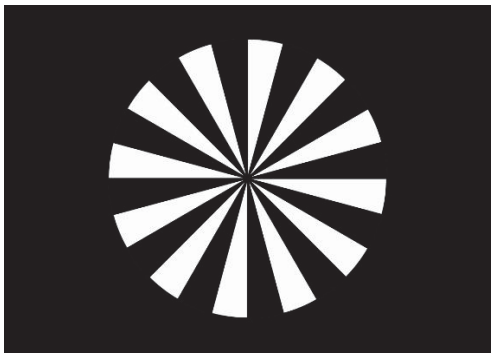

Figure 3.15: Accommodation stimulus, the 12-segment Siemens star.

Based on these considerations, the target that was used was a 12 segment Siemens star (Figure 3.15). The Siemens star was selected because its variable spatial frequency has been shown to provide optimal stimulation (Mathews & Kruger, 1994). It is displayed though the system in such a fashion that the image occupies the entire aperture (Figure 3.16).

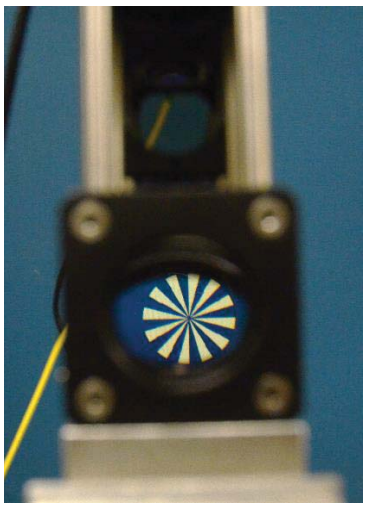

Figure 3.16: Accommodation target as viewed by the subject through the objective lens of the system.

The designed mount for the accommodation target display was machined from Delrin acetyl-resin and contains a shallow sleeve for seating the device. The top edge of the sleeve comes up to the bottom edge of the cellular phone's display, so as to allow for the required alignment and positioning of the device prior to beginning measurement

(Figure 3.17). Once the software is started and the cellular phone's display is on, no further manipulation of the target is necessary.

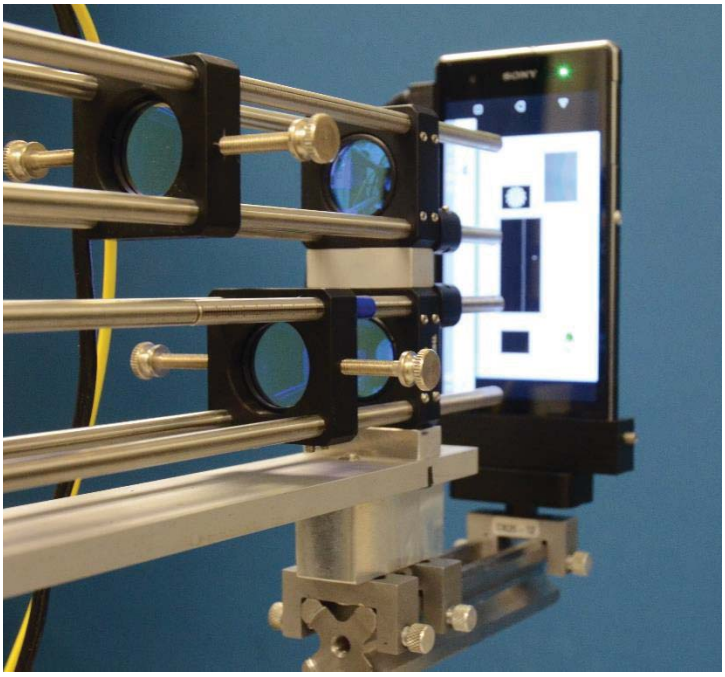

Figure 3.17: The accommodation stimulus as it is mounted to the system. The auxiliary lenses have a #8-32 thumb screw placed on either side of the lens mount to make translation of the lens easier. The accommodation stimulus is presented on the cellular phone by mirroring the display of the graphical user interface.

3.4.8 General Opto-Mechanical Description

The mechanical layout of the system went through a number of revisions from its conception to the final selected design. In the first iteration of the autorefractor module, the probe beam illumination channel was coincident with the measurement channel of the Shack-Hartmann aberrometer. This created an issue with reflections from the cube beamsplitters in the optical path. In the final design (Figure 3.18), the probe illumination is coupled to the accommodation stimulus, reducing reflections and therefore improving the efficiency of the measurement channel.

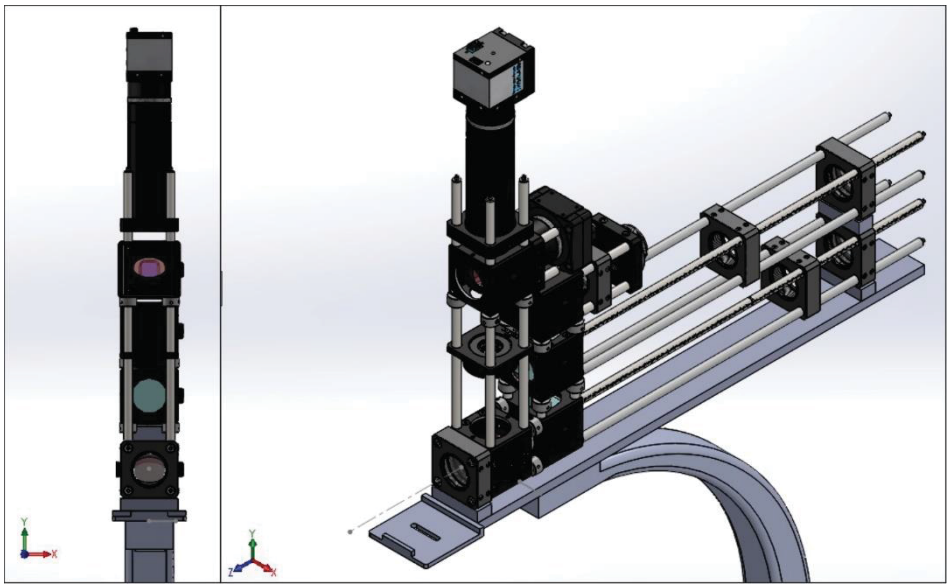

Figure 3.18: CAD model of the combination autorefractor, Badal optometer system with a front (left) and isometric view (right) shown. When viewed from the front, the system is symmetrical to allow for the mounting for components on either side of the measuring apparatus.

The base was designed to be symmetric with respect to the sagittal plane to allow the mounting of the trans-scleral spectral domain optical coherence tomography (SD-OCT) system on either side of the system to allow for temporal ciliary body imaging of both the left and right eye of a subject. A description of the trans-scleral SD-OCT system and how it is mounted to the other modules is described in Chapter 5.

The accommodation target delivery system (i.e. cellular phone) was mounted to an optical rail affixed to the rear of the system base. The rail allows for the position of the target to be adjusted to the focal length of the Badal system's collimating lenses.

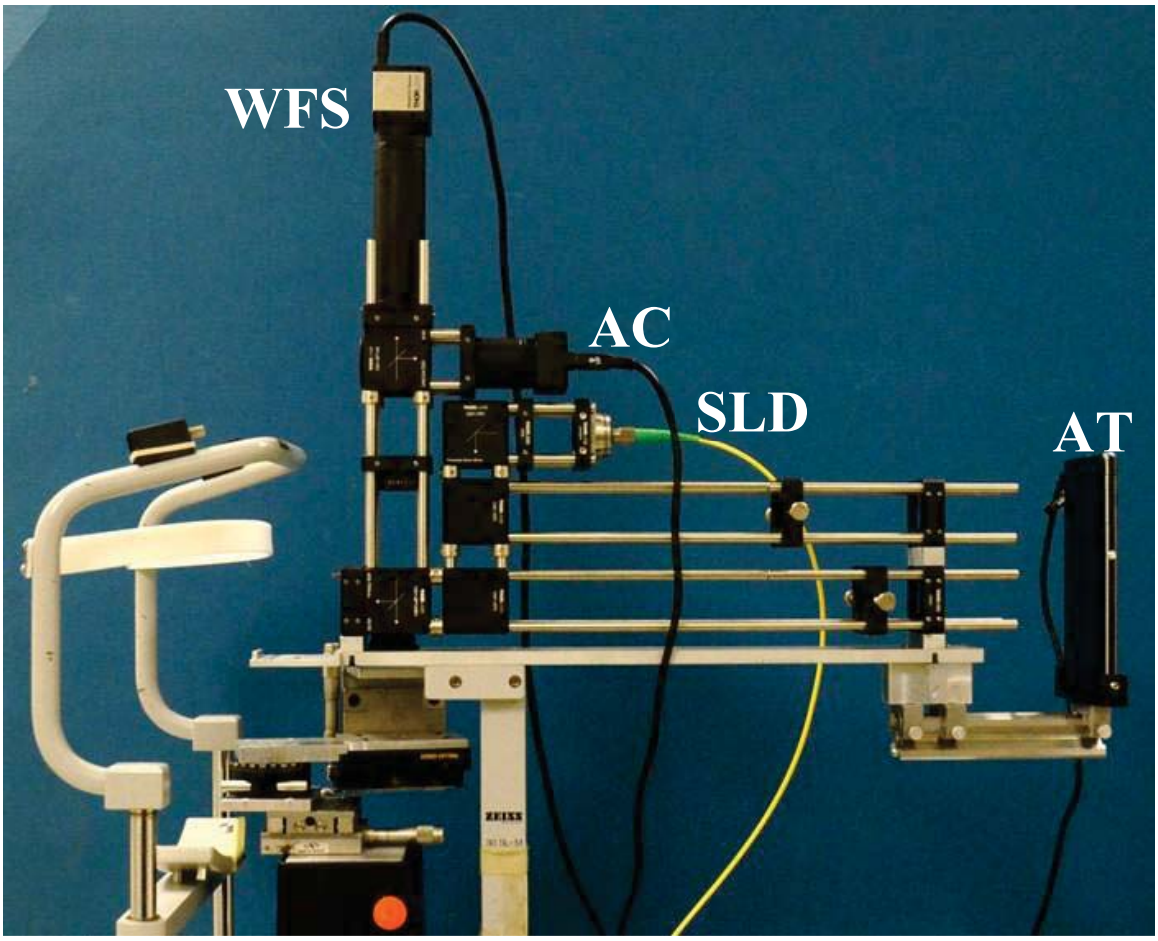

Figure 3.19: Profile view of the mounted combination autorefractor, dual-channel accommodation modules. WFS: Shack-Hartman wavefront sensor. AC: Alignment Camera. SLD: Superluminescent diode probe beam. AT: Accommodation Target.

A platform located in front of the objective lens (Figure 3.19) allows mounting of the anterior segment SD-OCT probe. The platform is recessed and slotted to allow for the probe to be seated with no axial translational freedom and lateral translational freedom with a fixation point located at the slot. This design will allow for adjustment of the probe for better alignment between all modules of the system.

3.4.9 Control Software

In order to interface the data output by the aberrometer and accommodation stimulus modules, a program was written in LabVIEW (National Instruments, Austin, TX) (Figure 3.20). The software needed to be capable of providing certain features:

- Input of identifying information of the subject for later review.
- A real-time plot of the wavefront sphere data output by the wavefront sensor.
- Real-time display of wavefront sphere, cylinder, and axis data.
- Display of the pupil image given by the pupil camera.
- Allow for the control of certain parameters: measurement pupil size, measurement pupil position, and number of included Zernike orders.
- Collection of all relevant data to a delimited text file, such as the ocular refraction parameters and the Zernike coefficients.

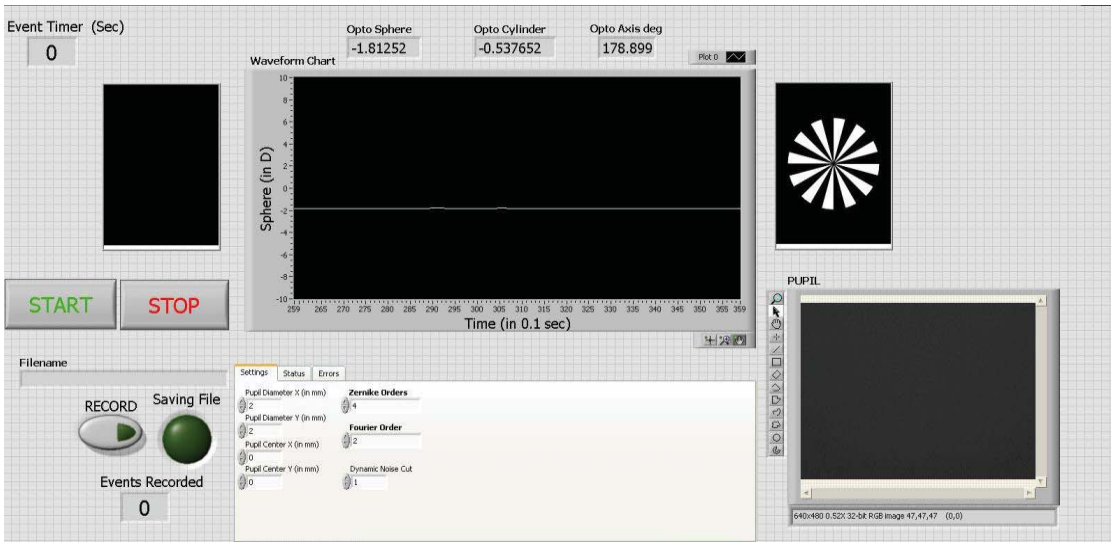

Figure 3.20: Graphical user interface of program used to record wavefront data and present the accommodation stimulus.

3.5 System Validation

The system validation was performed to ensure that the system designed meets the design specifications. The following experiments were performed as a means to comply with validation requirements:

- Light source safety testing
- Autorefractor module benchtop calibration
- Measurement stability experiment
- Real-time measurement of accommodation

3.5.1 Light Source Safety Test

The probe beam power output and irradiance were evaluated to ensure that they meet the safe exposure limits set forth by the ISO standard for ophthalmic instruments (ISO 15004-2, 2007). There are two group classifications that represent whether or not a light hazard exists. Group 1 instruments are ophthalmic instruments for which no potential light hazard exists and must be shown to meet the criteria set forth in Section 5.2 of the standard. They must also meet the limit requirements described in Section 5.4. Group 2 instruments are ophthalmic instruments for which a potential light hazard exists. They do not meet the requirements of Section 5.2, but operate within limits defined in Section 5.5. Section 5.2 states that for an instrument to be classified in Group 1, any or all of the follow criteria must apply:

a) An International Standard exists for the instrument type, but no light hazard requirements are included in that international standard.

b) Its components, e.g. lamps, light-emitting diodes, non-removable filters, lenses, fibers, etc., prevent emissions in excess of the limits specified for instruments in the Group 1 and certification exists.

c) Its only sources of radiation are Class 1 lasers as classified under IEC 60825-1:2001.

d) Its emission values are equal to or less than the limit values given in Section 5.4.

Table 3.3: Applicable Group 1 and Group 2 limit values for continuous wave instruments. Since the probe beam source operates at a wavelength of 750 nm, thermal irradiance is the only applicable requirement. d_r is the calculated retinal spot diameter.

	Parameter	Wavelength (nm)	Equation	Limit
Group 1	Retinal visible and infrared radiation thermal irradiance	380-1400	$E_{VIR-R} = \sum_{380}^{1400} E_\lambda R(\lambda)\Delta\lambda$	0.7 W/cm^2
Group 2	Retinal visible and infrared radiation thermal irradiance	380-1400	$E_{VIR-R} = \sum_{380}^{1400} E_\lambda R(\lambda)\Delta\lambda$	$(1.2/d_r)$ W/cm^2

Since the system operates in the near infrared spectrum (750 nm ±10 nm) (Figure 3.8), there is only one parameter set forth by Section 5.4 that is relevant to the system: Retinal visible and infrared radiation thermal hazard. Table 3.3 summarizes the limit of this requirement and its equation for both Group 1 and Group 2 classification.

The spectrum of the light source was verified using a spectrometer (Spectral Products SM-442) and normalized for use in the subsequent calculations (Figure 3.21). The standard states that the retinal visible and infrared radiation irradiance will be calculated by dividing the spectral radiant power in watts incident on the retina in a 0.03 mm circular disc centered on the position of highest irradiance by the area of the disc (7.07 x 10^{-6} cm^2). In order to do this calculation, we must first determine the spot size formed on the retina by the source. If we assume that the probe beam incident on the retina is collimated and the eye lies at the beam waist (d = 0.43 mm), the equation to determine retinal image size is:

$$1.27\frac{\lambda f}{d} \qquad [3.13]$$

Where λ = 750 nm, the central wavelength of the source, and f = 17 mm, representing a lens with a power of 60 D, which approximates the total power of the eye. Solving equation [3.17] using the aforementioned parameters yields a spot size of 0.038 mm.

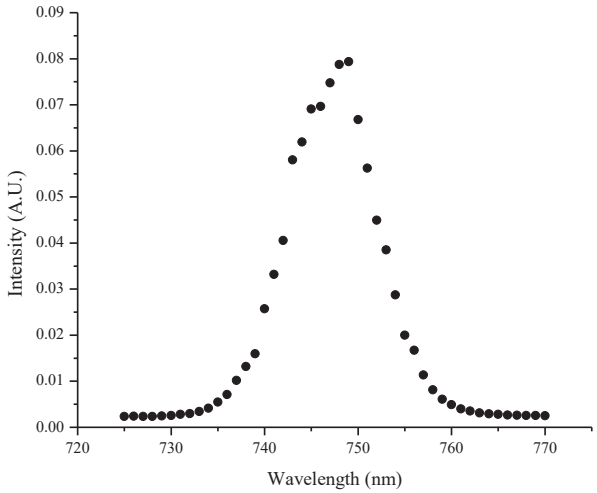

Figure 3.21: Normalized spectrum of the SLD source.

The retinal irradiance was recorded through a 7 mm pupil with the detector positioned at the intended corneal plane. The irradiance was measured with a Gigahertz-Optik optometer (5369M, Gigahertz-Optik, Türkenfeld, Germany) in combination with an RW-3703-4 (11219) 11 mm diameter detector capable of irradiance measurements for wavelengths between 400-1000 nm. The detected corneal irradiance was 3.67 W/m^2, or 0.367 mW/cm^2. The total power of the source was measured using a power meter (1930C) and detector (918-SL) (Newport, CA). The power reaching the eye was measured to be 190 μW. The weighting factor for the measured wavelength bandwidth ranges from 0.74 to 0.87.

In order to determine whether the probe beam satisfies the requirements, we assume a worst case scenario where the entire spectral irradiance is evenly distributed within the spot size of 0.038 mm with a weighing factor of 0.87. Dividing the output power by the

spot area and multiplying by the weight factor yields a value of 14.24 W/cm^2. The light source does not meet the limit to be in Group 1. The Group 2 limit required that the irradiance be less than $1.2/d_r$ W/cm^2 where d_r is the retinal spot diameter given in mm. Using the spot size above, to satisfy the Group 2 limit the irradiance must be less than or equal to 31.58 W/cm^2. As the irradiance detected on the retina is less than the limit, this means the SLD probe beam falls within Group 2 classification and therefore meets the safety criteria.

3.5.2 Autorefractor Calibration

3.5.2.1 Purpose

A benchtop optical experiment was conducted to ensure the autorefractor module is providing accurate measurements with a linear response within the desired dynamic range.

3.5.2.2 Methods

The autorefractor module was calibrated using a model eye designed and built in the lab (Figure 3.22). The model eye consists of a 30 mm focal length achromatic doublet positioned in front of a diffuse reflective surface. The diffuse surface is mounted to a translation stage to allow for axial displacement, mimicking the refractive error of the eye. When the distance between the lens and the diffuse reflector is larger than the effective focal length of the lens, the model eye is myopic. When the distance is shorter than the focal length, the eye is hyperopic.

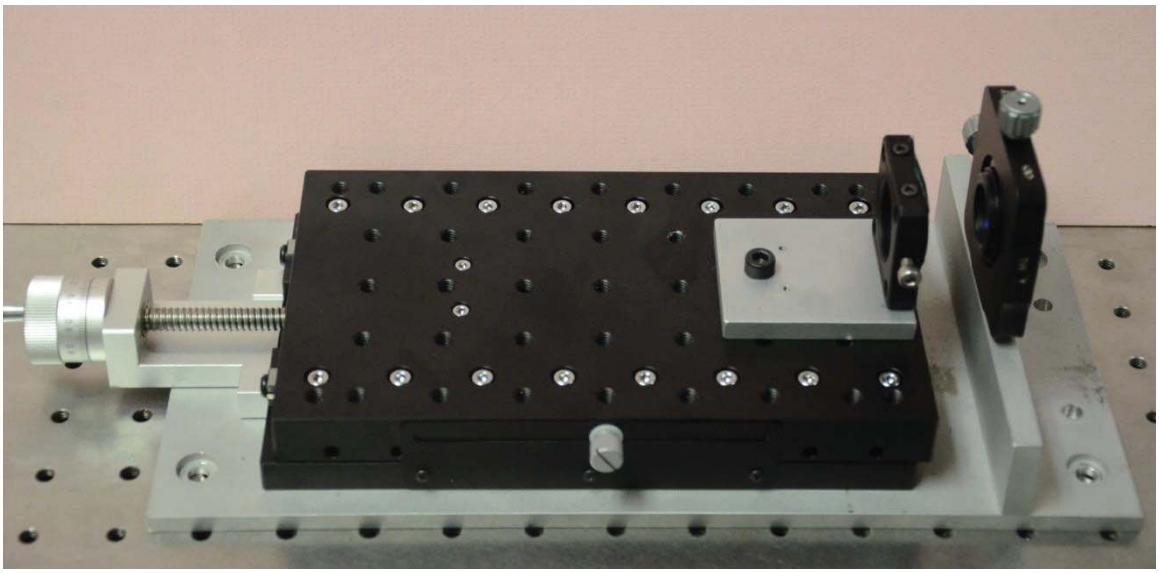

Figure 3.22: Model eye used for calibration of the autorefractor.

The model eye was mounted to the optical bench and the autorefractor positioned in front of the eye, with the objective set 100 mm away from the model eye lens. The translation stage was adjusted in 0.5 mm steps and the wavefront sphere, cylinder, axis, and radius of curvature were recorded.

3.5.2.3 Results

Figure 3.23 shows the results of the calibration. From the results recorded, the approximate measurement range is from -8.2 to +18.5 D in sphere. As desired, the autorefractor provides a linear measurement response throughout the measurement range ($y = 1.0528x + 0.2893$). Figure 2.24 shows a plot of the residuals between the measured data and the linear regression (Left) and a mean-difference plot of the measured values (Right). The measured values are within ±1.8 D of the regression values over the entire range of refractive error and within ±0.6 D of the regression values over the range of -8.2 D to +10 D. This covers the maximum hyperopia range of interest. The Bland-Altman plot shows that the mean difference between the theoretical model eye refraction and the measured refraction in the range of interest falls within 2 standard deviations. The

maximum range of the measurement system may be greater than the given values, as there exists a limitation in how much translation can be applied to the model eye. In the positive (i.e. hyperopic) modeling range, there is a physical limit to how close the diffuse reflective surface can get to the lens mount. In the negative (i.e. myopic) modeling range, as the diffuse reflective surface moves further away from the lens, the spot field intensity decreases and the detected spot field experiences a marked decreased in spot contrast. In order to fully characterize the behavior of the wavefront measurement module, a more robust model eye will need to be developed.

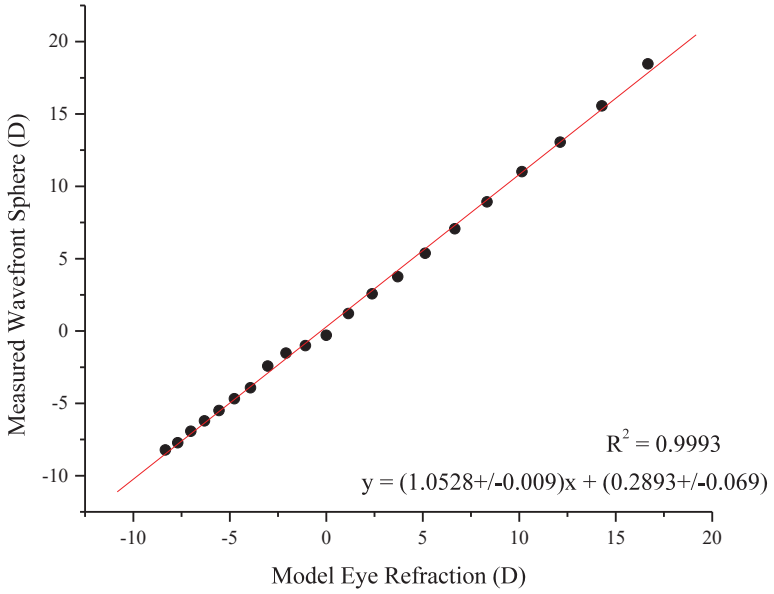

Figure 3.23: Measured wavefront sphere vs. the model eye refraction.

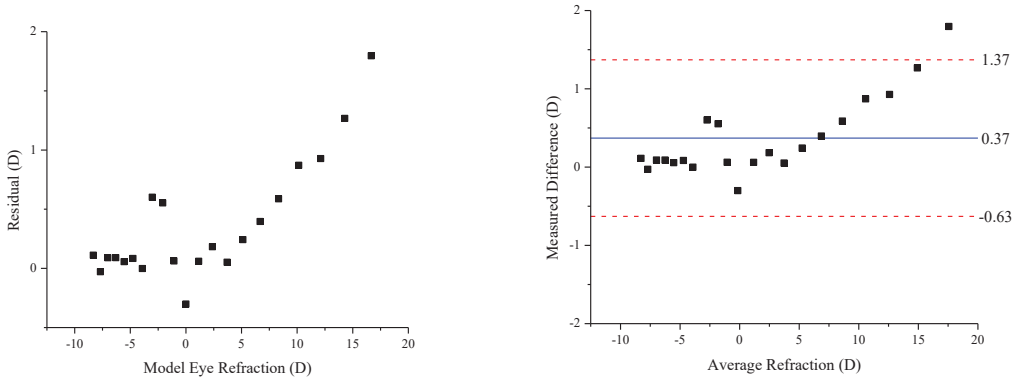

Figure 3.24: (Left) Residuals plot of the linear regression shown in Figure 3.23. Measured values are within ±1.8 D of the regression. (Right) Bland-Altman plot of the model eye refraction measurements.

3.5.3 Preliminary Studies

3.5.3.1 Purpose

To verify the stability of measurement using the autorefractor module of the system, as a proof of principle of dynamic real-time measurements, measurements were taken on the left eye of 3 subjects 3 times over a time span of 10 seconds.

3.5.3.2 Methods

The subjects were enrolled in a study approved by the University of Miami's Institutional Review Board. All measurements were done with the subjects in an uncorrected, non-cyclopleged state. Subjects were positioned in front of the system via a chin rest, with no stimulus target presented through the objective lens. They were then asked to fixate at distance with the contralateral eye. In between measurements, the subject was told to move away from the system, take a moment to rest their eyes, and place their head back in front of the system so that repositioning error could also be evaluated. In the LabVIEW control software, the acquisition period was set to 10 seconds. The sampling pupil is fixed to a 3 mm diameter and its position is fixed to the center of the sensor area.

Once the patient is in position, the operator presses the "Record" button to begin collecting wavefront data into an Excel spreadsheet. The rate of acquisition is 5 Hz. Measurements of optometric sphere, cylinder, and axis (terms defined by Thorlabs system documentation to represent the sphere, cylinder, and axis components of refraction) along with Zernike coefficients through the fourth order are collected at each time point. Sphere, cylinder, and axis measurements were averaged and compared to values obtained by a commercial autorefractor.

3.5.3.3 Results

Figures 3.25, 26, and 27 show the repeatability measurement results of sphere, cylinder, and axis for each subject. Table 3.4 summarizes the measured results.

Table 3.4: Repeatability experiment results for 3 subjects.

	Sphere (D)	Cylinder (D)	Axis (deg.)		Sphere Avg. (D)	Sphere Std. (D)	Cylinder Avg. (D)	Cylinder Std. (D)	Axis Avg. (deg.)	Axis Std. (deg.)
				Run 1	0.29	0.88	-1.95	1.48	111	34.39
24 y/o	1.08	0.25	76	Run 2	2.25	0.74	-1.44	1.08	100	39.80
				Run 3	2.22	0.22	-0.98	0.25	143	11.96
				Run 1	-3.03	0.37	-0.77	0.18	72	6.13
27 y/o	-2.54	0.71	15	Run 2	-2.67	0.20	-1.65	0.17	77	2.63
				Run 3	-3.45	0.26	-0.75	0.28	53	15.42
				Run 1	-2.28	0.35	-1.9	0.77	109	13.51
33 y/o	-1	0.25	5	Run 2	-1.01	0.25	-1.32	0.57	100	23.78
				Run 3	-1.06	0.17	-1.82	0.22	99	2.04

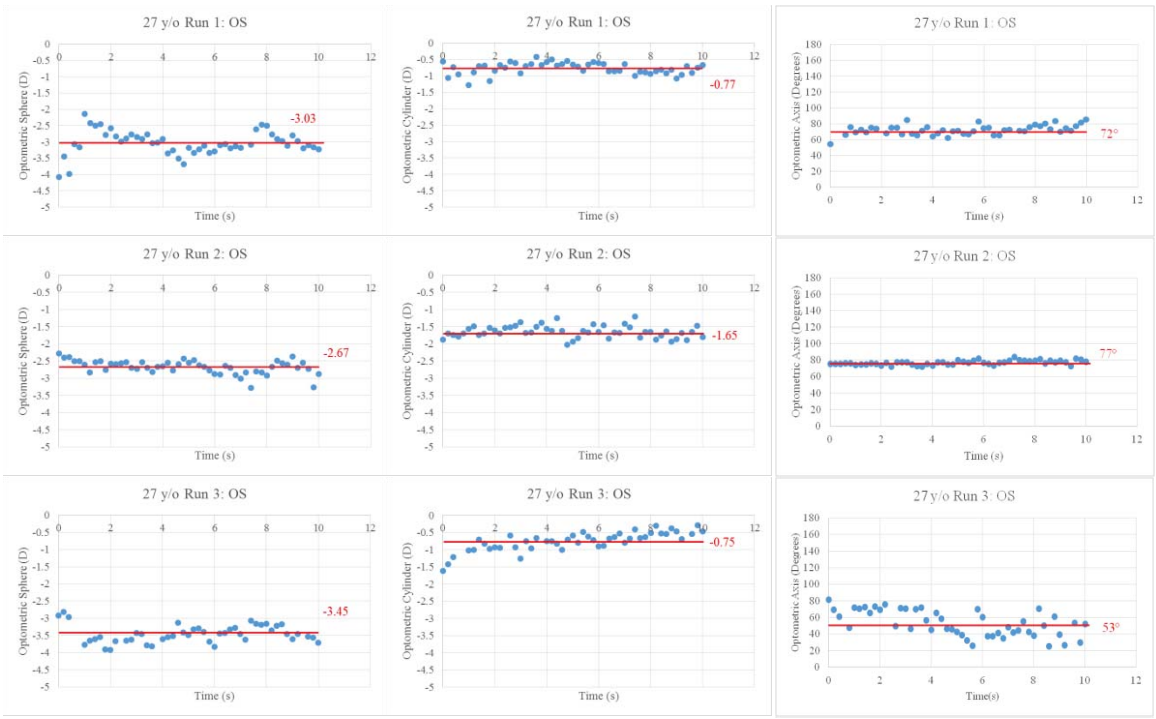

Figure 3.25: Stability experimental results for 27 year old subject, left eye. SEQ: -2.19 D.

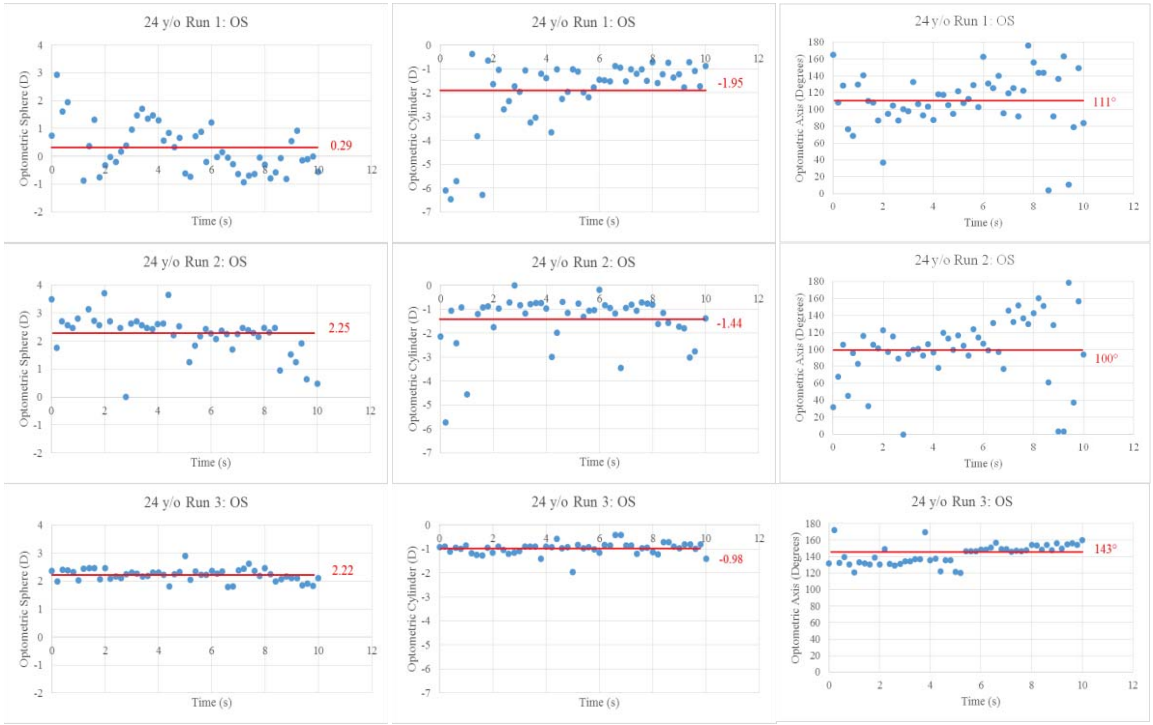

Figure 3.26: Stability experimental results for 24 year old subject, left eye. SEQ: 1.20 D.

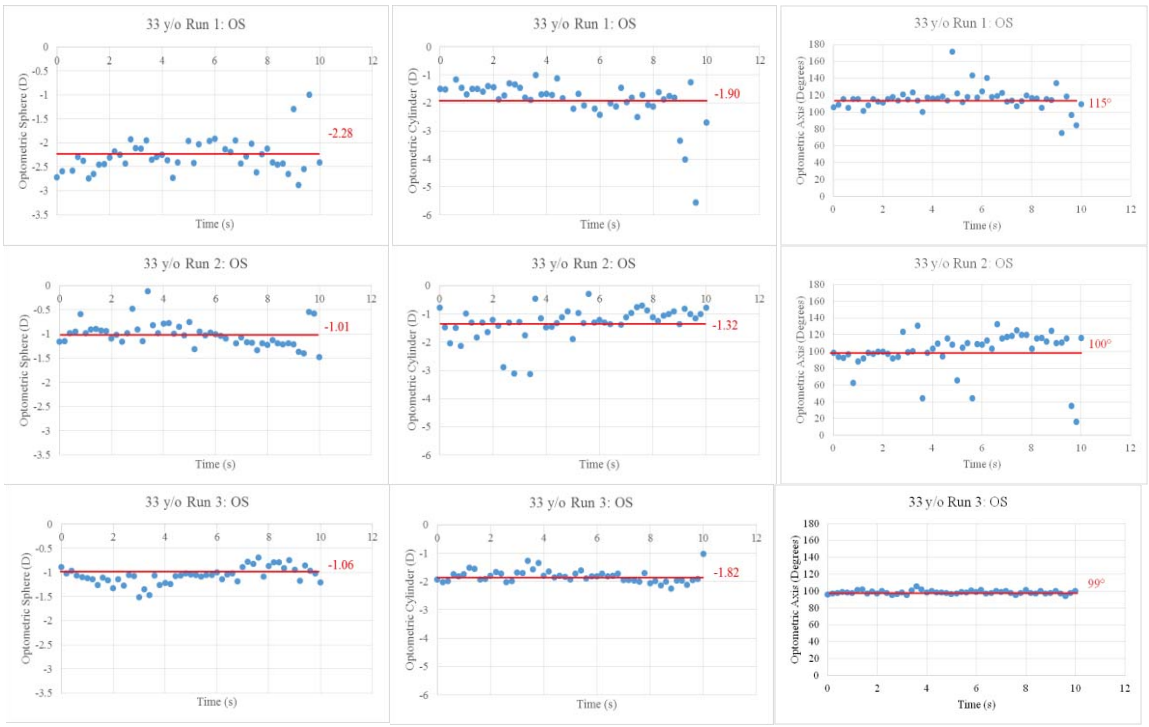

Figure 3.27: Stability experimental results for 33 year old subject, left eye. SEQ: -1.125 D.

The measurements show that the average measured spherical equivalent refraction for the 24, 27, and 33 year old subject was 0.86 D, -3.58 D, and -2.29 D, respectively. These values are within ±1.4 D of the values obtained with the commercially available autorefractor. Standard deviation of the measured sphere and cylinder value were within 0.90 D and 1.50 D respectively, for all measurements. The value of cylinder was less predictable. This is most likely due to issues with alignment of the subject during voluntary fixation onto the target.

3.5.3.4 Discussion

The data collected in the stability experiments represents the basic proof of principle of the continuous measurement of the ocular wavefront. There is some error in the measurements in comparison to the objective refraction with a commercial autorefractor, but the measurement difference is within the difference that can be expected

given that the measurements were not done under cycloplegia and the subjects may have accommodated. Some of the difference may also be due to the differences in measurement methodology and in the calculation of refraction from the Zernike coefficients (Jainta et al, 2004; Teel et al, 2014; Wang et al, 2003).

The continuous data retrieved from the autorefractor is not filtered prior to recording. The data shown in Figures 3.26, 3.27, and 3.28 represent raw sphere, cylinder, and axis data. Erroneous data points resulting from ocular movements is kept in the calculations. Since the subject was asked only to fixate on a distant point with the contralateral eye, proper centration of the measured eye is not controlled. Since the sampled pupil is fixed in size and position, eccentric positioning of the patients eye may drive variability in the measurement. If during the recording process, a low-pass filter were to be applied to the sampled data, the expected standard deviation of measurement would be lower.

The standard deviation of measurement of sphere was lower than that of cylinder and axis. The aforementioned ocular eccentricity may play a role in the measured cylinder values. It was also observed that increased variation in the measurement of cylinder resulted in an increase in the variation of the axis measurements. Furthermore, a lower measured cylinder value (i.e. cylinder less than 0.5 D) results in a higher inherent uncertainty of the axis measurement, in part because of higher uncertainty in determination of the angle of the steepest meridian when the contribution of cylinder to the wavefront is low.

Instrument myopia (Hennessy, 1975), or the disposition of a subject to inappropriately accommodate when looking through an optical system, may account for

the systemic trend of the measured spherical equivalent refraction to be lower. Subject refraction appears to be more myopic that the value measured with the autorefractometer. This difference could be due to the lack of a fogging to ensure a fully relaxed accommodative state. Overall, measured refraction was within 1.5 D of that measured by the commercially available autorefractor. No test method validation was performed, so it is unknown how well these values correlate to manifest refraction values.

3.5.4 Measurement of Accommodative Response

3.5.4.1 Purpose

To validate the capability of the autorefractor to measure the accommodative response.

3.5.4.2 Methods

Measurements were taken on the left eye of 3 subjects over a stimulus range of 0 D to 6 D. All measurements were done with the subjects in an uncorrected, non-cyclopleged state. Subjects were asked to fixate on the far channel stimulus and occlude the contralateral eye with their hand. The auxiliary lens of the far target was adjusted according to knowledge of their spherical equivalent refraction and until the subject stated that the target was in focus, placing the far target channel stimulus at their far point.

The wavefront sensor software was then run to collect the measurements. Unlike the stability experiments, the duration of measurement was 6 seconds, with application of the stimulus occurring 2 seconds after acquisition had begun. The wavefront sensor sampled pupil diameter was fixed to 3 mm. The procedure was repeated three times, once for each of the following stimuli; 0 to -2 D, 0 to -4 D, and 0 to -6 D. In between measurements while the stimulus auxiliary lens position was being adjusted, the subject

was allowed to sit back away from the instrument. Measurements were retaken if the pupil shifted out of the range of the probe beam. Once the examination ended, the subjects were asked to provide feedback on the presentation of the stimulus and the ease with which they were able to comply with the instructions of the study. The data was entered into a spreadsheet and the average of the steady state response was calculated and plotted along with the refraction data over time. Steady state changes in cylinder and axis were calculated using simple subtraction. They do not correspond to actual sphero-cylindrical power change.

3.5.4.3 Results

The purpose of this experiment was to demonstrate the basic feasibility of acquiring dynamic traces of the changes in the ocular wavefront during stimulated accommodation. Figures 3.28, 29, and 30 show the measurements of sphere and cylinder in response to an accommodative stimulus for each subject. Steady state values before and after the application of the accommodative stimulus were averaged and these values are displayed on the graphs. Absolute change in defocus and cylinder with respect to the accommodative stimulus is displayed at the bottom left of the respective graphs. All subjects report being able to view the target before and after the change in the stimulus.

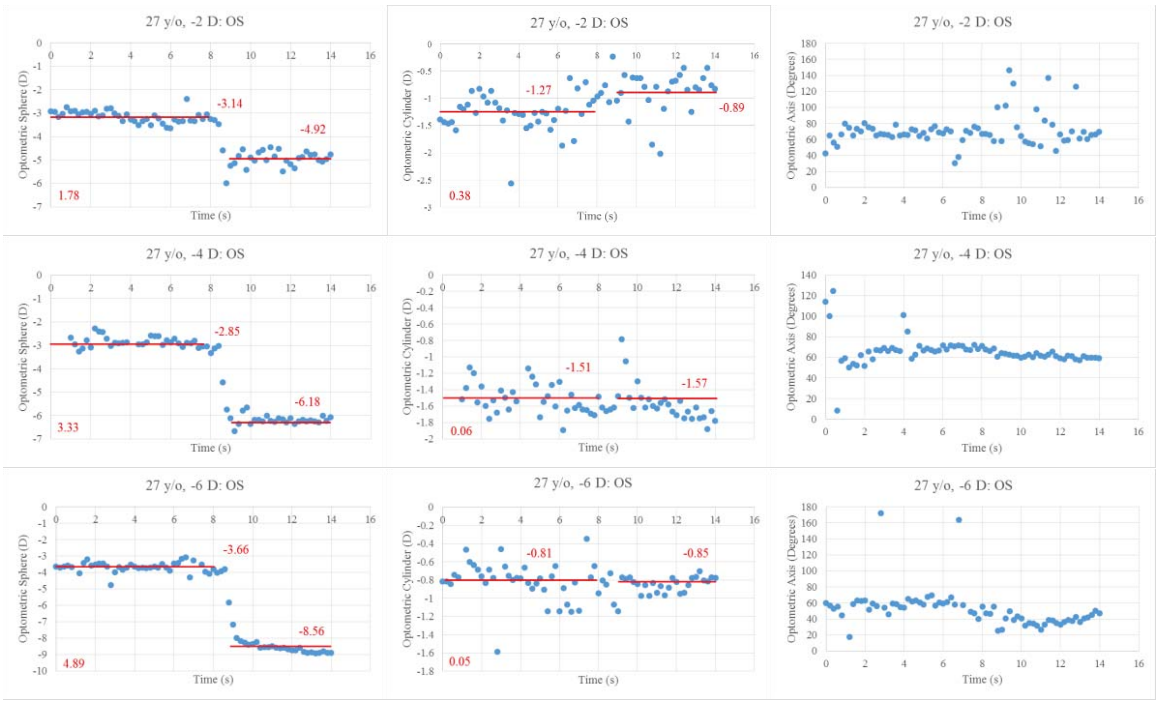

Figure 3.28: Accommodative change in measured sphere, cylinder, and axis of a 27 year old subject at -2 D, -4 D, and -6 D stimulus.

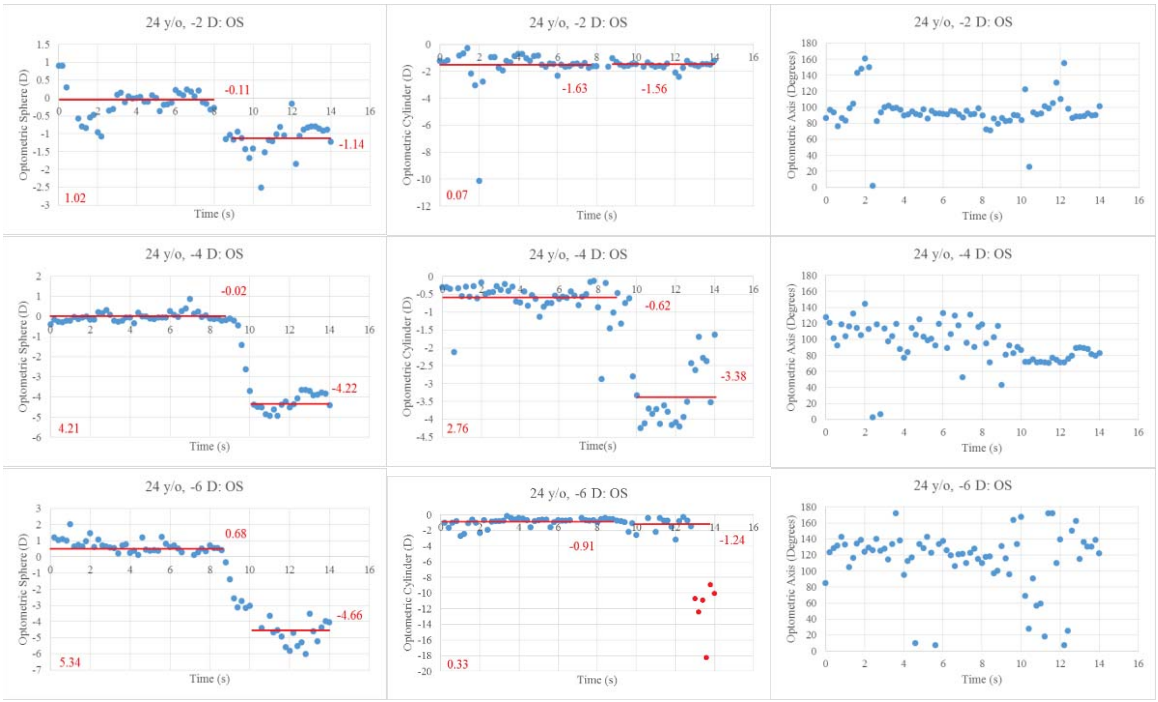

Figure 3.29: Accommodative change in measured sphere, cylinder, and axis of a 24 year old subject at -2 D, -4 D, and -6 D stimulus. The measurement points shown in red were removed from the calculations. These values at the end of the acquisition period are clearly incorrect.

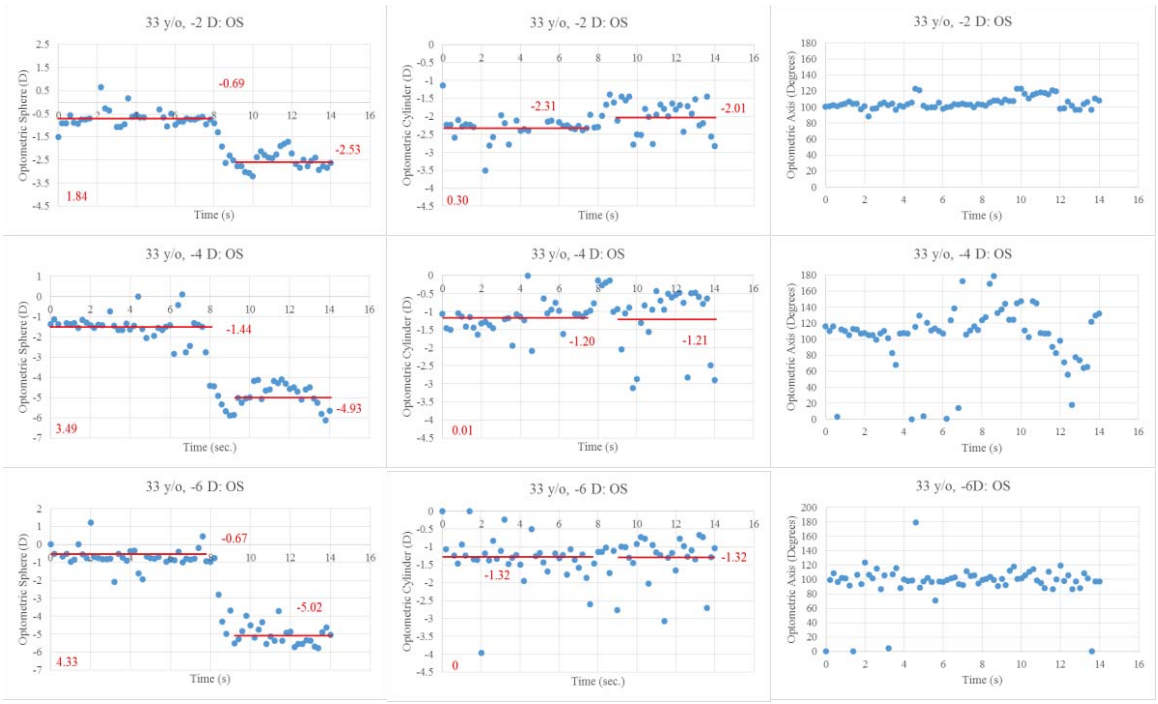

Figure 3.30: Accommodative change in measured sphered, cylinder, and axis of a 33 year old subject at -2 D, -4 D, and -6 D stimulus.

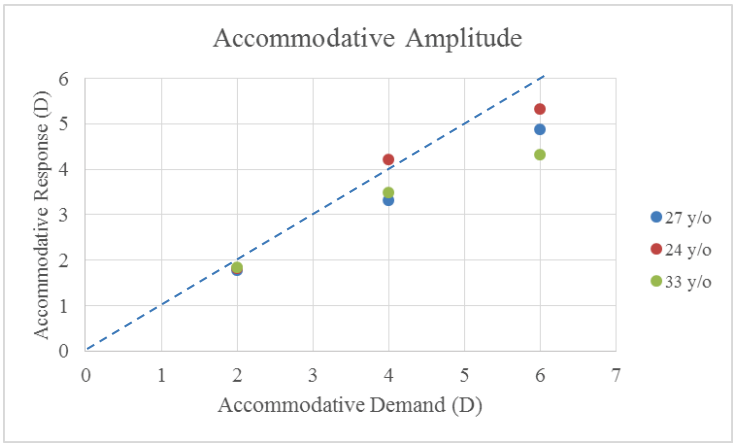

Figure 3.31: Plot of accommodative response versus accommodative demand. Amplitude of accommodation was calculated from the steady state averages of the optometric sphere measurements.

3.6 Discussion

The results obtained show agreement to results from studies by Lin and Jiang (2013) and Gambra et al (2009) in terms of the amount of accommodative lag exhibited by each subject. Figure 3.31 shows the accommodative response versus accommodative demand. On average, as the accommodative demand is increased, the accommodative

response decreases (i.e. increased accommodative lag). Again, as with the stability experiments, raw data collected during each run is displayed and used in calculation of the steady state averages. This explains why, under certain measurement conditions, the measured cylinder at the steady state time points strays drastically (greater than 1 D) from a difference of zero. For all three subjects, the accommodative response was within 1.7 D of the applied stimulus.

There are a few limitations to the present technique. The visible wavefront sensor probe beam interferes with measurement. Subjects complained the beam interfered with their ability to bring the target into focus, especially in the -6 D stimulus trial. This difficulty to focus on the target at greater stimulus values can be seen in the increased time to stabilization of the accommodated steady state portion of the data plots above. To compensate for this distracting effect of the probe beam, the beam was aligned within the system to lie approximately 1 mm laterally eccentric to the center of the accommodation stimulus. It was found that the probe beam still interferes with target fixation even at the position, as noted by each subject. This may add to the effect of ocular misalignment on measured wavefront values, and there appears to be an increase in measurement error as the accommodative demand is increased. As mentioned for the stability experiments, the addition of filtering to the acquired values may improve outcomes.

The target stimulus presented is not fogged. Using knowledge of the subject's spherical equivalent refraction and their verbal confirmation, the target is placed at the far point. This subjective method of adjusting the far target (and the near relative to the far position) may be affected by instrument myopia. As demonstrated by many of the initial

steady state conditions, the subject may be prematurely accommodating, leading to a decreased measured difference between the accommodated and unaccommodated states.

The following modifications to the autorefractor and accommodation stimulus modules would improve functionality of the overall combined system:

- Extension of the probe beam wavelength: By shifting the probe beam wavelength outside of the visible range (i.e. >900 nm), the probe beam will cease to interfere with the subjects' ability to view the target and may improve accommodative response.
- Increase in the wavefront sampling frequency of the wavefront sensor: If we wanted to determine the time constant associated with the accommodative response to a step stimulus, more data points must be collected during the transient period. Increased sampling will also ensure that enough data is collected, even if filtered.
- Automatic artifact registration and filtering of recorded data: In order to improve measured averages and the standard deviation of measurement during accommodation, the filtering of erroneous data points created due to eye blinks and minute ocular movements should be implemented.

3.7 Conclusion

A Shack-Hartmann based autorefractor combined with a target was designed. Calibration shows a linear response within -8 D to +10 D. Preliminary studies on 3 human subjects demonstrate that the autorefractor module and accommodation stimulus were shown to be capable of eliciting and measuring an accommodative response in real-time. The values obtained for steady state refraction are in agreement with those obtained with a

commercial autorefractor (standard deviation of sphere measurement within 1 D). In the following chapter, a method for determining lens power using an extended depth OCT system will be described. This method, in combination with the integrated OCT, autorefractor, and accommodation stimulus system will be capable of providing biometric information of the accommodative response.

Chapter 4: Calculation of Crystalline Lens Power using Extended-depth Optical Coherence Tomography (Aim 2)

The previous chapter described the development of a wavefront sensor-based autorefractor that will be used to measure changes in refraction dynamically during accommodation. The autorefractor will be combined with an OCT biometry system to allow simultaneous measurements of changes in lens shape and refraction during accommodation (Chapter 5). One of the applications of the system will be to determine the relation between changes in crystalline lens shape and power. These studies will require a method to quantify lens power.

This chapter presents a method for measuring lens power from whole eye OCT biometry, corneal topography, and refraction using a modified version of the Bennett method. A reduced eye model was used to derive a formula for lens power in terms of ocular distances, corneal power, and objective spherical equivalent refraction. The formula was used to calculate lens power in 16 eyes of 8 human subjects. Mean lens power measured was 24.2 D +/-1.8 D. An error analysis shows that the method produces lens power values with a predicted uncertainty of ±0.5 D. This method for lens power calculation will be used in Chapter 5 to correlate lens thickness change measured with the extended-depth SD-OCT to accommodative power changes measured with the autorefractor. The work described in this chapter has been published as a journal article in Biomedical Optics Express (Hernandez et al, Biomedical Optics Express 6(11):4501-4515; 2015).

4.1 Measurement of Lens Power

The crystalline lens is a dynamic focusing element that accounts for approximately one third of the dioptric power of the relaxed eye. Together with corneal power and ocular

distances, crystalline lens power is one of the parameters that determine the refractive state of the eye. Even though the lens is believed to not play an active role in ametropia, its significant contribution to the refractive state of the eye has prompted a great amount of interest to measure lens power and its age-dependence, and to determine how changes in lens power correlate with changes in ocular dimensions in the development of the refractive state of the eye (Mutti et al, 1995; Mutti et al, 2005; Iribarren et al, 2012; Iribarren, 2015; Olsen et al, 2007; Jones et al, 2005). Lens power is also essential to the study of accommodation, since changes in lens shape produce a change in lens power which allows the eye to change focus from far to near during accommodation.

Lens power can be calculated from measurements of lens thickness and radii of curvature. Values of the lens radii of curvature can be derived from images of the Purkinje reflexes (phakometry) (von Helmholtz, 1855; Mutti et al, 1992; Rosales & Marcos, 2006), or from cross-sectional or three-dimensional images of the lens acquired using Scheimpflug imaging (Dubbelman et al, 2001; Koretz et al, 1997), or OCT (Dunne et al, 2007; Gambra et al, 2013; Ortiz et al, 2013). Scheimpflug and OCT images must be corrected for distortions caused by refraction of light at the corneal and lens surfaces. The lens power calculations are generally performed with an assumed value for the equivalent refractive index (Garner, 1997; Dubbelman & van der Heijde, 2001), a value shown to change with age (Charman & Atchison, 2013). The accuracy of the posterior radius and of the lens power calculated is therefore limited by uncertainty in the value of the equivalent refractive index. In addition, the calculated lens power is highly sensitive to errors in the values of the refractive index. For instance, for a lens with an anterior radius of 10 mm and posterior radius of -6 mm, an uncertainty of only ±0.01 in refractive index produces an

uncertainty of ±2.7 D in lens power. Alternatively, for a precision of ±0.5 D in lens power calculation, one would need to know the equivalent index with a precision of ±0.002 (Ho et al, 2001). In the study of Dubbelman and Van der Heijde (2001), the variability of the equivalent refractive index obtained experimentally among individuals of the same age is on the order of ±0.005. This suggests that the uncertainty in the refractive index alone introduces an uncertainty on the order of ±1.3 D in the lens power calculated from measurements of curvature.

Another approach to calculate the lens power is the method developed by Bennett (1988), which eliminates the need for measurements of lens curvatures. The Bennett method requires measurement of corneal power, anterior chamber depth, lens thickness, axial eye length, and the subject's refraction. A paraxial model of the eye constructed from the measured biometric parameters is used to calculate lens power. The calculation relies on an estimate of the position of the principal planes of the lens. Lens power is calculated by assuming that the ratio of anterior to posterior lens radius is fixed, equal the value used in the Emsley-Gullstrand model. With this assumption, the position of the lens principal planes relative to the lens vertices depends only on the lens thickness. Error analyses show that the Bennett method provides a measurement of lens power with an accuracy that is on the order of ±1 D, better than the accuracy provided by phakometry (Dunne et al, 1989; Royston et al, 1989; Rozema et al, 2011).

Rozema et al (2011) published a detailed study comparing the lens power obtained with the Bennett method with values obtained from phakometry and using modified simplified versions of the Bennett method. The simplified methods assume that the crystalline lens is a thin lens placed either at the anterior vertex of the lens (the Stenström

method), or at the mid-point between the two principal planes of the lens (the Bennett-Rabbetts method). Rozema, Atchison, and Tassignon improved on these methods by finding the position of the thin lens that matches the calculated lens power to the lens power obtained using phakometry for a set of emmetropic eyes. However, the prediction error in lens power was found to increase significantly when the method was applied to a dataset that includes myopic eyes. The prediction error was also found to be strongly correlated with axial eye length. These analyses suggest that the optimal position of the thin equivalent lens varies with the refractive state of the eye.

The extended-depth optical coherence tomography system described in Chapter 5 was used to measure the ocular distances along the entire length of the eye. The system provides measurements of the corneal thickness, anterior chamber depth, lens thickness and vitreous depth. The system's measurements of ocular biometry, combined with measurements of corneal topography and refraction from commercially available devices, were used in the calculation of lens power using an optimized version of the Bennett method. In the optimized method, the thick lens model used in the Bennett method is replaced with a thin lens approximation. The calculations demonstrate that there is a position of the thin lens that eliminates the prediction error in lens power. The position of the thin equivalent lens depends on the ratio of anterior to posterior curvature and on the conjugate ratio of the lens (ratio of image to object distance for the lens).

4.2 Lens Power Calculation from Biometry

4.2.1 Equivalent Thin Lens Position

Table 4.1 defines all variables used in the subsequent equations for the given schematic of the eye (Figure 4.1). The known ocular parameters are: the radii of curvature

of the anterior and posterior cornea, the anterior chamber depth, the lens thickness, the vitreous depth, and the refractive error of the eye. Similar to the Bennett method, the lens power is obtained by applying the conjugation formulae to the lens:

$$L_0 = \frac{n}{s'_L} - \frac{n}{s_L} \qquad [4.1]$$

Table 4.1: List of variables (in alphabetical order).

ACD:	Anterior chamber depth: Distance from posterior corneal vertex to anterior lens vertex
b:	Coefficient of the calculation of lens power
CCT:	Central corneal thickness
H_1, H_3, H_4:	Corneal object principal point, Lens object principal point, Lens image principal point
K, K_1, K_2:	Total corneal power, Anterior corneal surface power, Posterior corneal surface power
ΔL:	Prediction error in lens power: $\Delta L = L - L_0$
L_0, L:	Total lens power - Actual, Total lens power - Estimated
L_3, L_4:	Anterior lens surface power, Posterior lens surface power
LT:	Central lens thickness
M_L	Lens magnification, $M_L = s'_L/s_L$
n, n_K, n_L:	Refractive indices: aqueous and vitreous, cornea, lens equivalent refractive index
O:	Lens center for the thin lens model of the lens
R:	Refraction in the anterior corneal plane
R_1, R_2, R_3, R_4:	Radius of curvature: Anterior cornea, Posterior cornea, Anterior lens, Posterior lens
SEQ:	Spherical Equivalent Refraction
s_K:	Distance from retinal conjugate to object principal point of cornea
s'_K:	Distance from image principal point of cornea to primary image
s_L:	Distance from object principal point of lens to primary image
s'_L:	Distance from image principal point of lens to retina
V_1, V_3, V_4:	Vertex: Anterior cornea, Anterior lens, Posterior lens
VD:	Distance from posterior lens vertex to retina
v_L:	Distance from lens anterior vertex to primary image
v'_L:	Distance from lens posterior vertex to retina

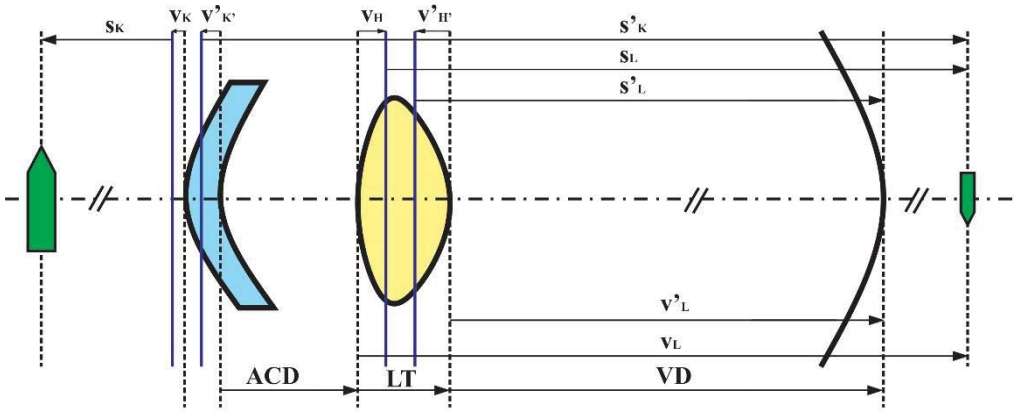

Figure 4.1: Schematic representing the primary image formed by the cornea, which is subsequently imaged by the crystalline lens onto the retinal plane. Variable definitions can be found in Table 4.1. The figure shows the case of a myopic eye (the retinal conjugate is located at a finite distance in front of the eye). Solid vertical lines correspond to principal planes. Dashed vertical lines show the planes passing through the object, image and surface vertices.

In the crystalline lens, the distance between the principal planes is small ($\overline{H_3H_4}$<0.2 mm, calculated using the age-dependent data of Dubbelman et al, 2001) for a normal range of lens shapes and refractive indices. To simplify the expressions, the lens can be approximated as a thin lens, with lens center O. Bennett and Rabbetts modeled the lens as a thin lens with lens center located at the mid-point between the two principal planes of the lens (Bennett & Rabbetts, 1998; Rozema et al, 2012). Instead of using the midpoint, there is an optimal position of the lens center that minimizes the error in the lens power calculation. This position depends on the conjugation ratio (ratio of image to object distance, s'_L/s_L).

The assumption that the lens is a thin lens with center O introduces a small error in the object and image distances, s_L and s'_L, equal to the distances from the lens principal points to the lens center. The resulting estimated power is:

$$L = \frac{n}{s'_L - \overline{H_4O}} - \frac{n}{s_L - \overline{H_3O}} \qquad [4.2]$$

Since the distances $\overline{H_4O}$ and $\overline{H_3O}$ are much smaller than the distances s'_L and s_L, the fractions can be replaced with their first order Taylor series approximation:

$$L = n\left[\frac{1}{s'_L}\left(1+\frac{\overline{H_4O}}{s'_L}\right)-\frac{1}{s_L}\left(1+\frac{\overline{H_3O}}{s_L}\right)\right] \quad [4.3]$$

Combining equations [4.1] and [4.3] gives:

$$L = L_0 - n\left(\frac{\overline{H_4O}}{s'^2_L}+\frac{\overline{H_3O}}{s^2_L}\right) \quad [4.4]$$

Using equation [4.4], and the relation $\overline{H_4O} = \overline{H_4H_3} + \overline{H_3O}$, shows that the prediction error in lens power, $\Delta L = L - L_0$, produced by approximating the crystalline lens as a thin lens located at a position O is:

$$\Delta L = L - L_0 = -n\left(\frac{\overline{H_3H_4}-\overline{H_3O}}{s'^2_L}+\frac{\overline{H_3O}}{s^2_L}\right) \quad [4.5]$$

From equation [4.5], there is a position of the lens center, O, for which the prediction error is equal to zero:

$$\overline{H_3O} = \frac{\overline{H_3H_4}}{1-\frac{s'^2_L}{s^2_L}} \quad [4.6]$$

Since the ratio s'_L/s_L is the magnification M_L of the lens, we can write equation [4.6] as:

$$\overline{H_3O} = \frac{\overline{H_3H_4}}{1-M^2_L} \quad [4.7]$$

The position of the lens center can be expressed in terms of the anterior vertex, V_3, of the lens, using the formulas for the distance from vertices to principal planes in a thick lens:

$$\overline{V_3H_3} = \frac{n}{n_L}LT\frac{L_4}{L_0} \quad [4.8a]$$

$$\overline{V_4H_4} = -\frac{n}{n_L}LT\frac{L_3}{L_0} \quad [4.8b]$$

Combining equations [4.7] and [4.8a, b] gives:

$$\overline{V_3O} = \frac{LT}{1-M_L^2}\left(1 - \frac{n}{n_L}\frac{L_3+L_4M_L^2}{L_0}\right) \quad [4.9]$$

The equation shows that the distance from the vertex to the lens center is proportional to the lens thickness, in first approximation if the contribution of the thickness term is ignored in the expression of the lens power (i.e. the approximation $L_0 = L_3 + L_4$). A calculation for typical values of the lens shape shows that the shift in position of the lens center is less than 0.1 mm when the thickness term is ignored, which is considered negligible. Neglecting the thickness term in the expression of lens power, L, equation [4.9] can be written in the following form:

$$\overline{V_3O} = b \times LT \quad [4.10]$$

Where the coefficient b is equal to:

$$b = \frac{1}{1-M_L^2}\left(1 - \frac{n}{n_L}\frac{L_3+L_4M_L^2}{L_3+L_4}\right) \quad [4.11]$$

Or, in terms of the radii of curvature (where $R_4 < 0$):

$$b = \frac{1}{1-M_L^2}\left(1 - \frac{n}{n_L}\frac{M_L^2-\frac{R_4}{R_3}}{1-\frac{R_4}{R_3}}\right) \quad [4.12]$$

Equations [4.10] and [4.12] show that the distance from the anterior lens vertex to the optimal thin lens position is proportional to the lens thickness, with a proportionality constant that depends on the conjugation ratio of the lens and on the ratio of posterior to anterior lens radius.

4.2.2 Estimated Lens Power

The object and image distances in equation [4.2] can be expressed in terms of the vertices (see Figure 4.1):

$$s_L' = v_L' + \overline{H_4V_4} \quad [4.13a]$$

$$s_L = v_L + \overline{H_3V_3} \qquad [4.13b]$$

Combining equations [4.2], [4.10], and [4.13] gives the following expression for the estimated lens power, where b is given by equation [4.12]:

$$L = \frac{n}{v'_L-(b-1)LT} - \frac{n}{v_L-b\times LT} \qquad [4.14]$$

In equation [4.14] the distance v'_L is the vitreous depth and the distance v_L is the distance from the anterior surface of the lens to the primary image formed by the cornea. Assuming that the cornea is a thin lens located at the anterior principal plane of the cornea, we have $v_L = s'_K - ACD - CCT - \overline{H_1V_1}$. The distance s'_K is found by applying the conjugation formula to the cornea: $n/s'_K = 1/s_K + K$. If we use the approximatio $1/s_K = R$, we obtain:

$$v_L = \frac{n}{R+K} - ACD - CCT - \overline{H_1V_1} \qquad [4.15]$$

Finally, we arrive at an equation for lens power dependent on the measured parameters (VD, R, K, K_2, ACD, CCT, and LT) and the parameter b:

$$L = \frac{n}{VD-(b-1)LT} - \frac{n}{\frac{n}{R+K}-ACD-CCT-\overline{H_1V_1}-b\times LT} \qquad [4.16a]$$

Where:

$$\overline{H_1V_1} = -\frac{1}{n_K} CCT \frac{K_2}{K} \qquad [4.16b]$$

4.2.3 Value of the *b* Coefficient

The b coefficient (equation [4.11]) depends on the value of the refractive indices, the ratio of the posterior to anterior radii of curvature of the lens, and on the square of the magnification of the lens. The ratio of anterior to posterior lens radius of curvature changes with age and with accommodation (Jones et al, 2007; Borja et al, 2008; Dubbelman et al, 2005). Using age-dependent in vivo data from Dubbelman et al (2001) to represent the

relaxed lens and age-dependent in vitro data from Borja et al (2008) to represent the maximally accommodated lens, the ratio of posterior to anterior lens varies from -0.51 to -0.72. For the calculation of lens power, we use in equation [4.12] a fixed value of $R_4/R_3 = -0.6$ located in the mid-point of the range and a fixed value of the equivalent index $n_L = 1.43$. The value of b is then given by:

$$b = \frac{0.650 - 0.584 M_L^2}{1 - M_L^2} \qquad [4.17]$$

With this assumption, the only remaining source of inter-individual variability of the coefficient b is the lens magnification. An approximate expression of the magnification in terms of the measured ocular distances and refractive error can be obtained by assuming that the lens is a thin lens with a lens center located at the mid-point of the lens vertices. The object and image distances (s_L, s'_L) of the lens in the expression of the magnification are then replaced with $v_L - LT/2$ and $v'_L + LT/2$, respectively, where the distance v'_L is the vitreous depth and v_L is given by equation [4.15]. The approximate expression of the magnification then becomes:

$$M_L = \frac{VD + \frac{LT}{2}}{\frac{n}{R+K} - ACD - CCT\left(1 - \frac{1}{n_K}\frac{K_2}{K_1}\right) - \frac{LT}{2}} \qquad [4.18]$$

To evaluate the error in the magnification predicted by the approximate expression of equation [4.18], an age-dependent model of the relaxed paraxial eye with four surfaces was generated with an adjusted vitreous depth to vary the refractive error at the corneal plane, from -10 D to +10 D (axial ametropia). Dimensions of the cornea, lens, and anterior chamber depth were obtained from the in vivo Scheimpflug data of Dubbelman et al (2001). The parameters of the eye model are shown in Table 4.2. Figure 4.2 shows the exact ($M_L = s'_L/s_L$) and approximate (equation 4.18) values of M_L for a 20 year old relaxed

eye for refractive errors ranging from -10 D to +10 D (top) and for an emmetropic eye as a function of age (bottom). Over the range of refractive errors, the maximum relative difference between the approximate and exact value of M_L^2 is 3.5% (0.464 vs 0.481). The value of M_L is found to be approximately independent on age. This analysis demonstrates that a close estimate of the value of M_L can be calculated from the measured biometric data.

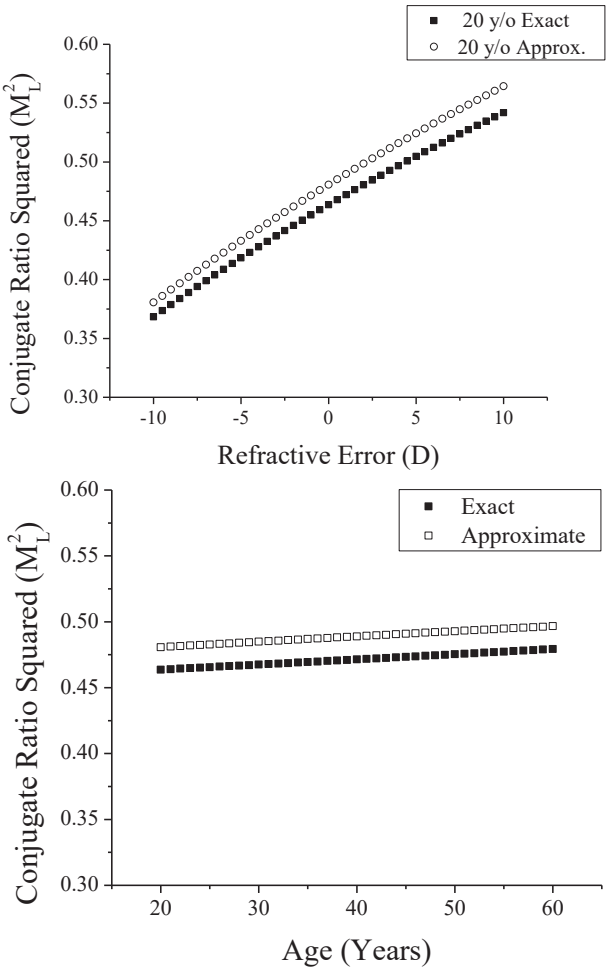

Figure 4.2: (Top) Exact and approximate conjugate ratio squared for a relaxed 20 year old eye (Dubbelman eye model) as a function of the refractive error. (Bottom) Exact and approximate conjugate ratio squared vs age for the relaxed age-dependent emmetropic Dubbelman eye model.

4.2.4 Error Analysis

To evaluate the error in the lens power predicted by equation [4.16a] with the coefficient *b* predicted by equation [4.17] and magnification provided by equation [4.18], the age-dependent model of the relaxed paraxial eye with refractive error ranging from -10 D to +10 D (see Section 4.2.3 and Table 4.2) was used. In addition, an accommodated 20 year old eye was modeled by using curvature, thickness and refractive index acquired from isolated lenses (Borja et al, 2008), corresponding to a fully accommodated state. The parameters of the two eye models are shown in Table 4.2. Equation [4.16a] was applied to calculate lens power. The value produced by the calculation was compared to the actual effective power of the lens obtained using the thick lens power formula.

Table 4.2: Predicted error eye model parameters, with equations representing the age-dependent model for the relaxed eye (based on data from Dubbelman et al, 2001 and Borja et al, 2008).

Parameter	Age-dependent relaxed Eye	20 year old accommodated
Anterior Corneal Radius (mm)	7.8	7.8
Posterior Corneal Radius (mm)	6.5	6.5
Corneal Thickness (mm)	0.55	0.55
Refractive index, air	1	1
Refractive index, cornea	1.376	1.376
Refractive index, aqueous	1.336	1.336
Refractive index, vitreous	1.336	1.336
Refractive index, lens equivalent	1.441 - (0.00039*Age)	1.433
Anterior Chamber Depth (mm)	3.87 - (0.01*Age)	2.75
Anterior Lens Radius (mm)	12.9 - (0.057*Age)	7.26
Posterior Lens Radius (mm)	-6.2 + (0.012*Age)	-4.67
Lens Thickness (mm)	2.93 + (0.024*Age)	4.16

Figure 4.3 shows the value of prediction error in lens power produced for the relaxed emmetropic eye as a function of age, as well as for the 20 year old relaxed and accommodated eyes and for the 60 year old eye in terms of refractive error. For the 20 year old eye, the prediction error ranged from -0.14 to -0.16 D in the relaxed state and 0.30 to

0.65 D in the accommodated state. In the 60 year old eye, the predicted error ranges from 0.13 to 0.50 D. The calculations show that for a range of ±10 D of ametropia and an age range of 20 to 60 years, the predicted error is within ±0.5 D for the relaxed eye. For the accommodated eye, the method overestimates the lens power by 0.30 D to 0.65 D, depending on the refractive error.

Figure 4.4 shows the predicted error of the change in lens power for the 20 year old eye in terms of refractive error. The change in lens power is 9.5 D. The prediction error monotonically increases from 0.46 to 0.79 D as the refractive error changes from -10 to +10 D. For an emmetropic eye, the prediction error is 0.59 D. These values correspond to a relative error ranging from 4.7% to 8.1% of the total change in lens power (less than 10%).

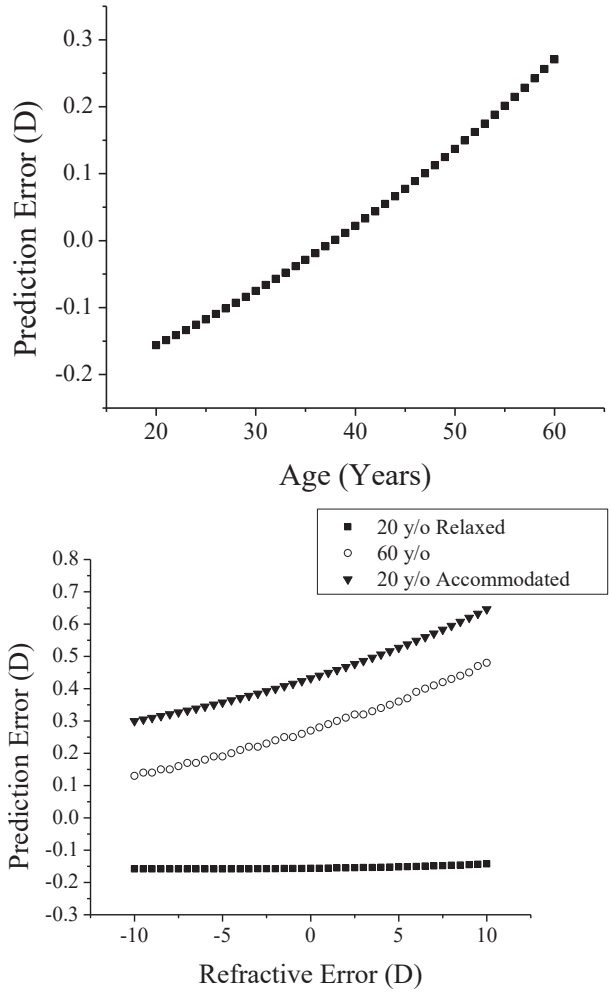

Figure 4.3: (Top) Predicted error the approximate constant b for the relaxed eye vs age. (Bottom) Prediction error for the 20 year old relaxed and accommodated, and the 60 year old model in terms of refractive error.

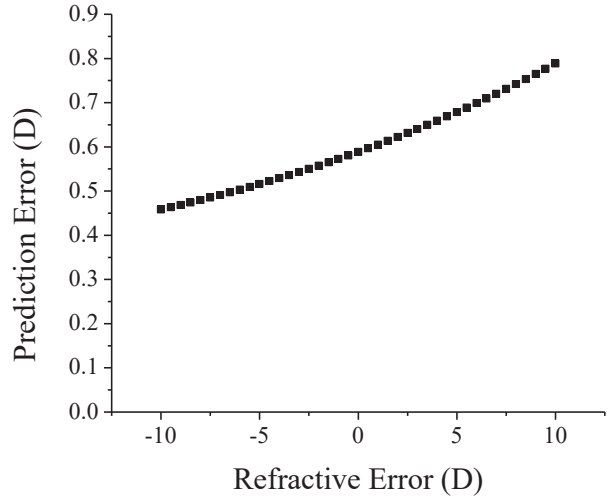

Figure 4.4: Predicted error of the change in lens power for the 20 year old vs refractive error. The change in lens power is 9.7 D.

4.3 Measurement of Lens Power Using Whole Eye OCT

4.3.1 Methods

Using the method described above, applied to whole-eye OCT images, we calculated the lens power of 16 eyes in 8 subjects enrolled in a study approved by the University of Miami's Institutional Review Board. Age ranged from 21 to 31 years (mean = 24.5±3.3 years). Objective spherical equivalent refraction measured using a commercial autorefractor (AR-1, Nidek, Japan) ranged from -5.8 to +3.8 D (mean = -2.3±2.8 D). Refraction was measured without cycloplegia. Anterior and posterior corneal curvature was acquired using a commercial anterior segment biometry system (Pentacam, Oculus, Germany). The mean value of the flattest and steepest meridian in the central 3 mm zone was used. Corneal thickness, anterior chamber depth, lens thickness, and vitreous depth were obtained using a custom built extended-depth spectral domain OCT system with a central wavelength of 840 nm and an axial resolution of 8 μm (Figure 4.5) in air. A detailed description of the OCT system can be found in Chapter 5 of this dissertation. The OCT system is coupled to an accommodation target that allows the operator to adjust the accommodative demand. The target was adjusted to lie at the subject's uncorrected far point. The OCT system was aligned under guidance of a live display of the cross-sectional image until the lens thickness was perceived to be maximal. The A-line that corresponds to the corneal apex was selected for all measurements. The ocular distances were determined by finding the position of the intensity signal peaks corresponding to corneal and lens surfaces and the retinal pigment epithelium.

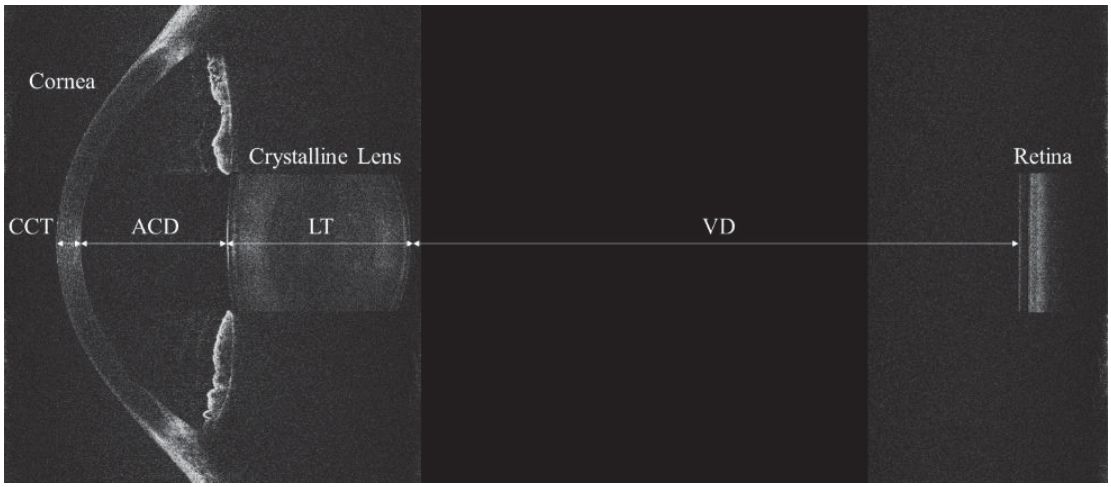

Figure 4.5: Image acquired using the extended-depth SD-OCT system and a representative A-line of the center placed above.

The OCT image was processed to convert optical distances into geometrical distances using the following group refractive indices at 840 nm (Ruggeri et al, 2012): cornea = 1.387, aqueous humor = 1.342, crystalline lens = 1.415, vitreous = 1.341, retina = 1.38. The precision of ocular distance measurements was evaluated in a study on 1 subject where 28 images were acquired in sequence. The standard deviation of the measurements was ±0.002 mm for the cornea, ±0.012 mm for the anterior chamber depth, ±0.018 mm for the lens, and ±0.011 mm for the vitreous depth.

The measured values were entered in equation [4.16a] to calculate the lens power. The value of b was calculated using equations [17] and [18]. Corneal power was calculated by applying the formula for the power of a thick lens with a refractive index of 1 for air, 1.376 for the cornea, and 1.336 for aqueous.

4.3.2 Results

The values measured in the 16 eyes are summarized in Table 4.3. These values were used to find the parameters required to calculate lens power using equation [4.16a] (Table 4.4). Lens power is shown in Figure 4.6 against axial eye length. All data is plotted on the same graphs, without separation of left and right eyes. Lens power ranged from 21.66 D to

27.60 D, with a mean of 24.30±1.70 D. Lens power was found to decrease as axial eye length increased. This is in agreement with the findings of Iribarren (2012) who shows a statistically significant increase in lens power with a decrease in axial eye length. However, the sample size of the present study is too small to make any definite conclusions as to the relation between lens power and ocular components.

Table 4.3: Data collected on 16 eyes of 8 subjects. SEQ = spherical equivalent refraction, for all other symbols, see Table 4.1.

Subject # and eye	Age (years)	SEQ, R (D)	R_1 (mm)	R_2 (mm)	CCT (mm)	ACD (mm)	LT (mm)	VD (mm)
1 OD	22	-4.07	7.74	6.37	0.488	3.783	3.438	18.302
1 OS	22	-5.62	7.79	6.44	0.481	3.773	3.432	18.927
2 OD	26	-5.07	7.53	6.19	0.526	3.224	3.709	17.265
2 OS	26	-5.81	7.50	6.18	0.533	3.303	3.660	17.714
3 OD	26	-3.76	7.52	6.00	0.523	3.039	3.475	17.352
3 OS	26	-2.96	7.47	5.94	0.518	2.991	3.552	16.959
4 OD	31	-0.63	7.46	6.23	0.475	3.331	3.670	16.138
4 OS	31	-0.88	7.41	6.08	0.476	3.406	3.679	15.924
5 OD	21	-1.75	7.68	6.40	0.540	3.215	3.567	15.970
5 OS	21	-0.13	7.68	6.39	0.537	3.175	3.618	15.942
6 OD	21	-5.13	7.86	6.49	0.523	3.622	3.452	18.567
6 OS	21	-4.88	7.81	6.47	0.522	3.705	3.425	18.540
7 OD	23	-1.13	7.83	6.41	0.525	2.968	3.797	16.438
7 OS	23	-0.62	7.73	6.34	0.509	3.048	3.752	16.336
8 OD	26	1.50	7.61	6.40	0.549	2.797	3.994	14.689
8 OS	26	3.81	7.58	6.36	0.534	2.873	3.921	14.607
AVG	24.5	-2.32	7.64	6.29	0.516	3.266	3.634	16.854
STD	3.31	2.79	0.14	0.17	0.024	0.318	0.174	1.329

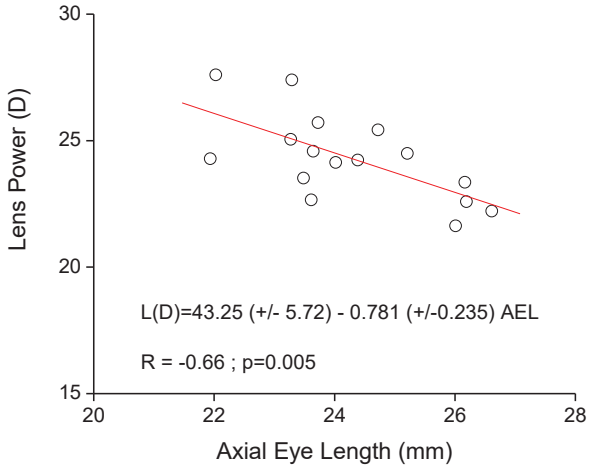

Figure 4.6: Lens power vs axial eye length for 16 eyes of 8 subjects.

Anterior segment distances and predicted lens power obtained from this study were in good agreement with the age-dependent biometric data of Dubbelman (2001) at the age corresponding to the average age of our subjects (24.5 years) (Dubbelman / present study): Anterior chamber depth: 3.08 / 3.27 mm, lens thickness: 3.52 / 3.63 mm, lens power: 24.1 / 24.3 D.

Table 4.4: Calculated values used in the equations for lens power.

Subject # and eye	K (D)	K_2 (D)	H_1V_1 (mm)	M_L	b	L (D)
1 OD	42.41	-6.28	0.053	0.695	0.712	21.66
1 OS	42.16	-6.21	0.051	0.676	0.706	22.23
2 OD	43.59	-6.46	0.057	0.659	0.701	25.45
2 OS	43.79	-6.47	0.057	0.664	0.702	24.52
3 OD	43.46	-6.67	0.058	0.675	0.705	24.26
3 OS	43.73	-6.73	0.058	0.683	0.708	24.18
4 OD	44.09	-6.42	0.050	0.718	0.720	22.70
4 OS	44.28	-6.58	0.051	0.710	0.717	23.56
5 OD	42.83	-6.25	0.057	0.659	0.701	27.43
5 OS	42.82	-6.26	0.057	0.690	0.710	25.09
6 OD	41.79	-6.16	0.056	0.665	0.702	23.37
6 OS	42.07	-6.18	0.056	0.677	0.706	22.62
7 OD	41.89	-6.24	0.057	0.671	0.704	25.75
7 OS	42.45	-6.31	0.055	0.688	0.709	24.62
8 OD	43.28	-6.25	0.058	0.683	0.708	27.66
8 OS	43.44	-6.29	0.056	0.725	0.723	24.35
AVG	43.01	-6.36	0.055	0.684	0.708	24.34
STD	0.81	0.18	0.003	0.020	0.007	1.70

4.4 Discussion

This chapter demonstrates the application of a whole-eye OCT system combined with corneal topography and refraction to the calculation of lens power using an optimized version of the Bennett method that relies on a thin lens approximation.

In the original Bennett method, the positions of the principal planes of the lens are calculated by assuming that the ratio of posterior to anterior radius of the lens is the same as that of the Gullstrand eye model. The position of each principal plane of the lens is then calculated from the lens thickness and two fixed constants. Here, a thin lens model is used and demonstrates that there is a position of the thin lens that produces a zero prediction error (equation [4.6]). In first approximation, the distance from the anterior lens vertex to the optimal thin lens position is proportional to the lens thickness, with a proportionality constant that depends on the conjugation ratio of the lens and on the ratio of posterior to anterior lens radius (equation [4.12]).

A theoretical error analysis using eye models of different ages, accommodative states, and refractive errors suggests that the theoretical prediction error is within ±0.5 D for the relaxed eye if the distance from anterior vertex to lens center is assumed to be independent of the lens shape. This approach provides a direct simple expression of lens power in terms of ocular distances, corneal power and refraction with a single coefficient that depends on ocular dimensions and refractive error (b, equation [4.6]). The modified method significantly reduces the theoretical prediction error compared to the methods that use a fixed position for the thin lens relative to the anterior lens vertex (Rozema et al, 2011), particularly in ametropic and accommodated eyes. In principle, the error could be further reduced by using an age- and accommodation- dependent estimate of the ratio of posterior

to anterior lens radius, which can be calculated for instance using the biometric data of Dubbelman et al (2001, 2005).

Similar to the Bennett method, the proposed modified method requires a measurement of lens thickness, which is not always available (Rozema et al, 2011). When lens thickness is unknown, an estimate of lens power can be calculated by using a fixed value or an age-dependent model for lens thickness. In that case, vitreous depth is estimated by subtracting lens thickness, anterior chamber depth and corneal thickness from the axial eye length. For instance, when the error analysis using the eye models described above is repeated using a fixed value of thickness equal to 4 mm, the theoretical prediction error for the relaxed lens power remains within ±1 D over a wide range of refractive errors (-10 D to +10 D).

In the calculation of the prediction error in lens power as a function of refractive error, the ametropic eye was modeled by changing only the axial eye length (axial ametropia). If instead we model ametropia by changing only the corneal shape (refractive ametropia), we find that the prediction error in lens power is independent of refractive error. Indeed, in that case both the vitreous depth, VD, and the quantity R+K remain constant as the refractive error changes. The approximate values of M_L (equation [4.18]) and b (equation [4.17]), and the predicted value of the lens power (equation [4.16a]), will therefore remain constant and equal to the value obtained for the emmetropic eye.

Comparing the lens power predicted with the described method to that of Bennett, we find that the Bennett method produces lens power values that are lower by -2.18 D on average. This difference stems mostly from the fact that the Bennett method calculates the corneal power from the anterior corneal radius only, using the standard keratometric index

of 1.3375. Use of the standard keratometry formula produces an overestimation of corneal power by approximately 1.2 D on average in normal corneas. The remaining difference is due to differences in the location of the principal planes of the lens. The difference in methods of calculation of corneal power accounts for most of the difference between our lens power values and the values of Rozema et al (2011, 2012). The values obtained in the present study are in closer agreement with values obtained using a keratometric index of 1.3315 (Iribarren et al, 2012), which is derived assuming a two-surface model of the cornea, with a value of anterior to posterior radius of curvature provided by the Gullstrand model eye (0.889). Recent studies show that the ratio of posterior to anterior radius of curvature is on the order of 0.82 to 0.84 (Dubbelman et al, 2006, Dunne et al, 1992), corresponding to a keratometric index of 1.328 to 1.329. This value is in good agreement with the data that obtained in this study. According to Table 4.3, the mean ratio of posterior to anterior curvature is 0.824±0.013, corresponding to a keratometric index of 1.328. This observation also brings to attention the fact that special care must be taken when comparing values of lens power obtained using the Bennett method in different studies. Use of different methods to calculate corneal power may produce significant differences in the calculated lens power. Studies that relied on the standard keratometric index of 1.3375 will tend to underestimate the lens power.

Another factor that may cause differences in published values of lens power is the difference in the position of the posterior boundary that is used as a reference for the measurement of axial eye length. In our study we used the inner boundary of the retinal pigment epithelium (RPE) as a reference, since this boundary is adjacent to the photoreceptors. In measurements acquired using ultrasound or commercial optical

biometry systems, the inner limiting membrane (ILM) serves as the reference surface. Axial eye length measured with these devices must therefore be corrected by adding the retinal thickness (approximately 0.2 mm) (Li et al, 2015). Without this correction, the lens power will be slightly overestimated.

The extended depth OCT provides all of the ocular distances needed for determining lens power using equation (Dubbelman et al, 2001), with high precision and in a single measurement. In principle, since the OCT system provides cross-sectional images of the corneal and lens contours, the lens power could have been calculated from OCT images and refraction only, without resorting to a separate measurement of corneal topography. However, accurate measurements of corneal and lens shape from OCT images requires the development and validation of image processing algorithms for segmentation, curve fitting, motion compensation, and distortion correction (Dubbelman et al, 2001; Ortiz et al, 2012; Zhao et al, 2010). Ideally, these algorithms must be applied to three-dimensional OCT images to take into account ocular surface asymmetry. These techniques are beyond the scope of the present study, which presents an alternative method to calculate lens power without requiring measurements of the lens radii of curvature.

The uncertainty in the equivalent index produces a large uncertainty in the lens power calculated with the lens maker formula, as discussed in the introduction. According to equation [4.12], the expression of b also depends on the equivalent refractive index. However, the influence of this dependence on the lens power is minimal. For instance, for the 20 year old relaxed lens, the change in lens power is only 0.26 D when the refractive index is changed from 1.40 to 1.44.

The extended-depth OCT system provides high precision measurements of the ocular distances, including lens thickness with a single device. The advantage of this approach compared to A-scan optical or ultrasound biometry, is that visualization of the image during the measurement helps ensure proper alignment of the eye. We estimate that the alignment precision for a trained operator is within ±0.2 mm. An error analysis shows that within this range, alignment errors produce an error that is below the 5.2 μm per pixel axial digital resolution of the images. In addition, we can select the A-line from the two-dimensional image along which ocular distances are measured, and we can use individual values of the refractive index for each ocular medium to convert from optical to geometrical distances. Together, these advantages help increase accuracy and precision of the calculation of lens power.

One limitation is that the method relies on a paraxial model of the eye. The paraxial retinal conjugate is assumed to coincide with the far point of the eye determined by spherical equivalent refraction. The calculation ignores the effect of ocular aberrations which may shift the best focus of the eye away from the paraxial focus. The method provides a mean value of lens power calculated using spherical equivalent refraction and mean corneal power across the central 3mm diameter optical zone. Another limitation is that refraction and OCT imaging were performed without cycloplegia. The measured lens power may therefore not correspond to the fully relaxed accommodative state. Some of the variations in lens power and lens thickness found between the 16 subjects could be due in part to the fact that some of the subject accommodated during refraction or imaging. However, the range and average values of the lens power are consistent with previous studies performed under cycloplegia.

4.5 Conclusion

An improved modification on the Bennett method to calculate lens power from corneal topography, refraction, and ocular biometry using extended-depth OCT is presented. The estimated theoretical uncertainty in the predicted relaxed lens power is within ±0.5 D for refractive error ranging from -10 D to +10 D. The estimated relative theoretical prediction error for the change in lens power during accommodation is on the order of 10%. A preliminary study on 8 subjects demonstrates that the method provides values of lens power that are in close agreement with previously published studies. This method will be used with the subsequent measures of refraction and ocular biometry to correlate lens power with accommodation.

Chapter 5: Integration of Anterior Segment Biometry Modules (Aim 3)

5.1 Purpose

The purpose of Aim 3 is to integrate an extended depth anterior segment spectral domain optical coherence tomography (SD-OCT) system and a trans-scleral SD-OCT system with the autorefractor and accommodation target described in Chapter 3. The implementation of a means to acquire biometric information of the eye will allow for correlation of the refractive data collected by the autorefractor to conformational changes occurring in the eye during accommodation. Specifically, in this study we will measure the relation between the power change measured with the autorefractor and the change in lens power calculated from biometry using the method presented in Chapter 4, in a proof-of principle study performed on 3 subjects with varying accommodative demands.

5.2 Optical Coherence Tomography (OCT)

Optical coherence tomography is an optical imaging modality based on low coherence interferometry capable of producing three-dimensional images of biological tissues (Izatt et al, 1994, Grulkowski et al, 2009). OCT imaging is often referred to as being the "optical analogous" to ultrasound imaging. Both modalities measure the time delay and intensity of echo signals produced by diffuse reflection of incident energy over a certain resolvable depth. However OCT relies on interference of light with low temporal coherence to produce the echo signal while ultrasound uses direct detection of acoustic energy. In ocular biometry, OCT is favored over ultrasound biomicroscopy because it is a non-contact and higher-resolution imaging modality capable of generating two-dimensional images with high speed.

OCT systems generally use an implementation based on the Michelson interferometer. In the Michelson interferometer, light from the source falls incident on a

beamsplitter which sends a fraction of the light energy to a reference mirror and the remainder to the sample under test. Light incident on the sample, or in the case of this application, ocular tissue, is reflected off of the various tissue boundaries. The light reflected back from the sample and reference mirror returns to the beam splitter where it is recombined and sent to a photodetector which produces the signal that is used in the formation of images.

OCT systems use a broadband source, typically a super-luminescent diode. Broadband sources have low temporal coherence. When a source with low temporal coherence is used in a Michelson interferometer, interference patterns are obtained only when the path difference of the light returning from the sample and reference arms of the interferometer is within the coherence length of the source.

The depth-dependent signal produced at a given position across the sample is called an A-scan. To obtain a 2D image, multiple A-scans are taken across the sample by using two galvanometer scanners which scan the sample beam laterally across the sample. These A-scans are combined to form a cross-sectional image, or B-Scan. Multiple B-scans can then be acquired to form a 3D image of the tissue. Variations in the scattering properties of the layers of the tissue being imaged will generate varying intensity values, which allow for one to distinguish layers, boundaries, or tissue structures in the OCT image. In the first OCT systems (time-domain OCT), the A-scan signal was acquired by translating the mirror in the reference arm (Figure 5.1). In time-domain OCT, the detected signal intensity is given by:

$$I_{12}(\tau) = I_1 + I_2 + G_{12}(\tau) \qquad [5.1]$$

Where I_1 and I_2 are the intensities returning from the sample and reference arms of the interferometer, τ is the time delay between the two reference arms, and G_{12} is the interferogram or interference term. This term is the cross correlation of the amplitude of the waves returning from the sample and reference arms of the interferometer. If E_1 and E_2 are the wave amplitudes returning from the reference and sample arm respectively, then G_{12} can be expressed as:

$$G_{12}(\tau) = 2Re(E_1^*(t)E_2(t-\tau)) \qquad [5.2]$$

Where t is time, and E_1^* is the complex conjugate of E_1. The time-dependent signal is recorded using a photoreceiver placed in the detector arm of the interferometer.

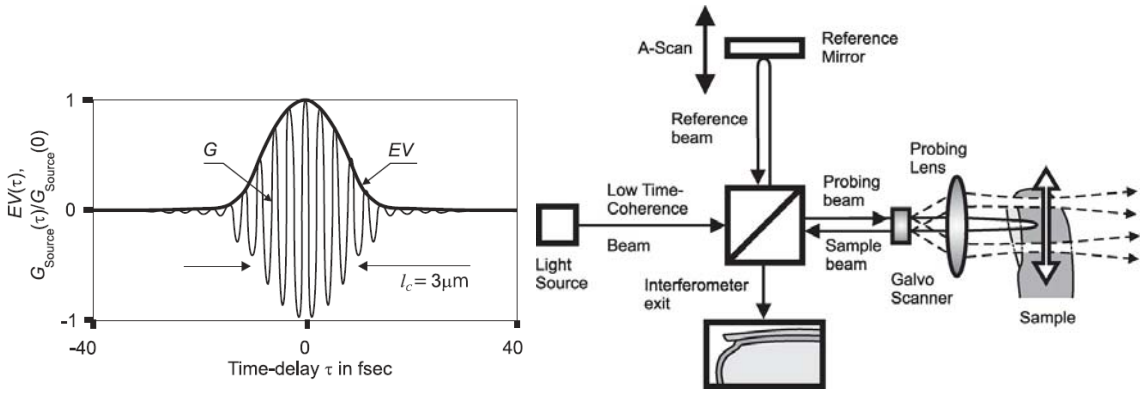

Figure 5.1: (Left) Interferogram (G) and signal envelope (EV) plotted as a function of the signal's time delay. (Right) Schematic of a time-domain OCT system. The reference mirror is translated axially to create an A-scan. The galvo scanner translates the sample beam laterally across the sample to generate a series of A-scans (Adapted from Fercher, 2009).

Currently, most commercial ophthalmic OCT systems use a spectral-domain implementation. In spectral-domain OCT (SD-OCT), the intensity signal is derived from a measurement of the spectral intensity distribution of the light in the detector arm of the interferometer. In SD-OCT, the reference arm is fixed and the photodetector is replaced with a spectrometer that uses a diffraction grating and line-scan array (1D photodetector array). The A-scan signal and measured spectrum form a Fourier transform pair. The

interference signal along each A-line can therefore be calculated by performing a Fourier transform of the recorded spectrum.

The main advantage of spectral-domain OCT over time-domain OCT is acquisition speed. In time-domain systems, the signal at each position along an A-scan is acquired by moving the reference arm mirror to match the optical path difference between the sample arm and reference arm. The time that it takes to acquire each A-scan becomes the limiting factor for the acquisition speed. In spectral-domain, the entire A-scan is captured in a single spectral measurement. The acquisition speed is limited only by the readout speed of the line-scan array. Spectral-domain OCT systems can therefore acquire images at a much faster rate than time-domain OCT.

The major limitation of spectral-domain OCT over time-domain OCT is that there is a marked sensitivity roll-off in spectral-domain OCT. This sensitivity roll-off limits the imaging depth, typically to a few millimeters.

5.2.1 OCT Biometry of Accommodation

Anterior segment biometry using a variety of imaging modalities is discussed in detail in Chapter 2. Ultrasound biomicroscopy can acquire whole anterior segment images at a high rate, but its resolution is low and it is not convenient for integration with refraction measurements. Scheimpflug imaging provides high resolution images of the anterior segment, but is difficult to use in a dynamic setting due to limited imaging speed.

Optical coherence tomography has been shown to be capable of imaging accommodative response in real-time (Radhakrishnan et al, 2001). Richdale et al (2008) measured the change in crystalline lens thickness with accommodation using a commercial OCT system (Visante OCT), and the results show values comparable to those obtained

with Scheimpflug and ultrasound imaging. However, there exists an intrinsic trade-off for OCT imaging involving image resolution and imaging depth. This sensitivity roll-off limits the imaging depth, typically to 3-4 mm. In order to capture the entire anterior segment, an imaging depth of 10-15 mm is needed.

Obtaining sufficient imaging depth to produce images of the full anterior segment during accommodation was a challenge resolved by new OCT imaging methods. Techniques for increasing the imaging depth include removal of the complex conjugate (Wojtkowski et al, 2002; Yun et al, 2004; Zhang et al, 2005), utilizing newer line-scan arrays with a larger number of pixels (Grulkowski et al, 2009; Marcos et al, 2014), or using an optical switch in the reference arm. Ruggeri et al (2012), at the Ophthalmic Biophysics Center, demonstrated whole anterior segment imaging in real time during accommodation via the implementation of an optical switching technique. Using a similar technique, Shao et al (2013) have also demonstrated real-time whole anterior segment imaging with optical switching and ciliary muscle imaging, during accommodation, but their system does not demonstrate synchronous acquisition of aberrometric and biometric information, and the accommodation stimulus design does not allow precise synchronization of the stimulus and data acquisition sequence.

New OCT systems based on swept-source approaches, which utilize vertical-cavity surface-emitting laser (VCSEL) light sources provide new opportunities for large depth imaging (Grulkowski et al, 2012; Neri et al, 2014). Swept source OCT systems can provide a whole eye axial image (Figure 5.2). They provide much faster imaging and avoid the sensitivity roll-off in depth, but VCSEL sources are still under development and usually operate at 1300 nm, which reduces axial resolution.

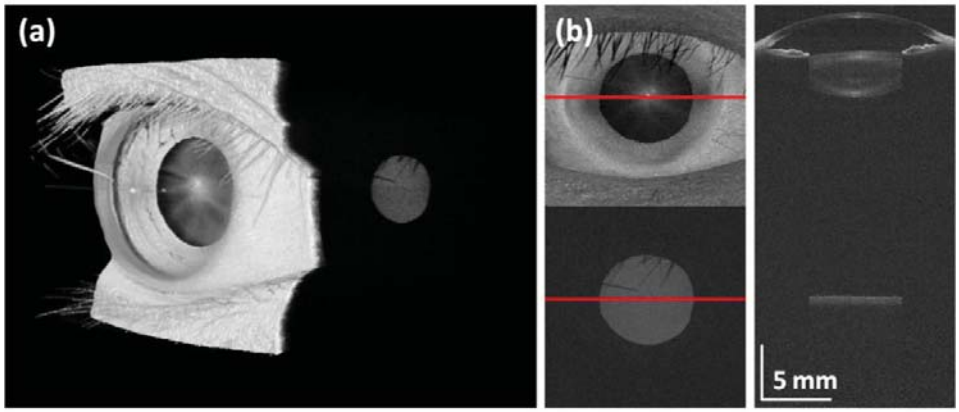

Figure 5.2: OCT images acquired with a swept source OCT system. (a) Whole eye volumetric scan. (b) En face image reconstructed from the OCT data set. (Right) Whole eye tomographic scan showing the cornea, crystalline lens, and retina. (Adapted from Grulkowski et al, 2012).

The OCT system used as the axial biometry module in this integrated system is based on the OCT system developed by Ruggeri et al (Figure 5.3). A detailed description of the system has been previously published (Ruggeri, 2012). Briefly, it is a spectral domain OCT with a central operating wavelength of 840 nm, a CMOS line scan camera with a single frame imaging depth in air of approximately 10 mm. The system has an axial resolution of 10 μm. An image of the whole eye is acquired by using an optical switch, moving between three reference planes. This allows the capture of the anterior segment in two frames, and the retina with one additional frame.

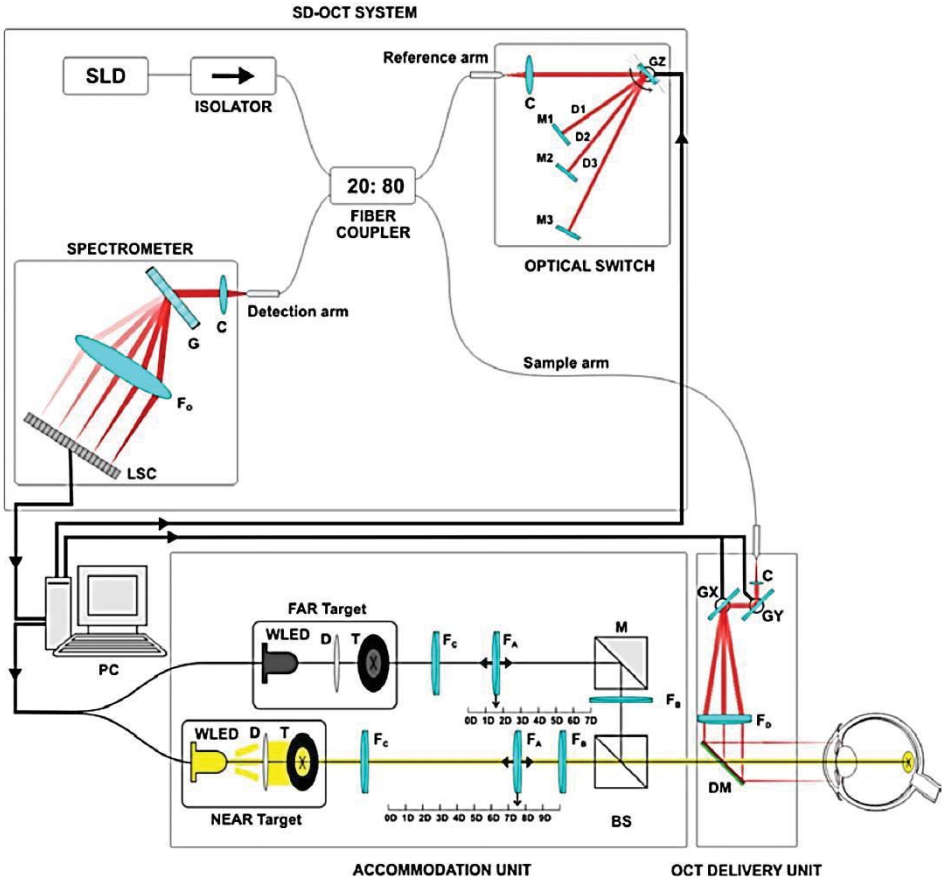

Figure 5.3: Schematic of the extended-depth SD-OCT system used as the base biometry module in the current integrated system (Shown here with schematic of the original accommodation stimulus). BS: Beamsplitter. C: Collimator. D: Diffuser. DM: Dichroic mirror. F_A: Auxiliary lens. F_B: Badal lens. F_C: Collimating lens. F_D: OCT delivery probe objective. F_o: Spectrometer objective. G: Grating. GX, GY, GZ: Galvanometer scanners. LSC: Line-scan camera. M, M1, M2, M3: Mirrors. SLD: Light source. T: Target. WLED: White light LED. (Adapted from Ruggeri et al, 2012).

5.3 Anterior Segment SD-OCT Integration

The basis for this design is the OCT developed by Ruggeri et al (2012) which is described in Section 5.2.1. There are two main steps necessary to make integration possible; modification of the OCT delivery probe and synchronization of the acquisition signal of the OCT to the autorefractor.

5.3.1 Design Specifications

The integration of the anterior segment OCT delivery probe needed to meet the following criteria:

- The relay optics base cannot have a footprint greater than 50 x 50 mm.
- The probe must allow for adjustment of the OCT objective lens independent of the galvanometer block to adjust for telecentricity of the scan.
- The probe must allow for adjustment of the fixed galvanometer mirror/objective lens unit independent of the probe base to allow for the adjustment of the probe working distance.
- Once integrated with the autorefractor mount, the delivery probe must be capable of rotation (±15 degrees) and lateral translation (±5 mm).

5.3.2 Original Delivery Probe Design

The original delivery probe is shown in Figure 5.4. The base of the probe is a 60 mm 6-way cage cube (LC6W, Thorlabs, Newark, NJ) with a 50 x 50 mm hot mirror (#64-470, Edmund Optics, Barrington, NJ) mounted at 45 degrees. The hot mirror relayed the OCT scan signal provided by the galvanometer/source block mounted perpendicular to the optics' base. While this mounting scheme allowed for angle adjustment of the hot mirror, its large footprint and block profile make lateral translation and base rotation difficult. The rotation angle is limited by the cage, since it interfered with other opto-mechanical components in close proximity. Lateral translation of the probe was also difficult due to a tolerance offset between the outer thread diameter of the screw used to fix the probe in place and the milled slot along which the probe is meant to travel. This meant that lateral translation would also result in some axial displacement.

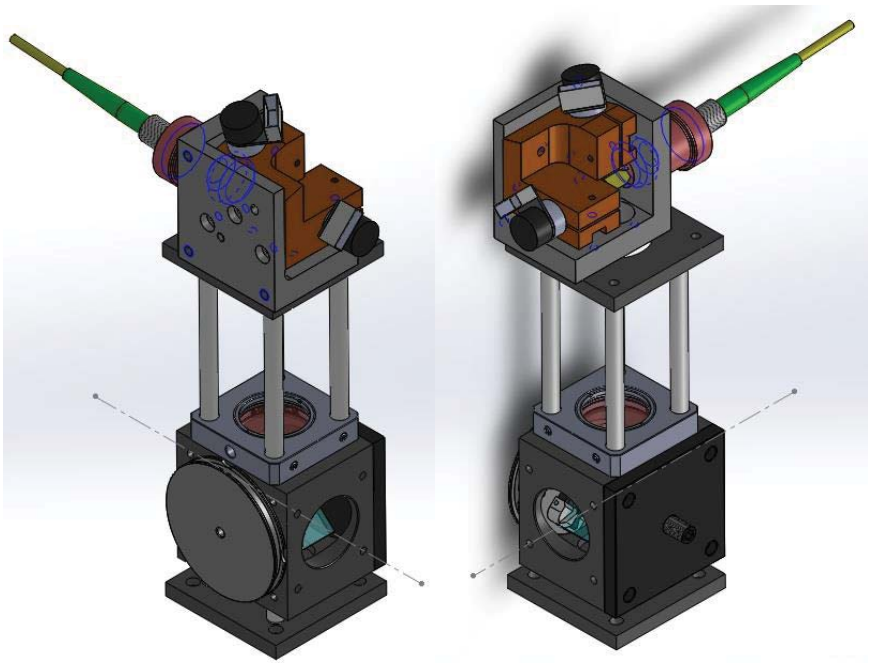

Figure 5.4: Isometric views of the left-hand (Left) and right-hand (Right) sides of the original extended-depth SD-OCT delivery probe.

5.3.3 Modified Delivery Probe

The redesigned delivery probe does away with the cage mount and hot mirror of the original design. The new probe does retain the use of cage rods to allow for adjustment of the telecentric scan lens. The new probe also incorporates a new custom dichroic mirror with sharp-cut-off (Semrock, Rochester, New York) (Figure 5.5) that replaces the original hot mirror. The dichroic mirror allows for the partial transmission of the autorefractor's probe beam at 750 nm, transmission of the visible light of the accommodation stimulus, and reflection of the OCT beam.

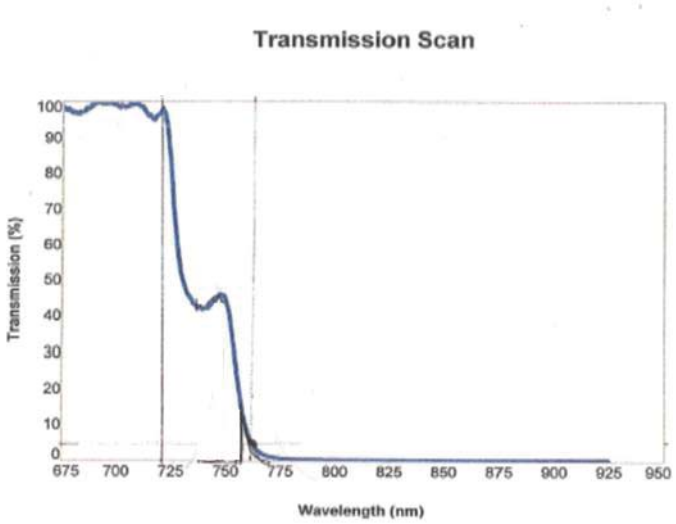

Figure 5.5: Transmission curve of the dichroic used to replace the hot mirror in the original OCT probe design. Transmission of the central wavelength of the autorefractor probe beam is approximately 45%.

5.3.3.1 Dichroic Mount and Base

The OCT probe base and dichroic mirror mount is made up of three components; an upper mirror frame, a lower mirror frame, and an outer mirror enclosure. The upper mirror mount has an open top portion serving as a clear aperture for the galvanometer scanning block and a milled flat at a 45 degree angle on the posterior side. The lower mirror frame is a cylindrical base with a 45 degree angle flat and four fixation holes to allow mounting to a rotation stage. The outer mirror enclosure houses the upper and lower mirror mounts, with both being fixed to the enclosure via four #8-32 flathead screws. A 30 mm clear aperture was milled perpendicular to the round face of the cylindrical enclosure serving as the viewing window for the subject.

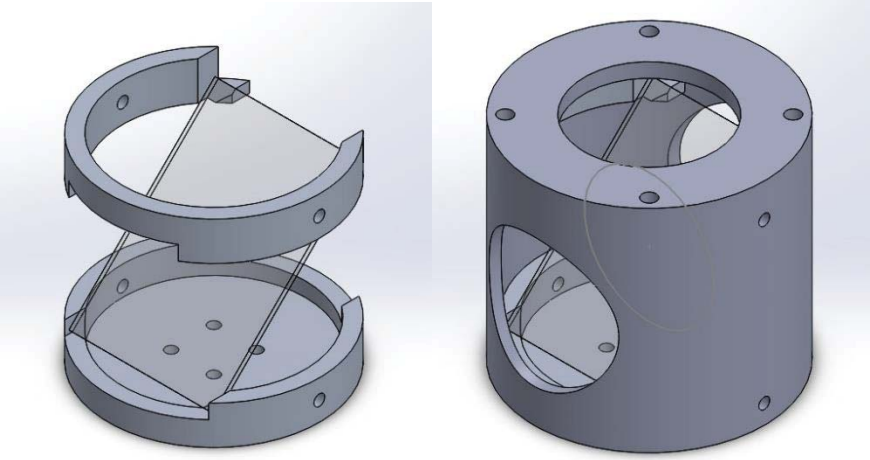

Figure 5.6: (Left) OCT probe base mirror mount without the cylindrical outer housing. The square hole pattern on the base is a series of through holes from which the probe is fixed to the rotation stage. (Right) The outer cylindrical enclosure shown on the mirror mount. The holes on the round face of the cylinder are used to fix the mirror mount halves to the outer housing. The four holes on the top flat face are for mounting the rods which hold the galvanometer block/telecentric scanning lens subassembly.

The new OCT probe base was fixed to a small rotation stage (MSRP01, Thorlabs, Newton, New Jersey). The stage allows for the probe to be rotated about its axial center for adjustment relative to the subject's visual axis. Graduations on the rotation stage allow for adjustment of the probe with one degree resolution. The probe/rotation stage assembly is then placed on the counter-sunk portion of the system base where it can be laterally adjusted with no front-to-back displacement in the probe. Once the lateral position has been adjusted, a thumb screw is tightened underneath the rotation stage through a slot in the system base to fix the probe. This satisfies the criteria of allowing the same number of degrees of freedom in the displacement of the OCT delivery probe.

The complete probe assembly is shown in Figure 5.7. The upper portion of the probe, on which the galvanometer mirror scanning block sits is a custom-milled cage frame. The frame allows for independent adjustment of the telecentric scanning lens and fixed adjustment of the galvanometer block and scanning lens. With this design, once the

position of the lens is fixed to ensure telecentricity of the OCT scan, the OCT sub assembly's position can be adjusted relative to the dichroic mirror to ensure that the scanning lens and Badal lens are confocal with respect to each other.

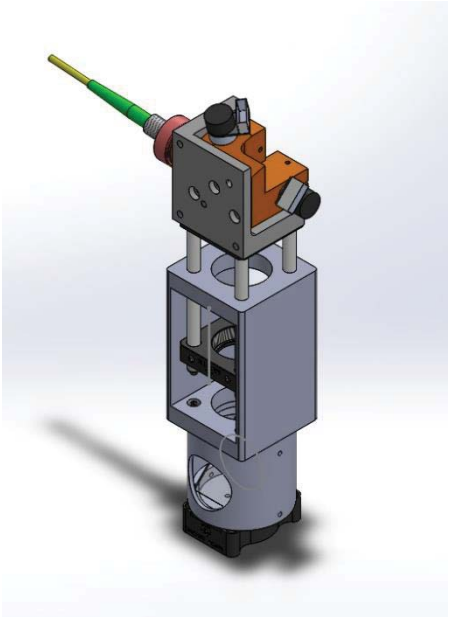

Figure 5.7: Isometric view of the updated OCT probe design. The cylindrical mirror mount is fixed to a rotation stage. The upper cage-mount frame utilizes cage rods to allow for independent adjustment of the galvo scanner and telecentric scan lens.

5.4 Trans-scleral SD-OCT Integration

The design of a fixture for the trans-scleral OCT probe exploits the intentional symmetry of the system base to allow for mounting on either side of the base. This design addresses the limitation of the previous design, which allowed imaging only of the left eye because there was insufficient mechanical clearance to mount the trans-scleral probe. There are two main steps necessary to make integration possible; creation of a probe mount which satisfies the design specifications and synchronization of the acquisition signal of the ciliary body OCT to the autorefractor. The trans-scleral OCT system is a commercially available 1325 nm SD-OCT system (Telesto, Thorlabs, Newton, New Jersey) (Figure 5.8).

The system's probe was removed from its platform arm and custom mounting hardware was designed and built for integration into the accommodation biometry system.

Figure 5.8: The Telesto 1325 nm SD-OCT system as sold by Thorlabs (www.thorlabs.com).

5.4.1 Design Specifications

The integration of the trans-scleral ciliary body imaging SD-OCT needed to meet the following design criteria:

- Independent 4-axis adjustment of the probe: x, y, and z-axis translation and rotation.
- Quick release of the probe from the mount to allow for the proper placement of the probe objective when switching between left-eye and right-eye measurements.
- The axis of rotation must lie at the focal plane of the probe objective.

5.4.2 Trans-scleral SD-OCT Mount

The trans-scleral OCT mounting apparatus can be divided into two main components; the probe housing and the tabletop probe mount. The probe housing is comprised of a two part U-bracket (Figure 5.9). The bracket allows for fixation of the probe via two base holes on the mount's base. Fixation of the probe to the tabletop probe mount is done with the probe lying on its side. The position of the probe's objective lens is

eccentric to the probe body's axis of symmetry. The probe housing takes into account the height difference of the objective when placed on either of its side faces (i.e. when changing measurement position of the probe from left eye to right eye). The probe housing is joined to the tabletop mount via a dovetail system, with the female interface milled onto the housing bracket. Once positioned, the bracket is fixed using a set screw.

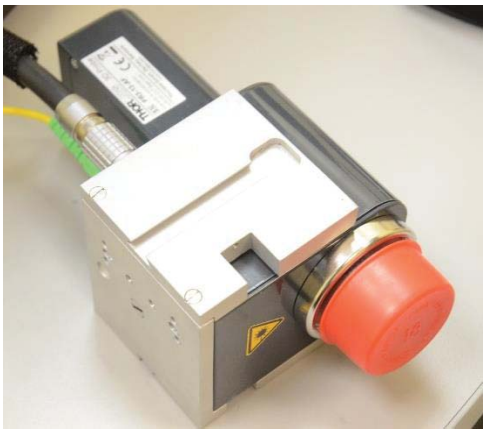

Figure 5.9: The trans-scleral SD-OCT probe affixed to the custom U-bracket with a female dovetail feature on either side to allow for mounting on either side of the main system base.

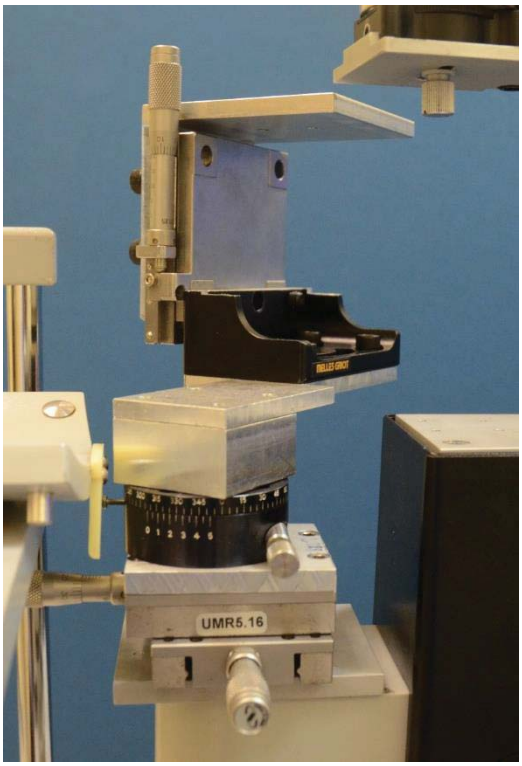

Figure 5.10: The tabletop probe mount consisted of a two-axis translation stage, a rotation stage, a rotational mounting plate, a height spacer, and an L-bracket probe seat.

The tabletop probe mount (Figure 5.10) is made up of five stacked components: a two-axis translation stage, a rotation stage, a rotational mounting plate, a height spacer, and an L-bracket probe seat. The two axis translation stage is centrally fixed on the base of the tabletop arm so that the trans-scleral SD-OCT assembly's motion is coincident with the rest of the system. The rotation stage is fixed to the translating base in such a way that the axis of rotation lies at the subject's pupil plane. The rotational mounting plate holds the height spacer and L-bracket so that once the OCT probe is placed on the mount, the axis of rotation of the probe is located at the working distance of the OCT objective lens. Preliminary imaging studies with the combined system demonstrate the ability to acquire images of the ciliary muscle with this design (Figure 5.11) (Ruggeri et al, to be submitted Biomedical Optics Express).

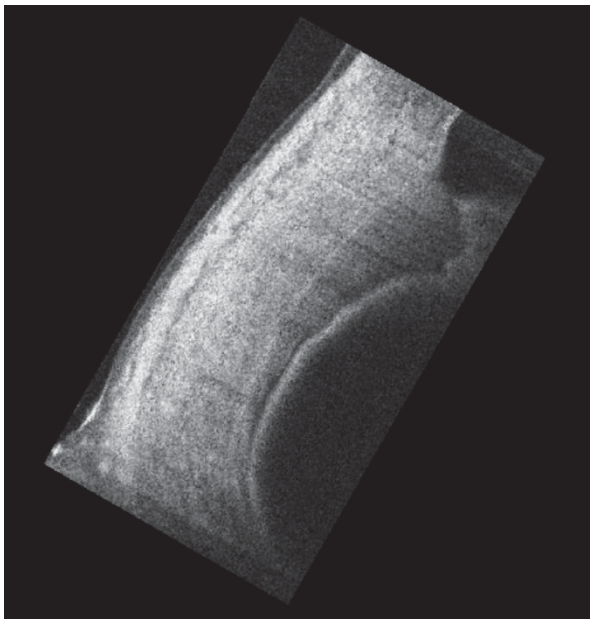

Figure 5.11: Image of the ciliary body acquired with the trans-scleral SD-OCT probe.

5.4.3 Final Integrated System

Figures 5.12 and 5.13 show the final integrated system. The entire system was mounted on a motorized slit-lamp table which allows for 3-dimensional adjustment of the system's position. The subject places his/her head on the chin rest which can be adjusted up or down as a rough alignment of the eye relative to the objective lens of the wavefront sensor and accommodation stimulus modules. The only other component located on the motorized table is the SLD light source used as the wavefront sensor probe beam. All other components, including the digital I/O interface for synchronization and both OCT engines and their respective PCs reside on two medical-grade transport carts.

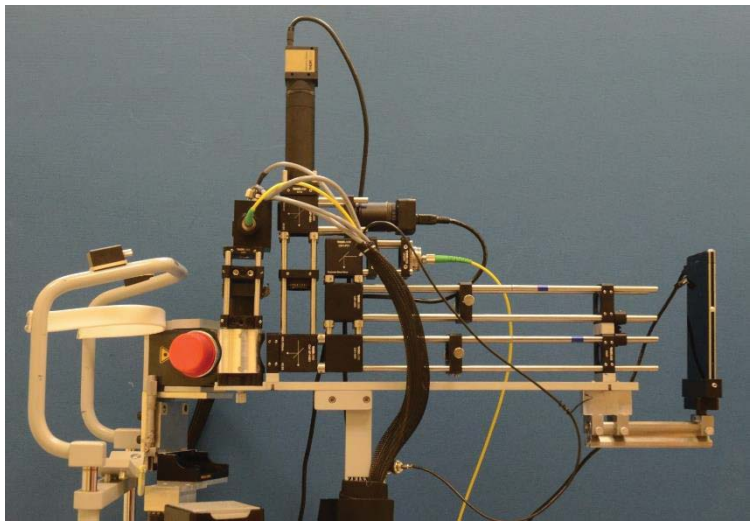

Figure 5.12: A side view of the complete system. The patient's head is placed on the chinrest to the left of the picture.

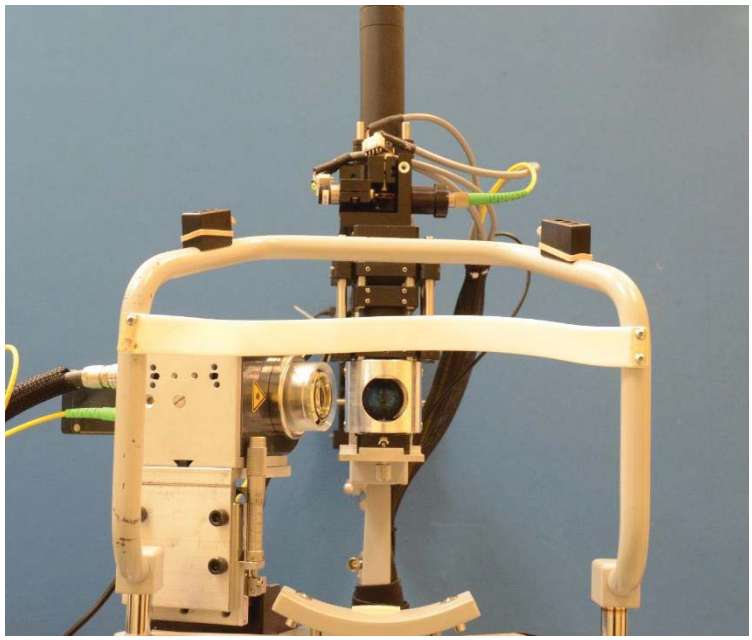

Figure 5.13: Front view of the integrated system. The position of the extended-depth SD-OCT probe is adjusted to bring the eye in focus. The entire system is mounted on the same base, so that the position of both OCT systems changes when the extended-depth OCT system position is adjusted.

5.5 Device Synchronization

Synchronization of the two OCT systems and wavefront aberrometer signals was performed using custom LabVIEW software and a USB-6211 multifunction I/O interface (National Instruments, Austin, Texas). Synchronization of the OCT systems to one another

was performed by Marco Ruggeri and Carolina de Freitas and has been described in detail elsewhere (de Freitas, 2014). To synchronize the acquisition of the refraction data and pupil image, the synchronization signals from the OCT systems and the accommodation stimulus were probed using the I/O interface. The rising edge of the start OCT acquisition signal and the falling edge of the stimulus switch signal were used as indicators to the software that data collection should begin or that an accommodation trigger had taken place. The sequence of events during a complete single run of the LabVIEW software can be described as follows:

- The "Start" button in the software is pressed and free-run mode of the autorefractor and alignment camera is activated. No measurements are recorded during this time.
- Free-run of the OCT modules is initiated in their respective original software.
- Once the OCT systems are in free-run, a "Record" button is pressed in the LabVIEW software initiating the digital probe of the I/O interface to detect the rising edge of the OCT start acquisition signal.
- The "Acquire" button is pressed on the extended-depth SD-OCT system, triggering the rising edge, which starts acquisition of the wavefront data from the aberrometer. Data collected prior to application of the stimulus is tagged with a Boolean false in the text file as a means to denote pre- and post- stimulus data.
- Once the stimulus is triggered, the falling edge signal is detected, changing the position of the target and now tagging the wavefront data with a Boolean true.
- The collection of data from the OCT and wavefront sensor is timed out once a predefined amount of time has elapsed. Once acquisition ends, all depressed buttons are automatically returned to the OFF state and another measurement can be taken.

Since acquisition of wavefront data and OCT images occur at different rate, the start of acquisition and the application of the stimulus are used as reference markers to synchronize the data during post-processing.

5.6 Coincident Imaging and Measurement of Accommodation

5.6.1 Purpose

The goal of the study is to verify the capability of the combined autorefractor, anterior segment OCT and accommodation stimulus system to measure the optical and geometric changes to the crystalline lens during accommodation.

5.6.2 Methods

Measurements were taken on the left eye of 3 subjects, following an IRB-approved protocol. All measurements were done with the subjects in an uncorrected, non-cyclopleged state. Subjects were asked to fixate on the far channel stimulus and occlude the contralateral eye with their hand. The auxiliary lens of the far target was adjusted until the subject stated that the target was in focus, to place the far target channel stimulus at their far point.

The custom LabVIEW software was then run to collect wavefront data and trigger the acquisition of OCT data from the extended-depth SD-OCT system. The sequence of data acquisition is described in Section 5.5. The wavefront sensor provides wavefront data at a rate of 5 Hz and the OCT records data at a rate of 15 Hz, with a total of 40 data points acquired from the wavefront sensor and 50 data points acquired from the OCT per measurement run. When the OCT is triggered to start acquisition, there is a one second delay in the application of the stimulus. Two seconds of ocular wavefront data and one second of OCT data has been collected by the time the stimulus is triggered. Once

triggered, 2.5 seconds and 6 seconds worth of OCT data and ocular wavefront data are collected, respectively.

Data was acquired for three accommodation stimuli, once for each stimulus; from 0 to 2 D, 0 to 4 D, and 0 to 6 D. Measurements were retaken if the eye movements caused a pupil shift out of the range of the probe beam. Calculations of crystalline lens power were performed using the method described in Chapter 4. Segmentation of the OCT images to provide values of ocular distances along the central A-line is performed using custom algorithm developed by Siobhan Williams at the Ophthalmic Biophysics Center. The application of the stimulus is time-stamped. All data points acquired before the time-stamp are considered to be measuring the subject's relaxed wavefront and axial biometry. The average value of these 10 points in ocular wavefront data and 15 in segmented OCT data is taken to represent the relaxed state. When the stimulus is presented, refraction and axial biometry change until they reach the final accommodated steady state. The averaged values of the last points of the recording were used as the value of the refractive state and axial biometry of the subject in the accommodated state. The point at which the accommodated steady state is set to begin was chosen empirically by evaluating its onset on the plots of the change in lens thickness and the sphere component of refraction with accommodation, and therefore varies between subjects and stimuli applied. Since corneal thickness does not change during accommodation, the value of corneal thickness used in the lens power calculation is the average across all measured central thickness values from the three datasets obtained for each subject.

5.6.3 Results

The values measured in the 3 eyes are summarized in Table 5.1 and Table 5.2. These values were used to calculate lens power in the accommodated and disaccommodated states by utilizing the method described in Chapter 4 (Table 5.3). Figures 5.14, 16, and 18 show plots of change in measured sphere, cylinder, and axis during stimulated accommodation. Figures 5.15, 17, and 19 show the change in lens thickness during stimulated accommodation. Figure 5.20 shows the change in lens power as a function of the stimulus applied. The lens thickness increases during accommodation, and the anterior chamber depth and vitreous depth decrease.

The response of the 24 year old subject was variable, particularly at the 2D stimulus. The large fluctuations in sphere and cylinder and in lens thickness measured in response to the 2 D stimulus indicate that there were significant eye movements or decentration during the measurement, or that the subject could not maintain the near target in focus. For the other two subjects, the change in lens thickness and refraction to the step-wise accommodation stimulus was observed to follow an exponential type-behavior. For these two subjects there is an increase in lens power as the accommodative demand is increased (Figure 5.20). Figure 5.21 shows the relationship between the change in lens thickness and the calculated change in lens power. Applying a linear regression gives a change in lens power of the 27, and 22 year old of 0.032 and 0.008 mm/D, respectively. The value of the thickness-power slope for the 27 year old is within the range of values found by Dubbelman et al (2005) using Scheimpflug imaging. The value obtained for the 22 year old is much lower, most likely due to errors in the refraction measurement in response to the 6 D stimulus. Table 5.2 shows that the measured baseline sphere and

cylinder for the 6 D stimulus was significantly different from the values obtained during the experiments with the 2 D and 4 D stimuli. In addition, Figure 5.18 shows that both sphere and cylinder values measured for this subject in response to the 6 D stimulus were more variable. These results suggest that eye movements or misalignment may have affected the measurements.

Table 5.1: Measured axial biometry results from 3 subjects. R_1 and R_2 are the mean anterior and posterior radius of curvature of the cornea, respectively. CCT: Central corneal thickness. ACD: Anterior chamber depth. LT: Lens thickness. VD: Vitreous depth.

					Accommodation Calculation Distances (mm)							Steady State Average Difference		
Subject	SEQ, R (D)	R_1 (mm)	R_2 (mm)		CCT Avg. (mm)	ACD @ 0	ACD @ Accom.	LT @ 0	LT @ Accom.	VD @ 0	VD @ Accom.	ΔACD	ΔLT	ΔVD
27 y/o	-2.19	7.47	5.94	2 D	0.536	2.989	2.792	3.518	3.725	16.801	16.750	-0.197	0.207	-0.051
				4 D	0.558	2.919	2.716	3.538	3.825	16.823	16.747	-0.203	0.287	-0.076
				6 D	0.561	2.971	2.817	3.535	3.871	16.780	16.598	-0.154	0.335	-0.183
24 y/o	1.20	7.59	6.11	2 D	0.607	2.591	2.527	3.818	3.871	15.056	15.010	-0.064	0.054	-0.046
				4 D	0.590	2.601	2.470	3.855	4.037	14.945	14.887	-0.131	0.182	-0.057
				6 D	0.594	2.525	2.451	3.949	4.086	14.915	14.854	-0.075	0.137	-0.060
22 y/o	-4.92	7.81	6.47	2 D	0.555	3.679	3.545	3.398	3.560	18.326	18.310	-0.134	0.162	-0.016
				4 D	0.564	3.673	3.512	3.444	3.641	18.298	18.306	-0.161	0.196	0.008
				6 D	0.569	3.627	3.491	3.452	3.680	18.323	18.260	-0.137	0.229	-0.063

Table 5.2: Measured wavefront results from 3 subjects. Values of refraction to the left on the table were measured using a commercial autorefractor. Changes in cylinder and axis were calculated from simple subtraction.

					Measured Sphere (D)		Measured Cylinder (D)		Measured Axis (deg)		Steady State Average Difference		
Subject	Sphere (D)	Cylinder (D)	Axis (deg.)		Unaccom.	Accom.	Unaccom.	Accom.	Unaccom.	Accom.	Δ Sphere	Δ Cylinder	Δ Axis
				2 D	-2.91	-5.47	-1.10	-1.08	41.73	55.11	2.56	0.02	13.38
27 y/o	-2.54	0.71	15	4 D	-3.90	-7.41	-0.66	-1.26	32.43	6.35	3.51	0.60	26.08
				6 D	-3.68	-8.84	-1.03	-0.90	56.25	37.46	5.30	0.13	18.78
				2 D	0.23	-4.90	-1.88	-4.96	92.61	91.02	5.12	3.08	1.59
24 y/o	1.08	0.25	76	4 D	-0.78	-4.97	-0.35	-1.37	114.48	67.77	4.19	1.02	46.71
				6 D	-1.49	-5.27	-0.65	-1.00	145.4	69.61	3.78	0.36	75.80
				2 D	-5.42	-7.02	-0.17	-0.67	71.98	64.52	1.61	0.51	7.45
22 y/o	-5.08	0.33	5	4 D	-5.43	-8.95	-0.3	-0.52	99.31	108.85	3.52	0.22	9.55
				6 D	-2.58	-9.97	-1.46	-0.94	62.14	127.28	7.38	0.51	65.15

Table 5.3: Calculated values used in the equations for lens power.

Subject	K (D)	K_2 (D)	H_1V_1 (mm)		M_L @ 0	M_L @ Accom.	b @ 0	b @ Accom.	L @ 0 (D)	L @ Accom. (D)	ΔL (D)
				2 D	0.663	0.615	0.702	0.690	24.72	28.45	3.73
27 y/o	43.74	-6.73	0.062	4 D	0.644	0.580	0.697	0.684	26.25	31.16	4.91
				6 D	0.648	0.553	0.698	0.679	26.01	33.51	7.50
				2 D	0.645	0.556	0.697	0.680	28.74	36.34	7.60
24 y/o	43.13	-6.55	0.066	4 D	0.625	0.554	0.692	0.679	30.79	36.80	6.01
				6 D	0.616	0.549	0.690	0.678	31.52	37.29	5.77
				2 D	0.645	0.613	0.697	0.690	24.16	26.37	2.21
22 y/o	42.08	-6.18	0.060	4 D	0.645	0.575	0.697	0.683	24.26	29.08	4.82
				6 D	0.704	0.554	0.715	0.679	20.01	30.61	10.59

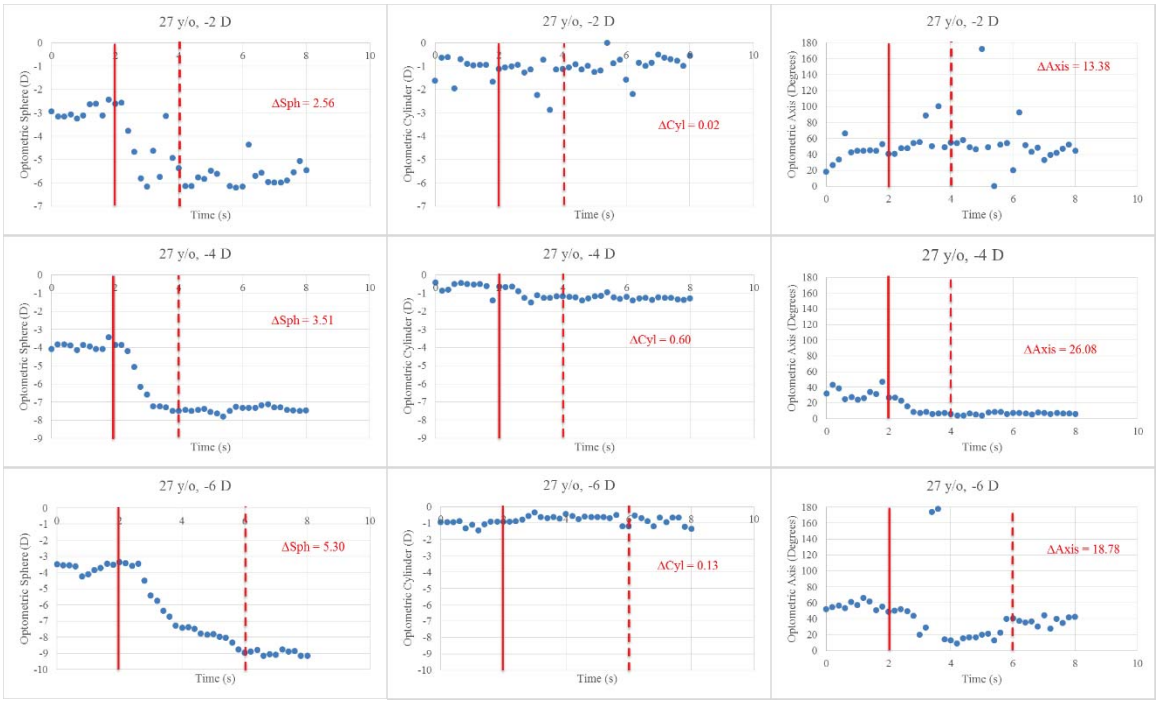

Figure 5.14: Measured change in wavefront sphere, cylinder, and axis during stimulated accommodation in a 27 year old subject. The solid red line marks the time at which the stimulus was applied and the dashed red line marks the selected start of the accommodated steady state.

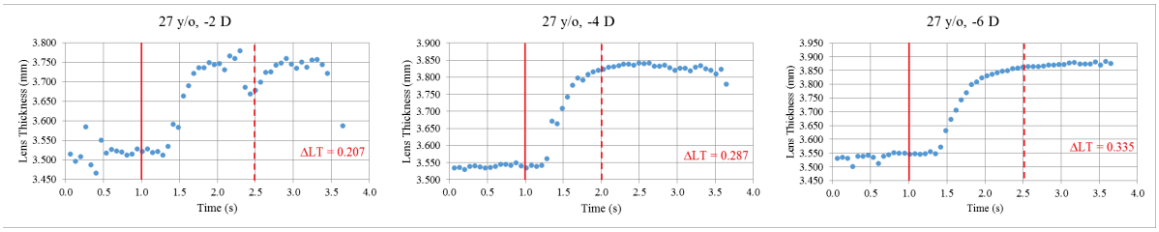

Figure 5.15: Measured change in lens thickness during stimulated accommodation in a 27 year old subject. The solid red line marks the time at which the stimulus was applied and the dashed red line marks the selected start of the accommodated steady state.

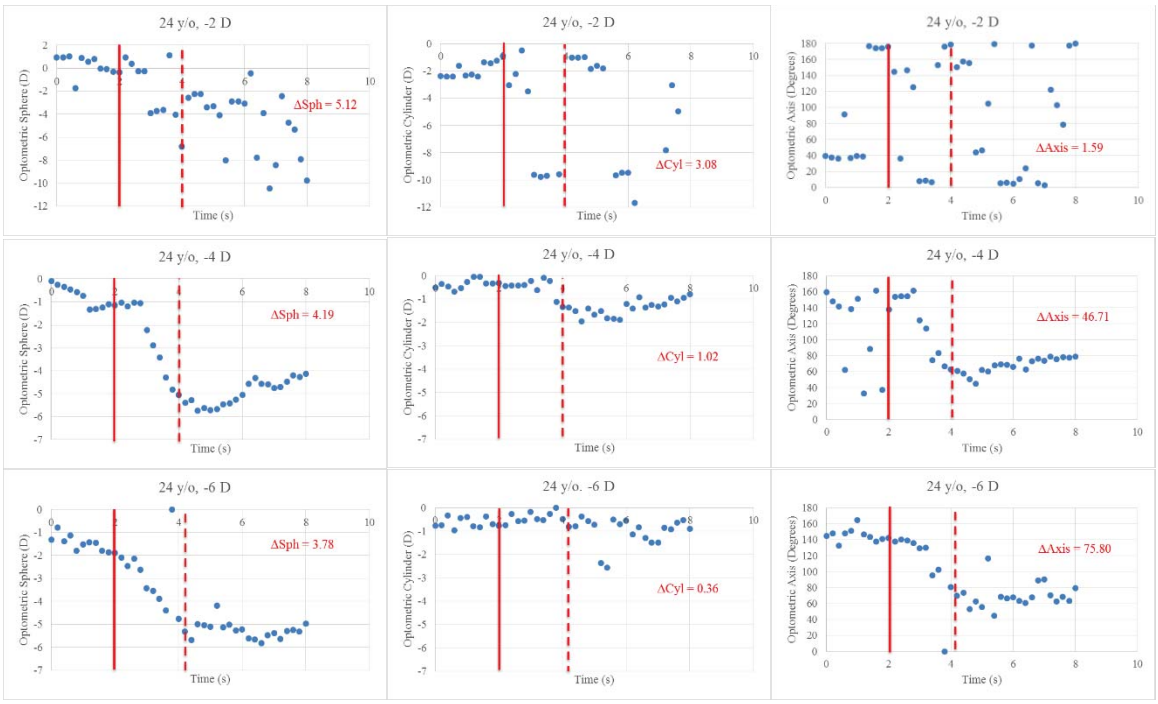

Figure 5.16: Measured change in wavefront sphere, cylinder, and axis during stimulated accommodation in a 24 year old subject. The solid red line marks the time at which the stimulus was applied and the dashed red line marks the selected start of the accommodated steady state.

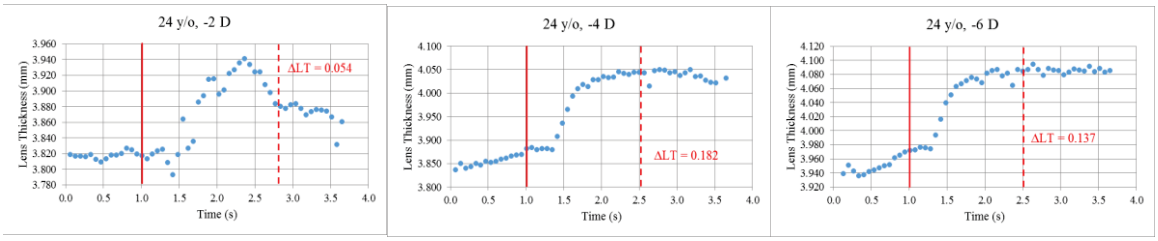

Figure 5.17: Measured change in lens thickness during stimulated accommodation in a 24 year old subject. The solid red line marks the time at which the stimulus was applied and the dashed red line marks the selected start of the accommodated steady state.

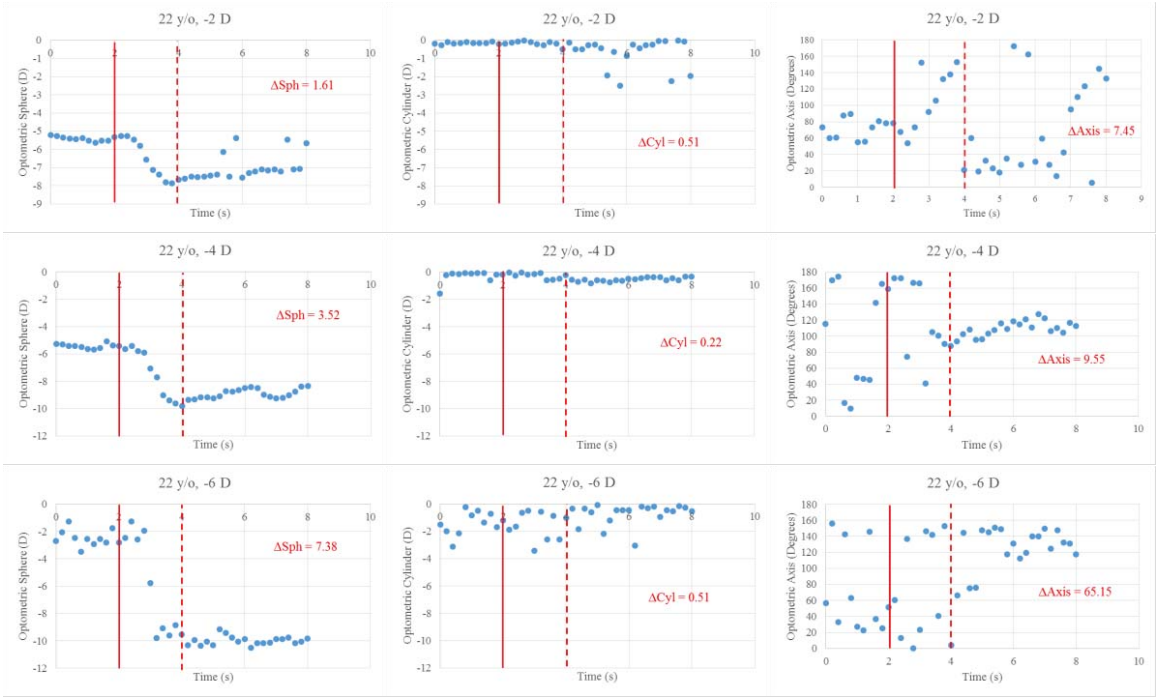

Figure 5.18: Measured change in wavefront sphere, cylinder, and axis during stimulated accommodation in a 22 year old subject. The solid red line marks the time at which the stimulus was applied and the dashed red line marks the selected start of the accommodated steady state.

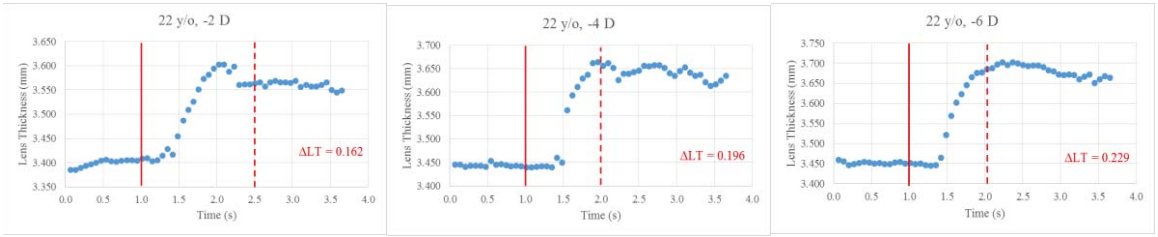

Figure 5.19: Measured change in lens thickness during stimulated accommodation in a 22 year old subject. The solid red line marks the time at which the stimulus was applied and the dashed red line marks the selected start of the accommodated steady state.

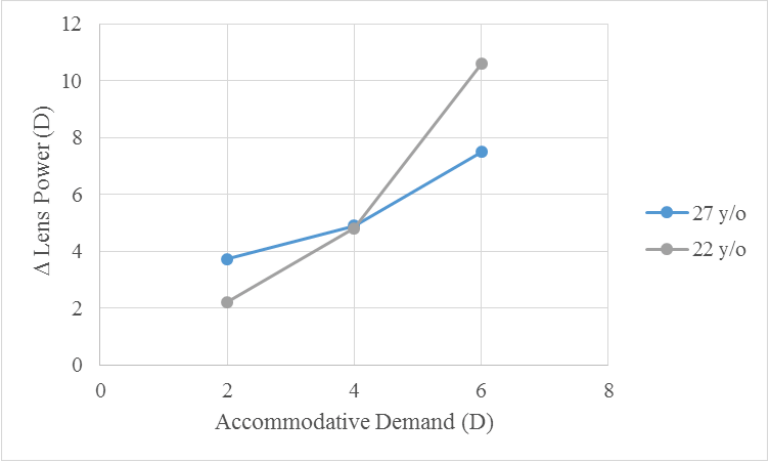

Figure 5.20: Change in lens power vs. accommodative demand for the 22 and 27 year old subjects.

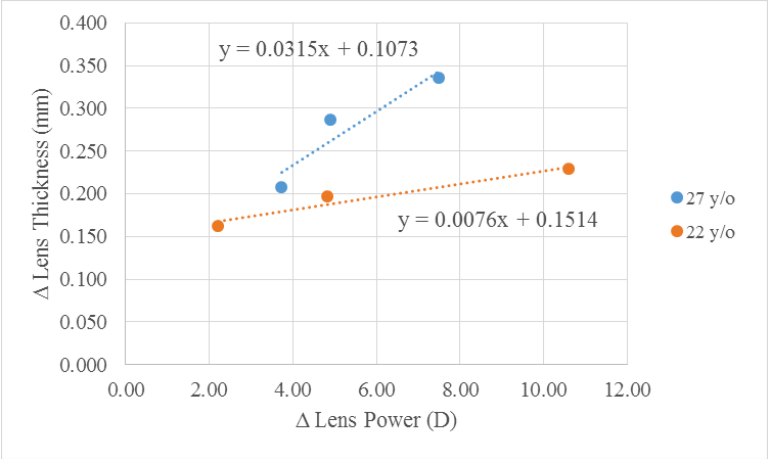

Figure 5.21: Change in lens thickness vs. change in lens power for the 22 and 27 year old subjects.

5.7 Discussion

In this Chapter, we present the integration of the autorefractor and accommodation target described in Chapter 3 with two OCT systems into a biometry system designed to simultaneously acquire refraction and biometry data during accommodation. Proof-of-principle experiments on three human subjects demonstrate the basic feasibility of combined refraction and ocular biometry in response to step accommodation stimuli. The results are in agreement with previously published data on the measured response to an accommodative stimulus (Sheppard et al, 2011) and with the accepted theory of

accommodative behavior (von Helmholtz, 1855). As with the experiments described in Chapter 3, raw data collected during each run is displayed and used in calculation of the steady state averages.

The experiments helped us identify a few limitations to the present technique. First, the subjects were found to have difficulty in finding the near target following the step stimulus, especially for the large stimuli (4 D and 6 D). This may have caused misalignment or decentration of the eye, and may explain some of the fluctuations in the refraction and biometric data. The spatial frequency content of the target may need to be optimized to facilitate the response to the step stimulus. Alternatively, the step stimulus may not be the ideal type of stimulus. A ramp stimulus may be a better alternative. In addition, as discussed in Chapter 3, the use of a red beam for refraction measurements made it more difficult for the subject to maintain fixation on the target. Pupil constriction is another factor that may have affected the refraction measurements, particularly for the 22 year old subject during the response to the 6 D stimulus. The view from the pupil camera and from the anterior segment OCT image indicates that the pupil diameter decreased significantly, potentially below the 3 mm fixed pupil defined by the software. Pupil constriction below 3mm will introduce measurement errors in the wavefront. The addition of pupillometry will be important to help increase the accuracy of the measurements.

With regards to the post-processing of the data collected, the fluctuations of refraction and lens thickness measurements introduced uncertainty in the selection of the onset of the accommodated steady state. The average of the accommodated steady state is taken from a point where the measurement appears to stabilize. In some of the responses,

the recording time window was not large enough to allow the subject to reach a true steady state (See for instance the response to the 6 D stimulus in Figure 5.19).

The following modifications to the integrated ocular refraction and biometry system, in addition to those detained in Chapter 3, would improve functionality:

- Change of the OCT probe delivery dichroic mirror to allow for the transmission of the longer wavelength wavefront aberrometer probe beam.
- Replacement of the accommodation stimulus source to a display that is easier to adjust and control.
- Modification to the trans-scleral SD-OCT mounting base to allow measurement of both left and right eye temporal ciliary body.
- The addition of pupillometry to evaluate the change in pupil diameter as a function of accommodative demand.

5.8 Conclusion

The autorefractor and accommodation system described in Chapter 3 was combined with an extended-depth SD-OCT system and trans-scleral SD-OCT system to simultaneously measure the optical and geometric changes of the eye during stimulated accommodation. The feasibility to acquire simultaneous refraction and biometric data dynamically during accommodation was demonstrated in a proof-of-principle study on three subjects. The method for the calculation of lens power described in Chapter 4 was applied to the collected data to determine the relationship between the change in lens power and lens thickness during accommodation. The experiments performed in Chapter 5 serve as a preliminary design verification of the accommodation biometry system's capability for objective assessment of accommodation.

Chapter 6: Summary and Conclusion

Accommodation is the ability of the eye to change focus. Presbyopia is the age-related loss of near visual function due to the gradual loss of the ability of the crystalline lens to change shape. It is a condition that affects everyone, beginning between the ages of 40-45. This gradual loss of near visual ability can make routine near tasks more difficult to perform. There are many new treatments for presbyopia in development, a need established by the continual growth of the presbyopic population. In order to assess the effectiveness of potential treatments designed to restore accommodation, an objective method of measuring accommodative response before and after treatment must be developed.

The goal of this project was to develop and evaluate a system that simultaneously measures the objective optical and mechanical accommodative response of the eye. The objective was to produce a device that can be used to qualitatively and quantitatively understand the changes that occur during accommodation and their age-dependence. This technology will allow for objective assessment of potential new surgical presbyopia treatments and verification of post-surgical results.

The goal of Aim 1 was the design, build, and testing of a system that combines a Shack-Hartmann based autorefractor with a dual-channel modified Badal optometer. The wavefront aberrometer and accommodation stimulus allow for real-time measurement of the refractive change during accommodation. The development of an autorefractor capable of measuring dynamic refraction in real-time was necessary to quantify the optical changes of the eye during stimulated accommodation. The proof of principle of these two modules was demonstrated in a preliminary study on 3 pre-presbyopic subjects. These studies showed that the autorefractor provided repeatable real-time measurements of the optical changes in the eye during accommodation.

Aim 2 involved developing a method for measuring lens power from whole eye OCT biometry, corneal topography, and refraction using a modified version of the Bennett method. The method will be used as an alternative to phakometry for measurements of changes in lens power during accommodation. A reduced eye model was used to derive a formula for lens power in terms of ocular distances, corneal power, and objective spherical equivalent refraction. The formula was used to calculate lens power in 16 eyes of 8 human subjects. Mean lens power measured was 24.2 D +/-1.8 D. An error analysis shows that the method produces lens power values with a predicted uncertainty of ±0.5 D.

The purpose of Aim 3 was to integrate an extended depth anterior segment spectral domain optical coherence tomography (SD-OCT) system and a trans-scleral SD-OCT system with the autorefractor and accommodation target described in Chapter 3. The complete system was used to record the optical and biometric changes to the eye during stimulated accommodation in 3 pre-presbyopic subjects. These changes were then correlated to the change in lens power using the method developed in Aim 2.

This dissertation serves as a design verification for a proof of concept device capable of objective accommodation assessment. The combined system was shown to be capable of simultaneous acquisition of optical and biometric information. Preliminary data collected is in agreement with previously published data correlating change in biometry to lens power change. The inclusion of a trans-scleral ciliary body imaging system allows for a complete evaluation of the accommodative plant.

The following modifications to the combined system would improve overall functionality and form part of planned future project activities:

- Extension of the autorefractor probe beam to longer wavelengths to avoid visualization of the beam during measurements.
- Increase in the wavefront sampling frequency of the wavefront sensor to allow acquisition of the dynamic refraction at rates matching the frame rate of the OCT system.
- Automatic artifact registration and filtering of recorded wavefront data to improve the reliability of measurements.
- Change of the OCT probe delivery dichroic mirror to allow for the transmission of the longer wavelength wavefront aberrometer probe beam.
- Replacement of the accommodation stimulus source to a display that is easier to adjust and control.
- Modification to the trans-scleral SD-OCT mounting base to allow measurement of both left and right eye temporal ciliary body.
- The addition of pupillometry to evaluate the change in pupil diameter as a function of accommodative demand.

The device will provide an integrated platform for the study of accommodation, presbyopia, and the evaluation of techniques under development to restore accommodation.

REFERENCES

Abdelkader A. Improved presbyopic vision with miotics. *Eye & Contact Lens* 0:1-5; 2015

Alfonso JF, Fernandez-Vega L, Baamonde MB, Montes-Mico R. Prospective visual evaluation of apodized diffractive intraocular lenses. *Journal of Cataract and Refractive Surgery* 33:1235-1243; 2007

Alio JL, 2012; Plaza-Puche AB, Montalban R, Javaloy J. Visual outcomes with a single-optic accommodating intraocular lens and a low-addition-power rotational asymmetric multifocal intraocular lens. *Journal of Cataract and Refractive Surgery* 38:978-985; 2012

Alio JL, Ben-num J, Rodriquez-Prats JL, Plaza AB. Visual and accommodative outcomes 1 year after implantation of an accommodating intraocular lens based on a new concept. *Journal of Cataract and Refractive Surgery* 35:1671-1678; 2009

Anderson HA, Glasser A, Manny RE, Stuebing KK. Age-related changes in accommodative dynamics from preschool to adulthood. *Investigative Ophthalmology and Visual Science* 51(1):614-622; 2010

Atchison D, Bradley A, Thibos L, Smith G. Useful variations of the Badal Optometer. *Optometry and Vision Science* 72(4):279-284; 1995

Augusteyn RC. On the growth and internal structure of the human lens. *Experimental Eye Research* 90:643-654; 2010

Ben-nun J, Alio JL. Feasibility and development of a high-power real accommodating intraocular lens. *Journal of Cataract and Refractive Surgery* 31:1802-1808; 2005

Bennett AG. A method of determining the equivalent powers of the eye and its crystalline lens without resort to phakometry. *Ophthalmic Physiological Optics* 8:53-59; 1988

Bennett AG, Rabbetts RB. Clinical Visual Optics. *Butterworth-Heinemann* Oxford; 1998

Beverage JL, Schwiegerling J. A Shack-Hartmann-based autorefractor. *Journal of Refractive Surgery* 22:932-937; 2006

Bohorquez V, Alarcon R. Long-term reading performance in patients with bilateral dual-optic accommodating intraocular lenses. *Journal of Cataract and Refractive Surgery* 36:1880-1886; 2010

Borja D, Manns F, Ho A, Ziebarth N, Rosen AM, Jain R, Amelinckx A, Arrieta E, Augusteyn RC, Parel JM. Optical power of the isolated human crystalline lens. *Investigative Ophthalmology and Vision Science* 49(6):2541-2548; 2008

Borja D, Uhlhorn SR, Ziebarth NM, Nankivil D, Arrieta-Quintero E, Ehrmann K, Ho A, Manns F, Parel J-M. Scheimpflug camera system for cross-sectional imaging of the ex vivo crystalline lens during simulated accommodation. Abstract and Poster #7163-65. *Ophthalmic Technologies XIX Conference, SPIE Photonics West Meeting*, San Jose CA, January 26, 2009

Britto P, Salgado-Borges J, Neves H, Gonzalez-Meijome J, Monteiro M. Light-distortion analysis as a possible indicator of visual quality after refractive lens exchange with diffractive multifocal intraocular lenses. *Journal of Cataract and Refractive Surgery* 41:613-622; 2015

Brown N. The change in shape and internal form of the lens of the eye on accommodation. *Experimental Eye Research* 15:441-459; 1973

Burd HJ, Judge SJ, Flavell MJ. Mechanics of accommodation of the human eye. *Vision Research* 39:1591-1595; 1999

Charman WN, Atchison DA. Age-dependence of the average and equivalent refractive indices of the crystalline lens. *Biomedical Optics Express* 5(1):31-39; 2013.

Cheng X, Himebaugh NL, Kollbaum PS, Thibos LN, Bradley A. Validation of a clinical Shack-Hartmann aberrometer. *Optometry and Vision Science* 80(8):587-595; 2003

Cleary G, Spalton DL, Marshall J. Pilot study of new focus-shift accommodating intraocular lens. *Journal of Cataract and Refractive Surgery* 36:762-770, 2010

de Freitas C. Control unit for an optical switch to extend the axial range of a spectral-domain optical coherence tomography system. Biomedical Engineering. University of Miami, Coral Gables, FL; 2014

Doane JF, Jackson RT. Accommodative intraocular lenses: considerations on use, function, and design. *Current Opinion in Ophthalmology* 18:318-324; 2007

Du TT, Fan VC, Asbell PA. Conductive Keratoplasty. *Current Opinion in Ophthalmology* 18:334-337; 2007

Dubbelman M, Sicam VA, Van der Heijde GL. The shape of the anterior and posterior surface of the aging human cornea. *Vision Research* 46(6-7):993-1001; 2006

Dubbelman M, Van der Heijde GL. The shape of the aging human lens: curvature, equivalent refractive index and the lens paradox. *Vision Research* 41:1867-1877; 2001

Dubbelman M, Van der Heijde GL, Weeber HA. The thickness of the aging human lens obtained from corrected Scheimpflug images. *Optometry and Vision Science* 78(6):411-416; 2001

Dubbelman M, Van der Heijde GL, Weeber HA. Change in shape of the aging crystalline lens with accommodation. *Vision Research* 45:117-132; 2005

Dubbelman M, Van der Heijde R, Weeber HA, Vrensen GFJM. Changes in the internal structure of the human crystalline lens with age and accommodation. *Vision Research* 43:2363-2375; 2003

Dunne MCM, Barnes DA, Royston JM. An evaluation of Bennett's method for determining the equivalent powers of the eye and its crystalline lens without resort to phakometry. *Ophthalmic Physiological Optics* 9:69-71; 1989

Dunne MCM, Davies LN, Wolffsohn JS. Accuracy of cornea and lens biometry using anterior segment optical coherence tomography. *Journal of Biomedical Optics.* 12(6):06423, 1-5; 2007

Dunne MCM, Royston JM, Barnes DA. Normal variations of the posterior corneal surface. *Acta Ophthalmologica* 70(2):255-261; 1992

Epstein RL, Gurgos MA. Presbyopia treatment by monocular peripheral presbyLASIK. *Journal of Refractive Surgery* 25:516-523; 2009

Esquenazi S, He J, Kim DB, Bazan NG, Bui V, Bazan HE. Wound healing response and refractive regression after conductive keratoplasty. *Journal of Cataract and Refractive Surgery* 32(3):480-486; 2006

Farid M, Steinert RF. Patient selection for monovision laser refractive surgery. *Current opinion in Ophthalmology* 20:251-254; 2009

Fercher AF. Optical coherence tomography – development, principles, applications. *Zeitschrift fur Medizinische Physik* 20:251-276; 2009

Gabriel C, Klaproth OK, Titke C, Baumeister M, Buhren J, Kohnen T. Repeatability of topographic and aberrometric measurements at different accommodative states using a combined topographer and open-view aberrometer. *Journal of Cataract and Refractive Surgery* 41:806-811; 2015

Gallagher JT, Citek K. A Badal optical stimulator for the Canon Autoref R-1 optometer. *Optometry and Vision Science* 72(4):276-278; 1995

Gambra E, Ortiz S, Perez-Merino P, Gora M, Wojtkowski M, Marcos S. Static and dynamic crystalline lens accommodation evaluated using quantitative 3-D OCT. *Biomedical Optics Express* 4(9):1595-1609; 2013

Gambra E, Sawides L, Dorronsoro C, Marcos S. Accommodative lag and fluctuations when optical aberrations are manipulated. *Journal of Vision* 9(6)4:1-15; 2009

Garner LF. Calculation of the radii of curvature of the crystalline lens surfaces. *Ophthalmic Physiological Optics* 17(1):75-80; 1997

Glasser A. Restoration of accommodation: surgical options for correction of presbyopia. *Clinical and Experimental Optometry* 91(3):279-295; 2008

Glasser A, Campbell MCW. Presbyopia and the optical changes in the human crystalline lens with age. *Vision Research* 38:209-299; 1998

Grulkowski I, Gora M, Szkulmowski M, Gorczynska I, Szlag D, Marcos S, Kowalczyk A, Wojtkowski M. Anterior segment imaging with spectral OCT using a high-speed CMOS camera. *Optics Express* 17(6):4842-4858; 2009

Grulkowski I, Lin JJ, Potsaid B, Jayaraman V, Lu CD, Jiang J, Cable AE, Duker JS, Fujimoto JG. Retinal, anterior segment and full eye imaging using ultrahigh speed swept source OCT with vertical-cavity surface emitting lasers. *Biomedical Optics Express* 3(11):2733-2751; 2012

Haefliger E, Parel JM. Accommodation of an endocapsular silicone lens (Phaco-Ersatz) in the aging rhesus monkey. *Journal of Refractive and Corneal Surgery* 10(5):550-555; 1994

Haefliger E, Parel JM, Fantes F, Norton EW, Anderson DR, Forster RK, Hernandez E, Feuer WJ. Accommodation of an endocapsular silicone lens (Phaco-Ersatz) in the nonhuman primate. *Ophthalmology* 94(5):471-477; 1987

Hao X, Jeffery JL, Le TP, McFarland G, Johnson G, Mulder RJ, Garrett Q, Manns F, Nankivil D, Arrieta E, Ho A, Parel JM, Hughes TC. High refractive index polysiloxane as injectable, in situ curable accommodating intraocular lens. *Biomaterials* 33(23):5659-5671; 2012

Hennessy RT. Instrument Myopia. *Journal of the Optical Society of America* 65(10):1114-1120; 1975

Hernandez V, Delgado S, Borja D, Ho A, Manns F, Parel JM. Real-time Hartmann-Shack autorefractor: slit-lamp mounted prototype. Abstract and Presentation #8567-29. *Ophthalmic Technologies XXIII Conference, SPIE Photonics West Meeting*, San Francisco CA, February 3, 2013

Ho A, Erickson P, Manns F, Pham T, Parel JM. Theoretical analysis of accommodation amplitude and ametropia correction by varying refractive index in Phaco-Ersatz. *Optometry and Vision Science* 78:405-410; 2001

Ho A, Manns F, Pham T, Parel JM. Predicting the performance of accommodating intraocular lenses using ray tracing. *Journal of Cataract and Refractive Surgery* 32:129-136; 2006

Holden BA, Fricke TR, Ho SM, Wong R, Schlenther G, Cronje S, Burnett A, Papas E, Naidoo KS, Frick KD. Global vision impairment due to uncorrected presbyopia. *Archives of Ophthalmology* 126(12):1731-1739; 2008

Hunt OA, Wolffsohn JS, Gilmartin B. Evaluation of the measurement of refractive error by PowerRefractor: a remote, continuous and binocular measurement system of oculomotor function. *British Journal of Ophthalmology* 87:1504-1508; 2003

Iribarren R. Crystalline lens and refractive development. *Progress in Retinal and Eye Research* 47:86-106; 2015

Iribarren R, Morgan IG, Nangia V, Jonas JB. Crystalline lens power and refractive error. *Investigative Ophthalmology and Visual Science* 53(2):543-550; 2012

Izatt JA, Hee MR, Swanson EA, Lin CP, Huang D, Schuman JS, Puliafito CA, Fujimoto JG. Micrometer-scale resolution imaging of the anterior eye in vivo with optical coherence tomography. *Archives of Ophthalmology* 112:1584-1589; 1994

Jainta S, Jaschinski W, Hoormann J. Measurement of refractive error and accommodation with the photorefractor PowerRef II. *Ophthalmic and Physiological Optics* 24:520-527; 2004

Jenkins FA, White HE. Fundamentals of Optics. McGraw Hill Book Company, New York; 1957

Jones CE, Atchison DA, Pope JM. Changes in lens dimensions and refractive index with age and accommodation. *Optometry and Vision Science* 84(10):990-995; 2007

Jones LA, Mitchell GL, Mutti DO, Hayes JR, Moeschberger ML, Zadnik K. Comparison of ocular component growth curves among refractive error groups in children. *Investigative Ophthalmology and Visual Science* 46:2317-2327; 2005

Kasthurirangan S, Vilupuru AS, Glasser A. Amplitude dependent accommodative dynamics in humans. *Vision Research* 43(27):2945-56; 2003

Koopmans SA, Terwee T, Barkhof J, Haitjema HJ, Kooijman AC. Polymer refilling of presbyopic human lenses in vitro restores the ability to undergo accommodative changes. *Investigative Ophthalmology and Visual Science* 44(1):250-257; 2003

Koopmans SA, Terwee T, Glasser A, Wendt M, Vilipuru AS, van Kooten TG, Norrby S, Haitjema HJ, Kooijman AC. Accommodative lens refilling in rhesus monkeys. *Investigative Ophthalmology and Visual Science* 47(7):2976-2984; 2006

Koretz JF, Cook CA, Kaufman PL. Accommodation and presbyopia in the human eye: Changes in the anterior segment and crystalline lens with focus. *Investigative Ophthalmology and Visual Science* 38(3):569-578; 1997

Koretz JF, Cook CA, Kaufman PL. Aging of the human lens: Changes in lens shape at zero-diopter accommodation. *Journal of the Optical Society of America A* 18:265-272; 2001

Koretz JF, Cook CA, Kaufman PL. Aging of the human lens: changes in lens shape upon accommodation and with accommodative loss. *Journal of the Optical Society of America A* 19(1):144-151; 2002

Koretz JF, Cook CA, Kuszak JR. The zones of discontinuity in the human lens: Development and distribution with age. *Vision Research* 34:2955-2962; 1994

Koretz JF, Strenk SA, Strenk LM, Semmlow JL. Scheimpflug and high-resolution magnetic resonance imaging of the anterior segment: a comparative study. *Journal of the Optical Society of America. A* 21(3):346-354; 2004

Koretz JF, Handelman GH, Brown NP. Analysis of human crystalline lens curvature as a function of accommodative state and age. *Vision Research* 24(10):1141-1151; 1984

Krueger RR, Kuszak J, Lubatschowski H, Myers RI, Ripken T, Heisterkamp A. First safety study of femtosecond laser photodisruption in animal lenses: Tissue morphology and cataractogenesis. *Journal of Cataract and Refractive Surgery* 31:2386-2394; 2005

Lazon de la Jara P, Erickson D, Erickson P, Stapleton F. Visual and non-visual factors associated with patient satisfaction and quality of life in LASIK. *Eye* 25:1194-1201; 2011

Li SM, Wang N, Zhou Y, Li SY, Kang MT, Liu LR, Li H, Sun YY, Meng B, Zhan SY, Atchison DA. Paraxial schematic eye models for 7- and 14-year-old Chinese children. *Investigative Ophthalmology and Vision Science* 56(6):3577-3583; 2015

Li YJ, Choi JA, Kim H, Yu SY, Joo CK. Changes in ocular wavefront aberrations and retinal image quality with objective accommodation. *Journal of Cataract and Refractive Surgery* 37:835-841; 2011

Liang J, Grimm B, Goelz S, Bille JF. Objective measurement of wave aberrations of the human eye with the use of a Hartmann-Shack wave-front sensor. *Journal of the Optical Society of America. A* 11(7):1949-1957; 1994

Lin H, Jiang B. Accommodative responses under different stimulus conditions. *Optometry and Vision Science* 90(12):1406-1412; 2013

Lopez-Miguel A, Maldonado MJ, Belzunce A, Barrio-Barrio J, Coco-Martin MB, Nieto JC. Precision of a commercial Hartmann-Shack aberrometer: Limits of total wavefront laser vision correction. *American Journal of Ophthalmology* 154(5):799-807; 2012

Lossing LA, Sinnott LT, Kao CY, Richdale K, Bailey MD. Measuring changes in ciliary muscle thickness with accommodation in young adults. *Optometry and Vision Science* 89(5):719-726; 2012

Lubatschowski H, Schumacher S, Fromm M, Wegener A, Hoffmann H, Oberheide U, Gerten G. Femtosecond lentotomy: generating gliding planes inside the crystalline lens to regain accommodation ability. *Journal of Biophotonics* 3(5-6):265-268; 2010

Manns F, Ho A, Kruger RR. Customized visual correction of presbyopia. In Wavefront-guided corrections: The quest for super vision, 2nd Edition, Chapter 42. SLACK Inc, Thorofare, NJ 353-360; 2004

Marcos S, Ortiz S, Perez-Merino P, Birkenfeld J, Duran S, Jimenez-Alfaro I. Three-dimensional evaluation of accommodating intraocular lens shift and alignment in vivo. *Ophthalmology* 121:45-55; 2014

Marques EF, Castanheira-Dinis A. Clinical performance of a new aspheric dual-optic accommodating intraocular lens. *Clinical Ophthalmology* 8:2289-2295; 2014

Mastropasqua R, Pedrotti E, Passilongo M, Parisi G, Marchesoni I, Marchini G. Long-term visual function and patient satisfaction after bilateral implantation and combination of two similar multifocal IOLs. *Journal of Refractive Surgery* 31(5):308-314; 2015

Mathews S. Scleral expansion does not restore accommodation in human presbyopia. *Ophthalmology* 106(5):873-877; 1999

McLead SD, Portney V, Ting A. A dual optic accommodating foldable intraocular lens. *British Journal of Ophthalmology* 87:1083-1085; 2003

Mirshahi A, Buhran J, Gerhardt D, Kohnen T. In vivo and in vitro repeatability of Hartmann-Shack aberrometry. *Journal of Cataract and Refractive Surgery* 29:2295-2301; 2003

Montes-Mico R, Alio JL. Distance and near contrast sensitivity function after multifocal intraocular lens implantation. *Journal of Cataract and Refractive Surgery* 29:703-711; 2003

Montes-Mico R, Lopez-Gil N, Perez-Vives C, Bonaque S, Ferrer-Blasco T. In vitro optical performance of nonrotational symmetric and refractive-diffractive aspheric multifocal intraocular lenses: Impact of tilt and decentration. *Journal of Cataract and Refractive Surgery* 38:1657-1663; 2012

Mutti DO, Zadnik K, Adams AJ. A video technique for phakometry of the human crystalline lens. *Investigative Ophthalmology and Vision Science* 33(5):1771-1782; 1992

Mutti DO, Zadnik K, Adams AJ. The equivalent refractive index of the crystalline lens in childhood. *Vision Research* 35(11):1565-1573; 1995

Mutti DO, Mitchell GL, Jones LA, Friendman NE, Frane SL, Lin WK, Moeschberger ML, Zadnik K. Axial growth and changes in lenticular and corneal power during emmetropization in infants. *Investigative Ophthalmology and Vision Science* 49(9):3074-3080; 2005

Myers RI, Krueger RR. Novel approaches to correction of presbyopia with laser modification of the crystalline lens. *Journal of Refractive Surgery* 14(2):136-139; 1998

Neri A, Ruggeri M, Protti A, Leaci R, Gandolfi SA, Macaluso C. Dynamic imaging of accommodation by swept-source anterior segment optical coherence tomography. *Journal of Cataract and Refractive Surgery* 41:501-510; 2014

Olsen T, Amarsson A, Sasaki H, Sasaki K, Jonasson F. On the ocular refractive components: the Reykjavik eye study. *Acta Ophthalmologica Scandinavica* 85:361-366; 2007

Ortiz S, Perez-Merino P, Duran S, Velasco-Ocana M, Birkenfeld J, de Castro A, Jimenez-Alfaro I, Marcos S. Full OCT anterior segment biometry: an application in cataract surgery. *Biomedical Optics Express* 4(3):387-396; 2013

Ortiz S, Perez-Merino P, Gambra E, de Castro A, Marcos S. In vivo human crystalline lens topography. *Biomedical Optics Express* 3(10):2471-2488; 2012

Ortiz S, Siedlecki D, Grulkowski I, Remon L, Pascual D, Wojtkowski M, Marcos S. Optical distortion correction in optical coherence tomography for quantitative ocular anterior segment by three-dimensional imaging. *Optical Express* 18:2782-2796; 2010

Ossma IL, Galvis A, Vargas LG, Trager MJ, Vagefi MR, McLead SD. Synchrony dual-optic accommodating intraocular lens. *Journal of Cataract and Refractive Surgery* 33:47-52; 2007

Ostrin LA, Kasthurirangan S, Glasser A. Evaluation of a satisfied bilateral scleral expansion band patient. *Journal of Cataract and Refractive Surgery* 30:1445-1453; 2004

Panagopoulou S, Neal DR. Zonal matrix iterative method for wavefront reconstruction from gradient measurements. *Journal of Refractive Surgery* 21(S):S563-S569; 2005

Parel JM, Gelender H, Trefers WF, Norton EWD. Phaco Ersatz: cataract surgery designed to preserve accommodation. *Graefe's Archive for Clinical and Experimental Ophthalmology* 224:165-173; 1986

Pascolini D, Mariotti SP. Global estimates of visual impairment: 2010. *British Journal of Ophthalmology* 96: 614-618; 2012

Pieh S, Weghaupt H, Skorpik C. Contrast sensitivity and glare disability with diffractive and refractive multifocal intraocular lenses. *Journal of Cataract and Refractive Surgery* 24:659-662; 1998

Qazi MA, Pepose JS, Shuster JJ. Implantation of scleral expantion band segments for the treatment of presbyopia. *American Journal of Ophthalmology* 134(6):808-815; 2002

Queiros A, Villa-Collar C, Gutierrez AR, Jorge J, Gonzalez-Meijome JM. Quality of life of myopic subjects with different methods of visual correction using the NEI RQL-42 questionnaire. *Eye and Contact Lens* 38:116-121; 2012

Radhakrishnan S, Rollins AM, Roth JE, Yazdanfar S, Westphal V, Bardenstein DS, Izatt JA. Real-time optical coherence tomography of the anterior segment at 1310 nm. *Archives of Ophthalmology* 119(8):1179-1185; 2001

Ramasubramanian V, Glasser A. Can ultrasound biomicroscopy be used to predict accommodation accurately? *Journal of Refractive Surgery* 31(4):266-273; 2015

Ramasubramanian V, Glasser A. Prediction of accommodative optical response in presbyopic subjects using ultrasound biomicroscopy. *Journal of Cataract and Refractive Surgery* 41:964-980; 2015

Reggiani Mello GH, Krueger RR. Femtosecond laser photodisruption of the crystalline lens for restoring accommodation. *International Ophthalmology Clinics* 51(2):87-95; 2011

Richdale K, Bullimore MA, Zadnik K. Lens thickness with age and accommodation by optical coherence tomography. *Ophthalmic Physiology and Optics* 28:441-447; 2008

Rosales P, Marcos S. Phakometry and lens tilt and decentration using a custom-developed Purkinje imaging apparatus: validation and measurements. *Journal of the Optical Society of America A* 23(3):509-520; 2006

Rosen AM, Denham DB, Fernandez V, Borja D, Ho A, Manns F, Parel JM, Augusteyn RC. In vitro dimensions and curvatures of human lenses. *Vision Research* 46:1002-1009; 2006

Royston JM, Dunne MCM, Barnes DA. Calculation of crystalline lens radii without resort to phakometry. *Ophthalmic Physiological Optics* 9:412-414; 1989

Rozema JJ, Atchison DA, Tassignon MJ. Comparing methods to estimate the human lens power. *Investigative Ophthalmology and Visual Science* 52(11):7937-7942; 2011

Rozema JJ, Atchison DA, Kasthurirangan S, Pope JM, Tassignon MJ. Methods to estimate the size and shape of the unaccommodated crystalline lens in vivo. *Investigative Ophthalmology and Visual Science* 53(6):2533-2540; 2012

Ruggeri M, Uhlhorn SR, de Freitas C, Ho A, Manns F, Parel JM. Imaging and full-length biometry of the eye during accommodation using spectral domain OCT with an optical switch. *Biomedical Optics Express* 3(7):1506-1520; 2012

Ruggeri M, Uhlhorn S, De Freitas C, Manns F, Parel JM. Real-time imaging of accommodation using extended depth spectral domain OCT. ARVO Abstract; *Investigative Ophthalmology and Visual Science* 52: E-Abstract 3402; 2011

Ruggeri M, Uhlhorn S, Manns F, Parel JM, Porciatti V. Whole eye imaging of small animals with spectral-domain optical coherence tomography. Abstract and Presentation, *5th European Meeting on Visual and Physiological Optics*. August 22-24, 2010

Ruggeri M, Kocaoglu OP, Uhlhorn SR, Borja D, Urs R, Chou TH, Porciatti V, Parel JM, Manns F. Small animal ocular biometry using optical coherence tomography. Abstract and Presentation #7550-42. *Ophthalmic Technologies XX Conference, SPIE Photonics West Meeting*, San Francisco CA, January 23, 2010

Seyeddain O, Bachernegg A, Riha W, Ruckl T, Reitsamer H, Grabner G, Dexl AK. Femtosecond laser-assisted small-aperture corneal inlay implantation for corneal compensation of presbyopia: Two year follow-up. *Journal of Cataract and Refractive Surgery* 39:234-241; 2013

Shao Y, Tao A, Jiang H, Shen M, Zhong J, Lu F, Wang J. Simultaneous real-time imaging of the ocular anterior segment including the ciliary muscle during accommodation. *Biomedical Optics Express* 4(3):466-480; 2013

Sheppard AL, Davies LN. In vivo analysis of ciliary muscle morphologic changes with accommodation and axial ammetropia. *Investigative Ophthalmology and Visual Science* 51(12):6882-6889; 2010

Sheppard AL, Davies LN. The effect of aging on in vivo human ciliary muscle morphology and contractility. *Investigative Ophthalmology and Visual Science* 52(3):1809-1816; 2011

Sheppard AL, Evans CJ, Singh KD, Wolffsohn JS, Dunne MCM, Davies LN. Three-dimensional magnetic resonance imaging of the phakic crystalline lens during accommodation.

Shneor E, Millodor M, Avraham O, Amar S, Gordon-Shaag A. Clinical evaluation of the L80 autorefractometer. *Clinical and Experimental Optometry* 95(1):66-71; 2011

Soda M, Yaguchi S. Effect of decentration on the optical performance in multifocal intraocular lenses. *Ophthalmologica* 227:197-204; 2011

Spors F, Egan DJ, Shen J, McNaughton LE, Mann S, Patel NM. Corneal wavefront aberrations in patients wearing multifocal soft contact lenses for myopia control. *Open Journal of Ophthalmology* 2:45-53; 2012

Strang NC, Day M, Gray LS & Seidel D. Accommodation steps, target spatial frequency and refractive error. *Ophthalmic and Physiological Optics* 31(5):444-455; 2011

Teel DFW, Jacobs RJ, Copland J, Neal DR, Thibos LN. Differences between wavefront and subjective refraction for infrared light. *Optometry and Vision Science* 91(10):1158-1166; 2014

Torricelli AAM, Junior JB, Santhiago MR, Bechara SJ. Surgical management of presbyopia. *Clinical Ophthalmology* 6:1459-1466; 2012

Urs R, Ho A, Manns F, Parel JM. Age-dependent Fourier model of the shape of the isolated ex vivo human crystalline lens. *Vision Research* 50:1041-1047; 2010

Vilupuru SA, Lin L, Pepose JS. Comparison of contrast sensitivity and through focus in small-aperture inlay, accommodating intraocular lens, or multifocal intraocular lens subjects. *American Journal of Ophthalmology* 160(1):150-162; 2015

von Helmholtz H, Uber die akkommodation des auges. *Archives of Ophthalmology*. 2(2):1-74; 1855

Wang L, Wang N, Koch DD. Evaluation of refractive error measurements of the WaveScan wavefront system and the Tracey wavefront aberrometer. *Journal of Cataract and Refractive Surgery* 29:970-979; 2003

Waring IV GO, Berry DE. Advances in the surgical correction of presbyopia. International *Ophthalmology Clinics* 53(1):129-152; 2013

Wesemann W, Norcia AM, Allen D. Theory of eccentric photorefraction (photoretinoscopy): astigmatic eyes. *Journal of the Optical Society of America A* 8(12):2038-2047; 1991

Win-Hall DM, Glasser A. Objective accommodation measurements in presbyopic eyes using an autorefractor and an aberrometer. *Journal of Cataract and Refractive Surgery* 34(5):774-784; 2008

Win-Hall DM, Houser J, Glasser A. Static and dynamic measurement of accommodation using the Grand Seiko WAM-5500 autorefractor. *Optometry and Vision Science* 87(11):873-882; 2010

Win-Hall DM, Ostrin LA, Kasthurirangan S, Glasser A. Objective accommodation measurement with the Grand Seiko and Hartginer Coincidence Refractometer. *Optometry and Vision Science* 84(9):879-887; 2007

Wojtkowski M, Kowalczyk A, Leitgeb R, Fercher AF. Full range complex spectral optical coherence tomography technique in eye imaging. *Optics Letters* 27(16):1415-1417; 2002

Wolffsohn JS, O'Donnell C, Charman WN, Gilmartin B. Simultaneous continuous recording of accommodation and pupil size using the modified Shin-Nippon SRW-5000 autorefractor. *Ophthalmic and Physiological Optics* 24:142-147; 2004

Wolffsohn JS, Ukai K, Gilmartin B. Dynamic measurement of accommodation and pupil size using the portable Grand Seiko FR-5000 autorefractor. *Optometry and Vision Science* 83(5):306-310; 2006

Yun S, Tearney G, de Boer J, Bouma B. Removing the depth-degeneracy in optical frequency domain imaging with frequency shifting. *Optics Express* 12(20):4822-4828; 2004

Zamora-Alejo KV, Moore SP, Parker DGA, Ullrich K, Esterman A, Goggin M. Objective accommodation measurement of the Crystalens HD compared to monofocal intraocular lenses. *Journal of Refractive Surgery* 29(2):133-139; 2013

Zhang J, Nelson JS, Chen Z. Removal of a mirror image and enhancement of the signal-to-noise ratio in Fourier-domain optical coherence tomography using an electro-optic phase modulator. *Optics Letters* 30(2):147-149; 2005

Zhao M, Kuo AN, Izatt JA. 3D refraction correction and extraction of clinical parameters from spectral domain optical coherence tomography of the cornea. *Optics Express* 18(9):8923-8936; 2010